Copyright Warning & Restrictions

The copyright law of the United States (Title 17, United States Code) governs the making of photocopies or other reproductions of copyrighted material.

Under certain conditions specified in the law, libraries and archives are authorized to furnish a photocopy or other reproduction. One of these specified conditions is that the photocopy or reproduction is not to be "used for any purpose other than private study, scholarship, or research." If a, user makes a request for, or later uses, a photocopy or reproduction for purposes in excess of "fair use" that user may be liable for copyright infringement,

This institution reserves the right to refuse to accept a copying order if, in its judgment, fulfillment of the order would involve violation of copyright law.

Please Note: The author retains the copyright while the New Jersey Institute of Technology reserves the right to distribute this thesis or dissertation

Printing note: If you do not wish to print this page, then select "Pages from: first page # to: last page #" on the print dialog screen

The Van Houten library has removed some of the personal information and all signatures from the approval page and biographical sketches of theses and dissertations in order to protect the identity of NJIT graduates and faculty.

ABSTRACT

INVESTIGATION OF TOPOLOGICAL PHONONS IN DISCRETE MECHANICAL METAMATERIALS

by
Kai Qian

The study of topological mechanical metamaterials is a new emerging field that focuses on the topological properties of artificial mechanical structures. Inspired by topological insulators, topological mechanism has attracted intensive attention in condensed matter physics and successfully connected the quantum mechanical descriptions of electrons with the classical descriptions of phonons. It has led to experiments of mechanical metamaterials possessing topological characteristics, such as topologically protected conducting edges or surfaces without back-scattering. This dissertation presents a new experimental approach for mechanically engineering topological metamaterials based on patterning magnetically coupled spinners in order to localize the propagation of vibrations and evaluate different resonant modes. The topological properties of these metamaterials originate simply from their structures regardless of their nature and require no fine tuning of parameters. Strong excitation modes can also be observed through naked eyes, ideal for the exemplification of abstract theories. In Chapter 2, robust edge modes only due to smart patterning are reported. In Chapter 3, the analog of quantum valley Hall effect (QVHE) is emulated mechanically and its suitability for metamaterial applications is also discussed. In Chapter 4, flat frequency bands localized at open edges and antiphase boundary seams of topological mechanical metamaterials are shown to be promising for other metamaterials and novel applications. In Chapter 5, current work on classical Majorana edge modes of a ladder-like system, which is a counterpart to the classic Kitaev chain, is presented. At last, in Chapter 6, contributions, possible improvements, significant challenges, and potential applications are discussed.

INVESTIGATION OF TOPOLOGICAL PHONONS IN DISCRETE MECHANICAL METAMATERIALS

by
Kai Qian

A Dissertation
Submitted to the Faculty of
New Jersey Institute of Technology
in Partial Fulfillment of the Requirements for the Degree of
Doctor of Philosophy in Materials Science and Engineering

Department of Physics

May 2021

Copyright © 2021 by Kai Qian

ALL RIGHTS RESERVED

APPROVAL PAGE

INVESTIGATION OF TOPOLOGICAL PHONONS IN DISCRETE MECHANICAL METAMATERIALS

Kai Qian

Dr. Camelia Prodan, Dissertation Advisor Date
Associate Professor of Physics, NJIT

Dr. John Federici, Committee Member Date
Distinguished Professor of Physics, NJIT

Dr. Keun Hyuk Ahn, Committee Member Date
Associate Professor of Physics, NJIT

Dr. Benjamin Thomas, Committee Member Date
Assistant Professor of Physics, NJIT

Dr. Michael Siegel, Committee Member Date
Professor of Mathematical Sciences, NJIT

BIOGRAPHICAL SKETCH

Author:	Kai Qian
Degree:	Doctor of Philosophy
Date:	May 2021

Undergraduate and Graduate Education:

- Doctor of Philosophy in Materials Science and Engineering,
  New Jersey Institute of Technology, Newark, NJ, 2021
- Master of Science in Materials Science and Engineering,
  New Jersey Institute of Technology, Newark, NJ, 2017
- Bachelor of Engineering in Materials Science and Engineering,
  Nanjing University of Science and Technology, Nanjing, Jiangsu, P. R. China, 2014

Major:	Materials Science and Engineering

Publications:

Qian, K., Apigo, D. J., Padavić, K., Hedge, S. S., Prodan, E., Vishveshwara, S., and Prodan, C. Observation of Majorana edge modes in a Su-Schrieffer-Heeger ladder system. *In Preparation*.

Qian, K., Zhu, L., Ahn, K. H., and Prodan, C. (2020). Observation of flat frequency bands at open edges and antiphase boundary seams in topological mechanical metamaterials. *Physical Review Letters*, 125(22):225501.

Qian, K., Apigo, D. J., Prodan, C., Barlas, Y., and Prodan, E. (2018). Topology of the valley-Chern effect. *Physical Review B*, 98(15):155138.

Apigo, D. J., Qian, K., Prodan, C., and Prodan, E. (2018). Topological edge modes by smart patterning. *Physical Review Materials*, 2(12):124203.

Presentations:

Qian, K. (2021, March 15-19). *Observation of flat frequency bands at open edges and antiphase boundary seams in topological mechanical metamaterials* [Paper presentation]. American Physical Society March Meeting, United States.

Qian, K. (2020, December 4-6). *Observation of flat frequency bands at open edges and antiphase boundary seams in topological mechanical metamaterials* [Paper presentation]. American Physical Society Mid-Atlantic Section Fall Meeting, United States.

Qian, K. (2019, March 4-8). *Topology of the valley-Chern effect* [Paper presentation]. American Physical Society March Meeting, Boston, MA, United States.

Qian, K. (2019, March 4-8). *Observation of topological edge modes via smart patterning* [Paper presentation]. American Physical Society March Meeting, Boston, MA, United States.

And in the end the love you take is equal to the love you make.

The Beatles

ACKNOWLEDGMENT

First and foremost, I wish to express my sincere appreciation to my advisor, Prof. Camelia Prodan. It has been an honor to be her Ph.D. student. Dr. Prodan convincingly guided and encouraged me to be professional and do the right things even when the road got tough. She has wide knowledge and accurate physical intuition. She has been very supportive and patient since the first days I began working on topological systems. She often pointed out the incompleteness of my work and assisted me in improving my understanding on each problem. I would like to thank her for all her contributions of time and ideas during my Ph.D. study. Her guidance helped me in all the time of research and writing this dissertation. I could not have imagined having a better advisor and mentor for my Ph.D. study. I am grateful for the excellent example that she has provided as a successful researcher and professor.

Besides my advisor, I would like to thank the rest of my Ph.D. dissertation committee: Profs. John Federici, Keun Hyuk Ahn, Benjamin Thomas, and Michael Siegel, for their insightful comments and encouragement, but also for the hard question which incented me to widen my research from various perspectives. Additionally, I also want to thank Prof. Gordon Thomas, who was a member of my committee but retired in 2020, for being one of the kindest people I know.

I would like to thank the W. M. Keck Foundation and the Department of Physics at New Jersey Institute of Technology for the financial support of my research and my Teaching Assistant position, respectively.

I would like to express my sincere gratitude to my colleague and friend, Dr. David J. Apigo, for his guidance and assistance at every stage in my Ph.D. study. I would like to thank Profs. Ahn, Emil Prodan, and Smitha Vishveshwara, who provided me the opportunities to do the collaboration work. Without their precious support and help, it would have been

impossible to conduct my research projects. I also want to thank Dr. Kyle Dobiszewski for his contributions of ideas in design of my experiments.

My time at New Jersey Institute of Technology was made enjoyable in large part due to many friends. I would like to appreciate the conductor of NJIT Jazz Band, David Rimelis, for sharing all his love and musical knowledge. I want to thank Jonathan O'Buckley, Siying Wang, Richard Woods Jr., Sarah Ebert, Joey McCann, and Gabriel Ruiz for every moment we played as a band together. I am grateful to Megan T. Sweeney and Orion Wilchinsky for all the fun that we have had in the past five years. And while they are no longer with us, I want to thank Karen Pinoci and Kevin Milfort-Sanchez for showing me their passion and perseverance in what they truly love.

Last but not the least, I would like to express my gratitude to my family, especially my parents, Jin Qian and Yuqin Tan, for raising me and supporting me in all my pursuits unconditionally, and to my loving, encouraging, and smart fiancée, Wenting Cheng, whose faithful company during my entire Ph.D. life is really appreciated.

TABLE OF CONTENTS

Chapter **Page**

1 OVERVIEW 1

2 TOPOLOGICAL EDGE MODES VIA SMART PATTERNING 7

- 2.1 Introduction 7
- 2.2 Magnetically Coupled Mechanical Spinners 8
  - 2.2.1 Configurable Spinner 8
  - 2.2.2 Coupling and Dynamics 9
  - 2.2.3 1D Quasi-Periodic Pattern 12
- 2.3 Spectral Analysis 13
  - 2.3.1 Bulk Spectrum 13
  - 2.3.2 Topological Edge Spectrum 15
- 2.4 Summary 16

3 TOPOLOGY OF THE VALLEY-CHERN EFFECT 19

- 3.1 Introduction 19
- 3.2 Experimental Platform 21
  - 3.2.1 Configurable Spinners 21
  - 3.2.2 Mapping the Basic Couplings 21
- 3.3 QVHE with Coupled Spinners 25
  - 3.3.1 Mapping the Bulk Spectrum 27
  - 3.3.2 Berry Curvature 31
  - 3.3.3 Domain Walls 31
  - 3.3.4 Experimental Observation of the Domain Wall Modes 34
- 3.4 Summary 38

4 TOPOLOGICAL FLAT BANDS IN MECHANICAL METAMATERIALS . . . 39

- 4.1 Introduction 39
- 4.2 Flat Frequency Bands at Open Edges 40

TABLE OF CONTENTS
(Continued)

Chapter **Page**

4.2.1 Configuration of Systems 40
4.2.2 Results for Topological Insulator Systems 42
4.2.3 Topological and Nontopological Systems 43
4.2.4 Localization of Edge Modes 45
4.3 Flat Frequency Bands at Antiphase Boundaries 47
4.3.1 Ring-shaped System 47
4.3.2 Theoretical Tubular Model 48
4.4 Summary 49
4.5 Supplementary Material 49
4.5.1 Theoretical Analysis 49
4.5.2 Adequacy of the Chosen Spinner System Sizes 51
5 MAJORANA EDGE MODES IN A SU-SCHRIEFFER-HEEGER LADDER . . 54
5.1 Introduction 54
5.2 SSH Ladder System 55
5.2.1 Configuration 56
5.3 Experimental Results 56
5.3.1 Bulk and Edge Spectra 56
5.3.2 Edge Modes 57
5.3.3 Phase Transition 58
5.4 Summary 60
6 CONCLUSIONS 61
REFERENCES 65

LIST OF FIGURES

Figure **Page**

1.1 Example of the objects that differ in their genus, g, which counts the number of holes. $g = 0$ for the muffin and the plate; $g = 1$ for the donut and the cup. 2

1.2 Quantum Hall trio. Numbers in parentheses indicate the years of each discovery. H is the external magnetic field, and M is the magnetization. For all three quantum Hall effects, electrons flow through the lossless edge channels, with the rest of the system insulating. When there is a net forward flow of electrons for Hall resistance measurement, (left) those extra electrons occupy only the left edge channels in the quantum Hall system regardless of their spins, (center) opposite-spin electrons occupy opposite sides in the quantum spin Hall system, and (right) only spin-down electrons flow through the left edge in the quantum anomalous Hall system. The locking schemes between spin and flow direction, and the number of edge channels depend on the material details, and only the simplest cases are illustrated here. Source: [Oh, 2013]. 4

1.3 Overview of the two different families of topological acoustic metamaterials (zero-frequency versus high-frequency). Left: frequency versus momentum for typical band structures of an acoustic crystal. Black lines denote bulk excitations and coloured lines or dots indicate localized boundary modes. Note that for active metamaterials one can obtain a situation in which edge modes are truly unidirectional: that is, only the red or blue edge modes are present. The gap for which the topological features are relevant is shaded in red. Middle: the schematics show the generic set-up (‘hinges and rods’ versus ‘oscillating masses’) for both families, together with examples of recent experiments. The red dashed box in the Maxwell frames image indicates a boundary between two topological sectors. Right: lists of potential applications. Source: [Huber, 2016]. 6

2.1 (a) Example of the basic spinner configuration. The arms are detachable such that the spinners can be easily refitted. (b) Exemplification of a relative complex linear configuration of magnetically coupled spinners, with couplings in the front sideway (shown) and in the back (not shown). Source: [Apigo et al., 2018]. 9

LIST OF FIGURES
(Continued)

Figure **Page**

2.2 Mapping the coupling coefficients. (a) Illustration of a single spinner with the locations of magnets indicated. (b) Experimental apparatus for measuring the interaction potential of a dimer. Two spinners are placed on an aluminum track with variable distance, d. The system is actuated and the response is recorded using accelerometers. (c), (d) Response of the coupled spinner as the frequency is swept over the low/high resonances of a dimer spaced 9 mm apart. The standard fits indicate a quality factors of $Q = 40$ and 53, respectively. (e) Map of the high (red) and low (blue) resonant frequencies as functions of magnet spacing. (f) The coupling coefficients α (red dots) and β (blue dots), as derived from Equation (2.4) and the data from panel (e), together with the fit functions from Equations (2.5). The units of $2\pi^2 I \times \mathrm{Hz}^2$ are used for the coupling functions. Source: [Apigo et al., 2018]. 11

2.3 Example of a 1D quasi-periodic pattern topologically equivalent to the circles. (a) Display of a finite number of points of a pattern generated by the algorithm $x_n = n\, l_0 + r\, \sin(n\theta)$, with the particular values $l_0 = 1$, $r = 0.4$ and $\theta = \frac{2\pi}{\sqrt{15}}$. (b) A geometric algorithm to generate the same pattern. Source: [Apigo et al., 2018]. 13

2.4 Bulk spectrum as function of parameter θ. The parameters l_0 and r have been fixed to the experimental values: $l_0 = 76$ mm, $r = 2$ mm. $\theta = \frac{6\pi}{32}$ is used in the experiments. Source: [Apigo et al., 2018]. 14

2.5 Experimental bulk spectral characteristics. (a) A system of 32 spinners arranged in the pattern described by Equation (2.10). (b) Notations and experimental values: $\theta = \frac{6\pi}{32}$, $D = 66$ mm, $l_0 = 76$ mm, $r = 2$ mm. (c) Theoretically computed bulk spectrum for $\theta = \frac{2\pi}{\sqrt{117}} = \frac{6\pi}{32} + \mathcal{O}(10^{-3})$, together with the gap labels for the upper gaps. (d) Experimental reading from an accelerometer placed in the bulk of the system. The correspondence between theory and experiment is shown by the shaded regions. Source: [Apigo et al., 2018]. 15

2.6 Theoretical edge spectrum versus the measured one. (a) The predicted theoretical spectrum of a chain of 32 spinners with free ends, mapped as function of ω. (b) The resonant frequencies (dots) recorded at one end of the system, with the bulk spectrum from Figure 2.5(d) indicated by vertical grey bars. Dotted lines have been added to help indicate the chiral bands. In both panels, ω runs over the experimentally available values $\omega_n = n\theta$, $n = 0, \dots, 31$. Note that the theoretical plots include both (left and right) edge modes and this is why the chiral bands come in pairs. Source: [Apigo et al., 2018]. 16

LIST OF FIGURES
(Continued)

Figure **Page**

2.7 Measurements of the edge resonances. The panels report the readings from accelerometers placed on the second spinner from the edge for randomly rotated configurations of the spinner chain. Source: [Apigo et al., 2018]. . 17

2.8 Spatial profile of a resonant mode. The data shows the readings from four accelerometers placed on the first four spinners from the edge, as the frequency was swept over the last and most prominent bulk gap. The amplitudes of these readings are proportional with the size of the disks. For convenience, the full pattern of spinners is also shown. Source: [Apigo et al., 2018]. 17

3.1 Configurable spinner with detachable arms. (a) Ball bearing with six inserts. (b) Detachable arms with magnetic ends for coupling. (c-f) The four spinner configurations used in our study, together with the labels used in the text. The quality factors of the coupled spinners are measured to be around 50. Source: [Qian et al., 2018]. 22

3.2 Mapping the coupling coefficients. (a-b) The A-A and B-B dimmer configurations, respectively. (c) The experimentally measured resonant frequencies $f_{\pm}^{A-A}$ (red/blue dots, respectively) of the A-A dimer as functions of separation d between the magnets. (d) Same as (c) but for B-B dimer. (e) The ratios $\frac{f_+^{B-B}}{f_+^{A-A}}$ (red dots) and $\frac{f_-^{B-B}}{f_-^{A-A}}$ (blue dots) as function of separation. (f) The coupling coefficients α (solid red dots) and β (solid blue dots), as derived from Equation (3.6) in units of $2\pi^2 I_A \times \text{Hz}^2$, together with the analytic fits Equation (3.7) (continuous lines). Source: [Qian et al., 2018]. . 24

3.3 The A-B coupling. (a) The A-B dimer configuration. (b) The experimentally measured resonant frequencies $f_{\pm}^{A-B}$ as function of distance between the magnets. Source: [Qian et al., 2018]. 25

3.4 Bulk configuration. It is a finite bipartite honeycomb lattice populated with A (red) and B (blue) type spinners. The actuator appears at the bottom of the illustration. The inset shows the primitive cell (shaded region) and the primitive vectors $\boldsymbol{a}_1$ and $\boldsymbol{a}_2$ in yellow. Source: [Qian et al., 2018]. 26

3.5 Predicted bulk band spectra. Plots of the dispersion equations (3.18) for various values of the ratio $r = \frac{I_A}{I_B}$. The graphs are rendered as functions of $(k_1, k2) \in [-\pi, \pi]^2$ and the red dots indicate the position of the valleys points K and K'. Source: [Qian et al., 2018]. 30

LIST OF FIGURES
(Continued)

Figure **Page**

3.6 Predicted versus measured bulk spectrum. (a) The theoretical data taken from the last panel of Figure 3.5 ($r = 1.525$). The view point is chosen here such that k_2 is into the page and the red dots indicate the position of the valleys K and K'. (b) The reading from a sensor placed inside the spinner structure when the system is actuated from the edge. The shaded region in beige marks the spectral gap, which is consistent between theoretical and experimental results. Source: [Qian et al., 2018]. 30

3.7 Berry curvature. The theoretical calculations were performed with the experimental values of the coupling constants α and β and for the specified values of $r = I_A/I_B$. The last value $r = 1.525$ is used in the experimental demonstrations. The data is rendered as function of (k_1, k_2) whose axes are not shown. Source: [Qian et al., 2018]. 32

3.8 The experimental setup with a straight domain wall. The domain wall consists of the zigzag chain of B type (blue) spinners. Note the actuator positioned at one end of the domain wall. Source: [Qian et al., 2018]. 33

3.9 Schematic of the domain wall. Note that the domain wall does not cut any of the primitive cells. Source: [Qian et al., 2018]. 34

3.10 Predicted spectrum in the presence of a domain-wall. Simulations are shown for increasing values of $r = \frac{I_A}{I_B}$, ranging from 1 all the way to the experimental value of 1.525. The spectrum is computed on a strip with the domain-wall at the center. The doubly degenerated flat band seen in all panels is located at the edges of the ribbon, hence it is unrelated to the physics studied here. Source: [Qian et al., 2018]. 35

3.11 Experimental observation of the domain wall modes. The fine line marks the position of the interface relative to the honeycomb lattice, indicated by the black dots. The red disks mark the position of the motion sensors, which are placed above bonds. The size of a disk is proportional with the reading of the motion sensor at that location. The frequencies, which are marked in each panel, sample the entire bulk gap. The measurement are for the A-B system ($r = 1.525$). Source: [Qian et al., 2018]. 36

3.12 The experimental setup with a L-shaped domain wall. The domain wall consists of the zigzag chain of B type (blue) spinners. The actuator positioned at one end of the domain wall. Source: [Qian et al., 2018]. 37

3.13 Experimental observation of the L-shaped domain wall modes. Except for the shape of the interface, the rest of the details are shown in Figure 3.12. Source: [Qian et al., 2018]. 38

LIST OF FIGURES
(Continued)

Figure **Page**

4.1 (a) 6×6 spinner system, where rotatable spinners and magnetically coupled arms are highlighted and fixed spinners and arms without magnets are shaded. (b) Illustration of the spinner system pictured in (a), where the orange [grey] balls represent rotatable [fixed] spinners. The purple ellipse represents a unit cell. The blue [red] lines indicate the couplings within [between] the unit cells within the 1D SSH chains along the $0°$direction. The green lines indicate the constant interchain coupling, which is smaller than the average intrachain coupling. Coordinates (n_1, n_2) describe the position of the spinners. Source: [Qian et al., 2020]. 42

4.2 Results for topological systems. (a-e) Solid lines: Bulk mode spectra experimentally obtained by actuating and measuring at the $(N_1-1, 1)$ spinner for the $N_1 \times 6$ systems with $N_1 = 4$, 6, 8, 10, and 12, respectively. Dotted lines: Spectra obtained with the $(N_1/2 + 1, 5)$ spinner to reveal the top [bottom] of the upper [lower] bulk bands better. The blue areas indicate the lower and upper bulk bands. (f-j) Edge mode spectra experimentally obtained with the $(N_1, 2)$ spinner for the same systems as in (a-e), respectively. Red areas indicate the edge bands. A red arrow in (a) [blue arrows in (f)] indicates edge [bulk] modes appearing in the bulk [edge] spectra due to the short edge-to-edge distance. (k) Experimental and theoretical bulk and edge band widths versus the system size $N_1 \times N_2$. (l) Logarithm of experimental edge band width, $\ln(\Delta f_0)$, versus N_1 and fitting to the theory, resulting in the localization length at $k_2 = 0$, $\xi_0 \approx 3.2$, close to the theory value of 3.1 (see Section 4.5 Supplementary Material for details). Source: [Qian et al., 2020]. 44

4.3 Spectra experimentally obtained by actuating and measuring at the $(5, 1)$, $(6, 2)$, and $(6, 1)$ spinners for the 6×6 (a) topological and (b) nontopological systems. The edge band is present in the bulk band gap in (a), but absent in (b). Source: [Qian et al., 2020]. 45

4.4 (a-d): Patterns of modes. Colors represent the oscillation amplitudes of the spinners, estimated from slow motion movies by eyes. Stars mark actuated spinners. In (a) [(b)], an edge [bulk] mode is revealed at 23.6 Hz [19.5 Hz] in the edge [bulk] band for the 4×4 topological system. In (c) [(d)], an edge mode is revealed at 23.7 Hz [24.5 Hz] for the 6×4 [8×4] topological system. (e) Normalized oscillation amplitude of the (n_1, n_2) spinner versus its distance from the right edge, $12 - n_1$, when a single $(12, n_2)$ spinner $(n_2 = 1, ..., 6)$ at the right edge is actuated for the 12×6 topological system. (f) Symbols: semilogarithmic plot of (e) for even $12 - n_1$. Lines: linear fittings, leading to an average localization length $\xi = 1.5 \pm 0.3$, consistent with the theoretical range of $\xi(k)$, $0.9 \sim 3.1$. Source: [Qian et al., 2020]. . 46

LIST OF FIGURES
(Continued)

Figure **Page**

4.5 (a) Illustration of the SSH ring with fifteen spinners and a seam experimentally studied. See the caption for Figure 4.1(b). The purple line represents the extra coupling at a magnet distance of 6.5 mm for the chiral symmetry. (b) Red [Blue] line: Edge [Bulk] mode spectrum experimentally obtained by actuating and measuring at the spinner $\#1$ [$\#2$] for the SSH ring shown in (a). (c) Tubular model system with thirteen spinners in the azimuthal direction and an antiphase boundary seam, obtained by joining the $(1, n_2)$ and $(13, n_2+1)$ spinners of a planar system like Figure 4.1(b) with $N_1 = 13$. The grey balls represent fixed spinners interacting with the spinners at the seam. The magnification shows the antiphase boundary seam with the weak azimuthal couplings on both sides (the blue lines), and the couplings with the fixed spinners (the purple lines). (d) Band structure for the tubular system in (c). The blue lines represent the bulk bands and the red line the flat antiphase boundary seam band. Source: [Qian et al., 2020]. 48

4.6 Localization length $\xi(k_2)$ versus the edge state wave vector k_2 in the limit of the large edge-to-edge distance N_1 for the topological spinner systems. $\xi(k_2)$ varies between 0.9 at $k_2 = \pm\pi$ and 3.1 at $k_2 = 0$. Source: [Qian et al., 2020]. 51

4.7 (a) Symbols: Edge band width Δf_0 versus N_2, calculated for $N_1 \times N_2$ systems with $N_1 = 4, 6, 8, 10,$ and 12 and open boundary conditions. Horizontal solid lines: Δf_0 calculated for $N_2 = 1,000$ as a large N_2 limit for each case of N_1. Vertical dashed line: $N_2 = 6$ chosen for experimental setups. (b) Edge band width Δf_0 versus N_1, calculated for the $N_1 \times 6$ systems with open boundary conditions. The gray area approximately represents the experimental resolution, below which the edge band width cannot be measured reliably. Source: [Qian et al., 2020]. 53

5.1 (a) Spinner ladder system with the length of 13 rotatable spinners, where rotatable spinners and magnetically coupled arms are highlighted and fixed spinners and arms without magnets are shaded. (b) Illustration of the spinner ladder system pictured in (a), where rotatable spinners are colored white and blue and fixed spinners at both ends are colored grey. A purple plaquette represents a unit cell. d_i for $i = 1, 2$ and $i = 12$ denote the intrachain and interchain coupling distances between spinners in the $0°$and $60°$directions, respectively. 57

5.2 (a) Experimental and (b) theoretical resonance modes versus the interchain coupling distance d_{12}. In (a), the bulk modes are obtained by actuating and measuring at the $(1, 6)$ and $(1, 7)$ spinners and the edge modes at the $(1, 1)$ spinner in the ladder system. The grey areas indicate the bulk bands. . . . 58

LIST OF FIGURES
(Continued)

Figure **Page**

5.3 (a) Experimental spectra obtained by actuating at the $(1, 1)$ spinner and measuring at all the rotatable spinners in the ladder system with the interchain coupling distance $d_{12} = 8.0$ mm. Grey areas represent the lower and upper bulk bands. One spectral gap, which contains a strong edge mode at the frequency of 22.6 Hz, can be clearly identified. (b)-(e) Patterns of oscillations measured at the frequencies of (b) 14.3 Hz, (c) 21.0 Hz, (d) 22.6 Hz, and (e) 25.0 Hz, respectively. Colors represent the oscillation amplitudes of the rotatable spinners. Stars mark actuated spinners. 59

5.4 Spectra experimentally obtained by actuating and measuring at the $(1, 1)$, $(1, 6)$, and $(1, 7)$ spinners of the ladder systems with interchain coupling distances (a) $d_{12} = 1.0$ mm, (b) $d_{12} = 4.0$ mm and (c) $d_{12} = 7.0$ mm, respectively. The edge band is prominent in the bulk band gap in (c), but absent in (a) and (b). The bulk band gap is absent in (b). 60

6.1 Example of the unit cell as our approach for going beyond 2D metamaterials, which is inspired by (d) the body centered cubic lattices. (a-c) The configurations of a single spinner for eight couplings. (e) Prototype of the unit cell for 3D mechanical lattice. 64

CHAPTER 1

OVERVIEW

Metamaterials (meta means *beyond* in Greek) are artificially fabricated materials with superior and unusual properties that do not exist in naturally occurring materials, such as a negative electrical permittivity [Veselago, 1967]. These properties originate from their periodically or randomly distributed structures [Wang et al., 2016]. The launch of this field is marked by a famous paper published in 2000 by Pendry [Pendry, 2000], who discussed a class of materials with a negative refractive index. As a result, metamaterials became an explosive interest due to their potential for light manipulation and cloaking [Smith et al., 2004, Schurig et al., 2006, Alù and Engheta, 2007, Alù and Engheta, 2008, Liu et al., 2009]. The concept of metamaterials was soon introduced in phononic crystals and acoustic systems [Lu et al., 2009]. With the same idea to control the wave propagation, from electromagnetic to elastic waves, metamaterials meet conventional mechanics. Materials with any counterintuitive mechanical properties originated from their distinctive structures can be called mechanical metamaterials [Xin et al., 2020], for example, materials with a negative compressibility [Nicolaou and Motter, 2012] or a negative Poisson's ratio [Lakes, 2017]. Among these examples, a new class named topological mechanical metamaterials [Süsstrunk and Huber, 2016], which are inspired by electronic topological insulators [König et al., 2007, Hasan and Kane, 2010], has attracted intensive attentions over the past decade. They have interesting topological properties that are difficult to achieve with ordinary mechanical metamaterials. So, what is topological and why does it matter?

Topology, in mathematics, is about the study of geometric properties that are not destroyed by continuous deformations. A coffee mug is equal to a donut for topologists since the number of holes, which is a topological invariant, is always the same during smooth transformations, as shown in Figure 1.1. The concept of topology was brought

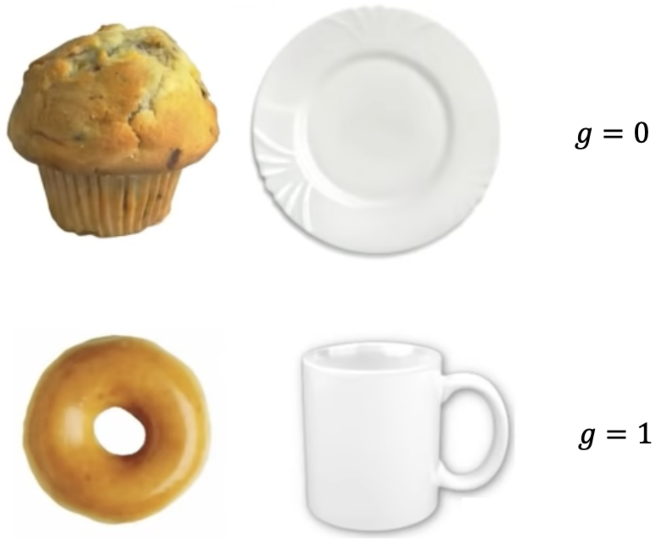

Figure 1.1 Example of the objects that differ in their genus, g, which counts the number of holes. $g = 0$ for the muffin and the plate; $g = 1$ for the donut and the cup.

into the field of condensed matter physics in the 1980s thanks to Thouless, Haldane, and Kosterlitz, who won the Nobel Prize in 2016 for their theoretical discoveries of topological phase transitions and topological phases of matter. A topological phase is a system state that certain physical properties depend on global topology instead of local details. In 1980, von Klitzing discovered the quantum Hall effect (or integer quantum Hall effect that, when the electrons were confined into a two-dimensional (2D) gas form, the Hall resistance became exactly quantized at $h/(ne^2)$, where n is a positive integer [Klitzing et al., 1980]. Afterwards, the whole condensed matter physics community started to realize that the intrinsic relation between the integer quantum Hall effect and the band structure topology can be adequately explained by a natural change of a topological invariant, namely the TKNN number (or the first Chern number) [Thouless et al., 1982]. New topological phases such as the quantum spin Hall effect [Kane and Mele, 2005a, Kane and Mele, 2005b, Bernevig and Zhang, 2006, Bernevig et al., 2006] and the quantum anomalous Hall effect [Laughlin, 1983, Haldane, 1988, Chang et al., 2013] were later discovered and evaluated. As shown in Figure 1.2, electrons can transport only along the dissipationless channels within the edges of these 2D quantum Hall systems, with the bulk insulating. Characterized by such edge (or surface in three dimensions) states, topological insulators are classified as an entirely new class of electronic materials, creating a surge of research activities after 2005. Similar to a regular insulator, a topological insulator also has a bulk energy gap separating the conduction band from the valence band. However, the interfaces (edges or surfaces) of a topological insulator are filled with gapless chiral conducting states. These states are insensitive to disorder since there is no state available for backscattering. Such amazing electronic topological properties have hence inspired many physicists, chemists, materials scientists, and engineers with different fields of interest. By considering the band theory and Bloch's theorem, one can easily see the similarity among electrons in crystals, photons in photonic crystals, and phonons in phononic crystals. As a result, the concept of topological phases have been naturally expanded from electronics to optics, acoustics and even further to mechanical vibrations. In 2008, Raghu and Haldane theoretically proposed an optical analog of the quantum Hall systems and established a unidirectional channel for electromagnetic energy [Raghu and Haldane, 2008], which was experimentally realized [Wang et al., 2009]. In 2009, Prodans theoretically demonstrated how topological vibration modes are the key to the dynamic instability of the microtubules [Prodan and Prodan, 2009]. In 2014, Fleury *et al.* introduced an acoustic analog of the Zeeman effect by using a linear, magnetic-free circulator to mimic a magnetic bias [Fleury et al., 2014]. With the influences of their creative studies, various topological photonic and phononic metamaterials were later developed [Lu et al., 2014, Zhang et al., 2018, Ma et al., 2019a, Ozawa et al., 2019]. Moreover, a natural question has been asked: How do we realize topological phases with quantum mechanical descriptions in classical mechanical systems where Newton's equations of motion describe phonons?

To realize this analogy, one can consider a generalized model consisting of coupled oscillators. When considering the motion of the model as a Hermitian eigenvalue problem

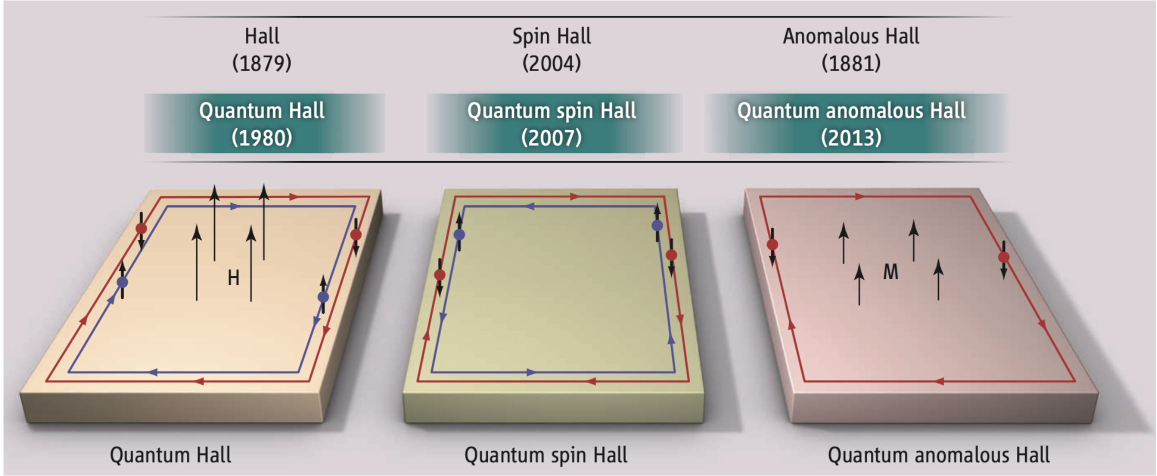
Hall
(1879)
Spin Hall
(2004)
Anomalous Hall
(1881)
Quantum Hall
(1980)
Quantum spin Hall
(2007)
Quantum anomalous Hall
(2013)
H
M
Quantum Hall
Quantum spin Hall
Quantum anomalous Hall

Figure 1.2 Quantum Hall trio. Numbers in parentheses indicate the years of each discovery. H is the external magnetic field, and M is the magnetization. For all three quantum Hall effects, electrons flow through the lossless edge channels, with the rest of the system insulating. When there is a net forward flow of electrons for Hall resistance measurement, (left) those extra electrons occupy only the left edge channels in the quantum Hall system regardless of their spins, (center) opposite-spin electrons occupy opposite sides in the quantum spin Hall system, and (right) only spin-down electrons flow through the left edge in the quantum anomalous Hall system. The locking schemes between spin and flow direction, and the number of edge channels depend on the material details, and only the simplest cases are illustrated here. Source: [Oh, 2013].

for frequency ω, Newton's equations can be rewritten as [Huber, 2016]:

$$i\frac{\partial}{\partial t}\begin{pmatrix}\sqrt{D}^T x\\ i\dot{x}\end{pmatrix}=\begin{pmatrix}0 & \sqrt{D}^T\\ \sqrt{D} & iA\end{pmatrix}\begin{pmatrix}\sqrt{D}^T x\\ i\dot{x}\end{pmatrix}, \tag{1.1}$$

where D is the dynamic matrix that encodes forces between oscillators and A is a skew-symmetric matrix that describes the conservatives couplings between positions and velocities. Here, Equation (1.1) is similar to the Schrödinger's equation. It also gives the classical mechanical system a particle-hole symmetry, which is usually seen in the studies of superconductivity. By taking advantage of the particle–hole symmetry, or engineering the dynamical matrix D and the skew-symmetric matrix A, one can implement zero-frequency properties or high-frequency properties of topological mechanical systems, as shown in Figure 1.3. At this point, topology can be conveniently implemented in classical mechanical systems. During the past years, researchers have been committed to discover topological phases in mechanical metamaterials. In 2014, Kane and Lubensky implemented zero-frequency modes using isolated lattices [Kane and Lubensky, 2014]. In 2017, Prodan *et al.* demonstrated the Majorana edge mode in the coupled dimer systems [Prodan et al., 2017]. Numerous efforts were also made in other different metamaterials and various approaches to realize topological phases in mechanical metamaterials were developed [Süsstrunk and Huber, 2016, Huber, 2016, Rocklin et al., 2017, Xin et al., 2020].

In this dissertation, I will present our past and current studies on topologically protected edge modes via smart patterning, QVHE, topological flat frequency bands, and Majorana edge modes through the exploitation of novel and versatile experimental platforms consisting of magnetically coupled fidget spinners. Our results are scalable and can apply to other metamaterials, such as photonic, electronic, acoustic, plasmonic, circuitry, optical lattice, and microwave metamaterials, potentially leading to novel phenomena and device applications.

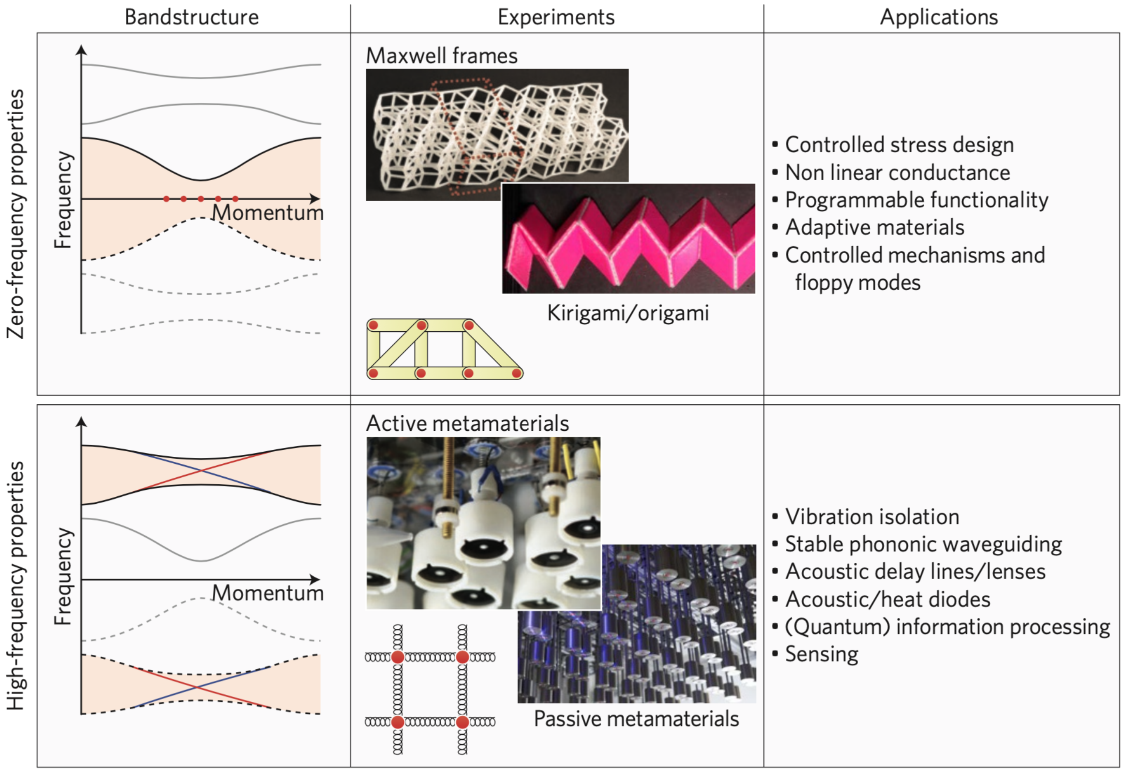
Bandstructure
Experiments
Applications
Zero-frequency properties
Frequency
Momentum
Maxwell frames
Kirigami/origami
• Controlled stress design
• Non linear conductance
• Programmable functionality
• Adaptive materials
• Controlled mechanisms and floppy modes
High-frequency properties
Frequency
Momentum
Active metamaterials
Passive metamaterials
• Vibration isolation
• Stable phononic waveguiding
• Acoustic delay lines/lenses
• Acoustic/heat diodes
• (Quantum) information processing
• Sensing

Figure 1.3 Overview of the two different families of topological acoustic metamaterials (zero-frequency versus high-frequency). Left: frequency versus momentum for typical band structures of an acoustic crystal. Black lines denote bulk excitations and coloured lines or dots indicate localized boundary modes. Note that for active metamaterials one can obtain a situation in which edge modes are truly unidirectional: that is, only the red or blue edge modes are present. The gap for which the topological features are relevant is shaded in red. Middle: the schematics show the generic set-up ('hinges and rods' versus 'oscillating masses') for both families, together with examples of recent experiments. The red dashed box in the Maxwell frames image indicates a boundary between two topological sectors. Right: lists of potential applications. Source: [Huber, 2016].

CHAPTER 2

TOPOLOGICAL EDGE MODES VIA SMART PATTERNING

In this chapter, we will demonstrate that topological edge modes can emerge solely from a smart patterning of a metamaterial. The work was in collaboration with Dr. David J. Apigo and Prof. Camelia Prodan from the Department of Physics at New Jersey Institute of Technology, and Prof. Emil Prodan from the Department of Physics at Yeshiva University.

2.1 Introduction

Over the past years, experimental demonstrations of topological effects in classical systems abound [Prodan and Prodan, 2009, Berg et al., 2011, Zhang et al., 2011b, Kane and Lubensky, 2014, Chen et al., 2014, Khanikaev et al., 2015, Deymier et al., 2015, Mousavi et al., 2015, Peano et al., 2015, Paulose et al., 2015a, Xiao et al., 2015a, Paulose et al., 2015b, Wang et al., 2015, Xiao et al., 2015b, Mao et al., 2015, Kariyado and Hatsugai, 2015, Nash et al., 2015, Süsstrunk and Huber, 2015, Süsstrunk and Huber, 2016, Deymier and Runge, 2016, Pal et al., 2016, Salerno et al., 2016, Rocklin et al., 2016, Prodan et al., 2017] and this field is rapidly moving towards the next stage where practical devices and concrete applications should emerge. However, it is extremely difficult to maintain controls over the designs as the systems are scaled down to meet certain practical constraints, especially on those based on specific configurations and values of the couplings. We demonstrate a new route to achieve robust edge modes only through patterning of the mechanical structures. More precisely, metamaterials consisting of bundles or stacks of certain patterns have all their bulk spectral gaps completely filled with topological edge spectrum when the system is halved. This edge spectrum cannot be gapped by changing boundary condition or by any adiabatic deformation of the metamaterials. This phenomenon is completely due to the patterning itself and does not require any fine tuning of the couplings, except for the opening of the bulk spectral gaps. We provide the experimental observation of such topological edge modes in a quasi-periodic mechanical system. Topological metamaterials with these principles can be engineered at any scale, which provides a practical platform for applications and devices.

2.2 Magnetically Coupled Mechanical Spinners

In this section, we will take a close look at this versatile experimental platform based on magnetically coupled mechanical spinners. Experimental platforms of this principle not only enables the realization and characterization of a topological pattern of mechanical resonators, but also helps with the formulation and exemplification of the theoretical concepts. For simplicity, we use one-dimensional (1D) patterns, but generalizations to higher dimensions can be easily achieved, as mentioned in the papers [Prodan and Schulz-Baldes, 2016, Prodan and Shmalo, 2019].

2.2.1 Configurable Spinner

A configurable mechanical spinner is shown in Figure 2.1(a). It consists of a stainless steel ball bearing mounted in a threaded brass encapsulation, which is fitted with six grooved indentations for attaching additional arms. For experimentation, two of the arms are attached with neodymium disk magnets, which provide the couplings between each spinner when arranged in linear patterns. The centers of the spinners are pinned down, resulting in one rotational degree of freedom, φ. By stacking and coupling such spinners, extremely complex systems can be created one degree of freedom at a time (see the example in Figure 2.1(b)). With the full control over the degrees of freedom and the couplings, any quadratic discrete Hamiltonian can be implemented to drive the small oscillations of the magnetically coupled spinners.

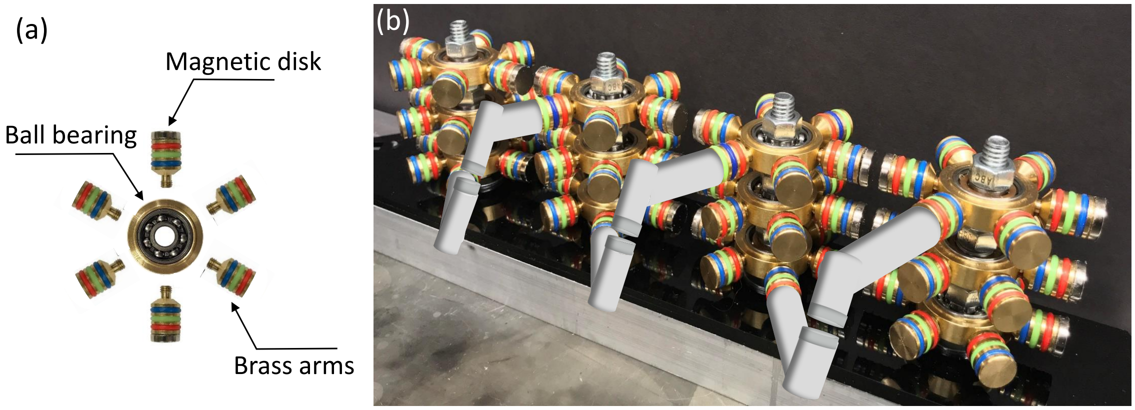

Figure 2.1 (a) Example of the basic spinner configuration. The arms are detachable such that the spinners can be easily refitted. (b) Exemplification of a relative complex linear configuration of magnetically coupled spinners, with couplings in the front sideway (shown) and in the back (not shown). Source: [Apigo et al., 2018].

2.2.2 Coupling and Dynamics

The magnetic couplings between the spinners can be measured by mapping the resonant modes of a dimer, whose dynamics is governed by the Lagrangian:

$$L(\varphi_1, \varphi_2, \dot{\varphi}_1, \dot{\varphi}_2) = \tfrac{1}{2} I \dot{\varphi}_1^2 + \tfrac{1}{2} I \dot{\varphi}_2^2 - V(\varphi_1, \varphi_2), \tag{2.1}$$

where I is the moment of inertia for a single spinner. In the regime of small oscillations around the equilibrium configuration, $\varphi_1 = \varphi_2 = 0$, the potential can be approximated quadratically in the form:

$$V(\varphi_1, \varphi_2) = \tfrac{1}{2} \alpha (\varphi_1^2 + \varphi_2^2) + \beta \varphi_1 \varphi_2, \tag{2.2}$$

where α and β represent the coupling coefficients. As a result, the pair of the two resonant modes can be computed explicitly:

$$f_\pm = \sqrt{\frac{\alpha \pm \beta}{4\pi^2 I}}. \tag{2.3}$$

The experimentally measured resonant frequencies are reported in Figure 2.2(e) as functions of the distance d between the magnets. Since Equations (2.3) can be inverted as:

$$\alpha = 2\pi^2 I \left(f_+^2 + f_-^2\right), \quad \beta = 2\pi^2 I \left(f_+^2 - f_-^2\right), \tag{2.4}$$

together with the experimental data, it is easy to determine the coupling coefficients $\alpha(d)$ and $\beta(d)$. The details of mapping are provided in Figure 2.2. In Figure 2.2(f), the experimental coupling coefficients are well fitted by:

$$\begin{aligned} \alpha(d) &= -\tfrac{778.14}{\sqrt{d}} + \tfrac{3439.81}{d} + \tfrac{161.35}{d^2}, \\ \beta(d) &= -\tfrac{654.09}{\sqrt{d}} + \tfrac{2763.66}{d} + \tfrac{575.89}{d^2}. \end{aligned} \tag{2.5}$$

When the centers of the spinners are pinned in a 1D pattern $\omega = \{x_n\}_{n\in\mathbb{Z}}$, the Lagrangian of the system becomes:

$$L = \sum_{n\in\mathbb{Z}} \left[\tfrac{1}{2} I \dot{\varphi}_n^2 - \Big(\alpha(d_{n-1}) + \alpha(d_n)\Big)\varphi_n^2 - \beta(d_n)\varphi_n\varphi_{n+1} \right], \tag{2.6}$$

where $d_n = x_{n+1} - x_n - D$ and D is the diameter of a spinner. The equations of motion read:

$$-I\ddot{\varphi}_n = \Big(\alpha(d_{n-1}) + \alpha(d_n)\Big)\varphi_n + \beta(d_{n-1})\varphi_{n-1} + \beta(d_n)\varphi_{n+1}. \tag{2.7}$$

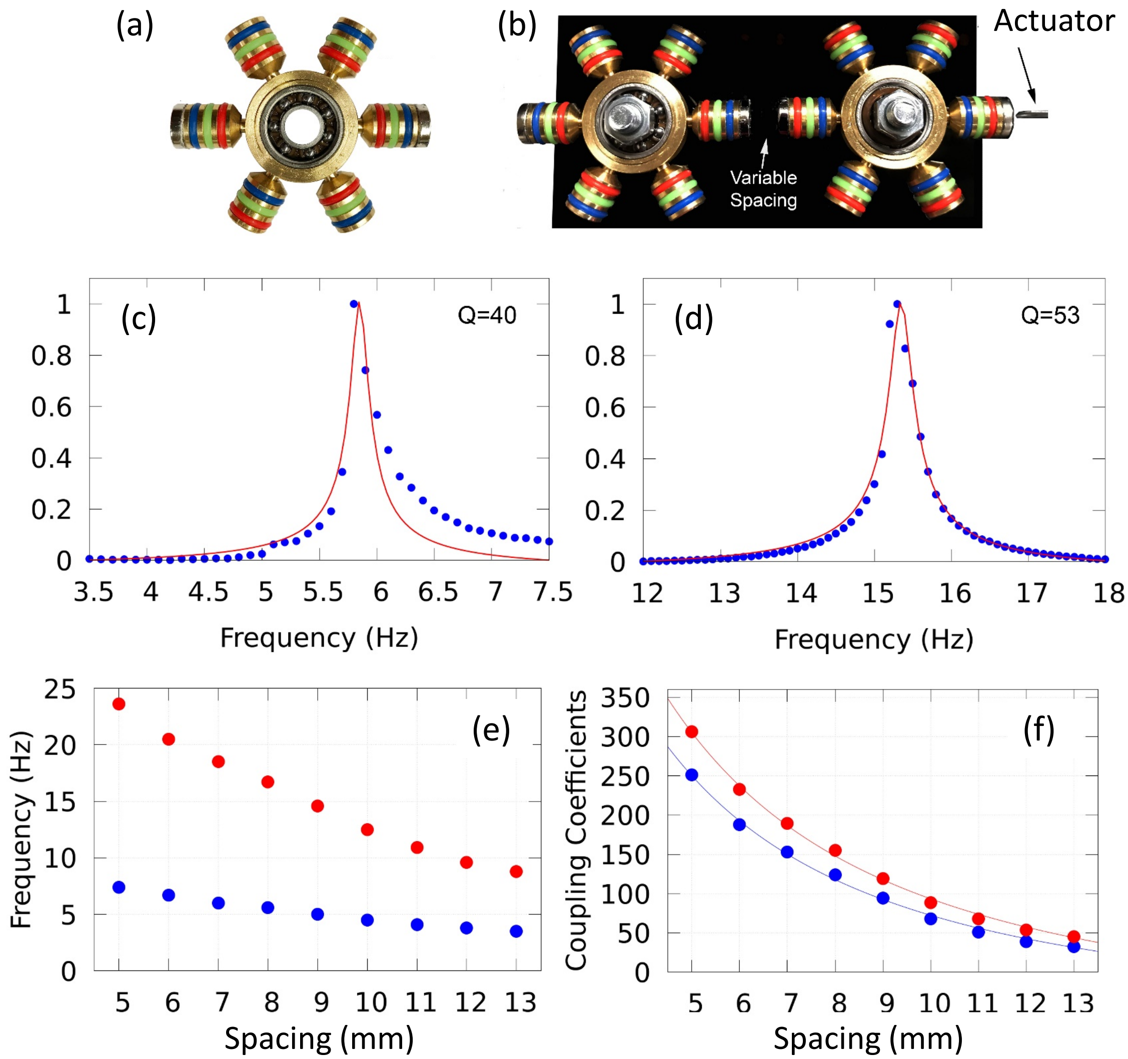

Figure 2.2 Mapping the coupling coefficients. (a) Illustration of a single spinner with the locations of magnets indicated. (b) Experimental apparatus for measuring the interaction potential of a dimer. Two spinners are placed on an aluminum track with variable distance, d. The system is actuated and the response is recorded using accelerometers. (c), (d) Response of the coupled spinner as the frequency is swept over the low/high resonances of a dimer spaced 9 mm apart. The standard fits indicate a quality factors of $Q = 40$ and 53, respectively. (e) Map of the high (red) and low (blue) resonant frequencies as functions of magnet spacing. (f) The coupling coefficients α (red dots) and β (blue dots), as derived from Equation (2.4) and the data from panel (e), together with the fit functions from Equations (2.5). The units of $2\pi^2 I \times \mathrm{Hz}^2$ are used for the coupling functions. Source: [Apigo et al., 2018].

The degrees of freedom can be encoded in the column vector:

$$|\varphi\rangle = (\dots, \varphi_{-1}, \varphi_0, \varphi_1, \dots)^T, \tag{2.8}$$

and let us denote $|n\rangle$ by the column vector with 1 at position n and zero in the rest. Then $|\varphi\rangle = \sum_n \varphi_n |n\rangle$ and, with the ansatz $|\varphi(t)\rangle = \mathrm{Re}\Big[e^{i2\pi f t}|\psi\rangle\Big]$ and the units of $2\pi^2 I \times \mathrm{Hz}^2$ from Figure 2.2(f), the system of equations of motion becomes $f^2|\psi\rangle = H|\psi\rangle$ with:

$$\begin{aligned} H = \sum_{n\in\mathbb{Z}} \Bigg[& \Big(\alpha(d_{n-1}) + \alpha(d_n)\Big)|n\rangle\langle n| \\ & + \beta(d_{n-1})|n\rangle\langle n-1| + \beta(d_n)|n\rangle\langle n+1| \Bigg]. \end{aligned} \tag{2.9}$$

At this point, it is a classical eigensystem for Hamiltonian, H, in the Hilbert space $\ell^2(\mathbb{Z})$.

The analysis above serves as a model for generically patterned resonators. It can be implemented for other spinner configurations, for example, the other systems presented in this dissertation, even for complex ones that include stacking and couplings beyond first neighbors, such as the exemplification shown in Figure 2.1(b).

2.2.3 1D Quasi-Periodic Pattern

As mentioned by Apigo *et al.* [Apigo et al., 2018], the discrete set of patterns can be topologically equivalent with the circles. The simplest 1D pattern is illustrated in Figure 2.3(a) and its analytic expression is in the form:

$$x_n = n\, l_0 + r\, \sin(n\theta), \quad r < \frac{l_0}{2}, \quad n \in \mathbb{Z}, \tag{2.10}$$

where θ is an irrational fraction of 2π. Figure 2.3(b) explains the geometric algorithm of this pattern. The point labeled by 0 is always fixed at the origin of the real axis and set the labels to be consistent with the ordering $\ldots < x_{-1} < x_0 = 0 < x_1 < \ldots$. This implicitly assumes that two points are never on top of each other. From topological point of view, any closed loop is also a circle, hence more complex patterns can be generated by the same algorithm but using a deformed circle. Although the algorithm is simple, the resulting patterns can be extremely complex and irregular. We can actually allow not only continuous deformations of the resonators but also of the patterns themselves [Apigo et al., 2018].

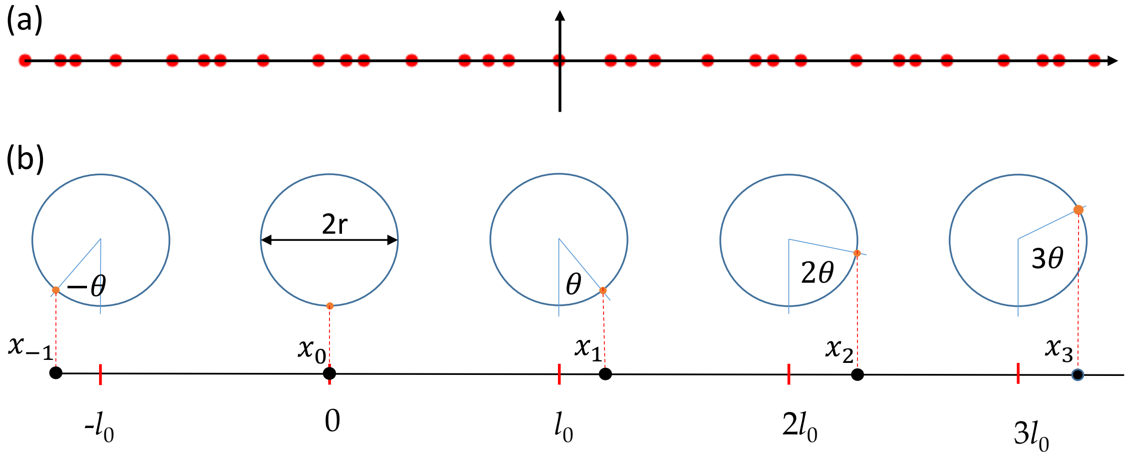

Figure 2.3 Example of a 1D quasi-periodic pattern topologically equivalent to the circles. (a) Display of a finite number of points of a pattern generated by the algorithm $x_n = n\,l_0 + r\,\sin(n\theta)$, with the particular values $l_0 = 1$, $r = 0.4$ and $\theta = \frac{2\pi}{\sqrt{15}}$. (b) A geometric algorithm to generate the same pattern. Source: [Apigo et al., 2018].

2.3 Spectral Analysis

2.3.1 Bulk Spectrum

The resonant frequency spectrum for Hamiltonian (2.9) over the pattern (2.10) is shown in Figure 2.4 as function of θ. The calculation is performed on a finite pattern of length $L = 840$ with periodic boundary condition for all commensurate values $\theta_n = \frac{2n\pi}{L}$, where the empirical coupling coefficients α and β are used. The similarity between this spectrum and the Hofstadter spectrum [Hofstadter, 1976] is remarkable. The main characteristic of the spectrum is the fractal network of spectral gaps, where each gap is topological, which implies the emergence of topological edge modes.

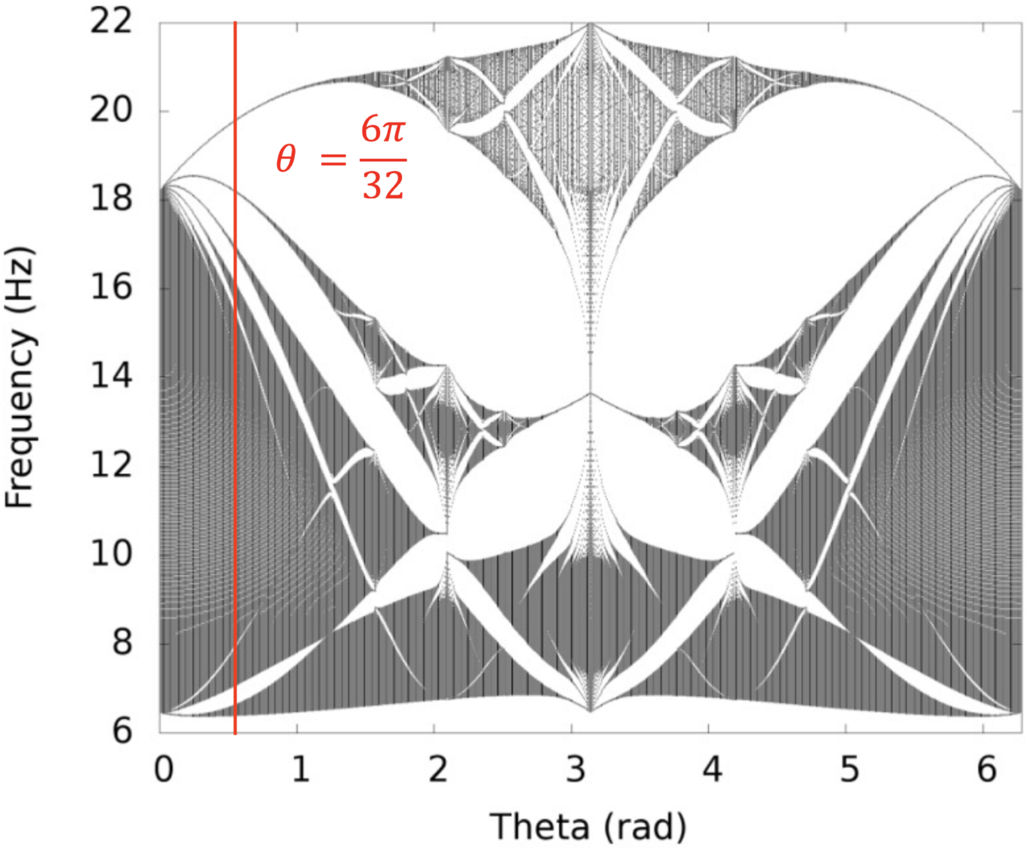

Figure 2.4 Bulk spectrum as function of parameter θ. The parameters l_0 and r have been fixed to the experimental values: $l_0 = 76\,\text{mm}$, $r = 2\,\text{mm}$. $\theta = \frac{6\pi}{32}$ is used in the experiments. Source: [Apigo et al., 2018].

The bulk spectrum has been mapped experimentally for select values of θ. The setup is shown in Figures 2.5(a) and 2.5(b). Throughout, the units of length are millimeters. To accommodate for the diameter, $D = 66$ mm, of the spinners, their centers have been arranged according to the algorithm $x_n = 76n + 2\,\sin(n\theta)$, $\theta = \frac{6\pi}{32}$, leading to a distance between the magnets (see Equation (2.6)):

$$d_n = 10 + 2\sin\Big((n+1)\theta\Big) - 2\sin\Big(n\theta\Big), \quad n \in \mathbb{Z}. \tag{2.11}$$

These are the inputs for Hamiltonian (2.9). The theoretically computed spectrum and the experimentally measured one are reported in Figures 2.5(c) and 2.5(d), respectively. The overall quantitative agreement is good, especially for the upper part of the spectrum. In fact, a rigorous correspondence between the two was established (see the guiding shaded regions in Figures 2.5(c) and 2.5(d)), by matching the experimental and theoretical profiles of the normal modes.

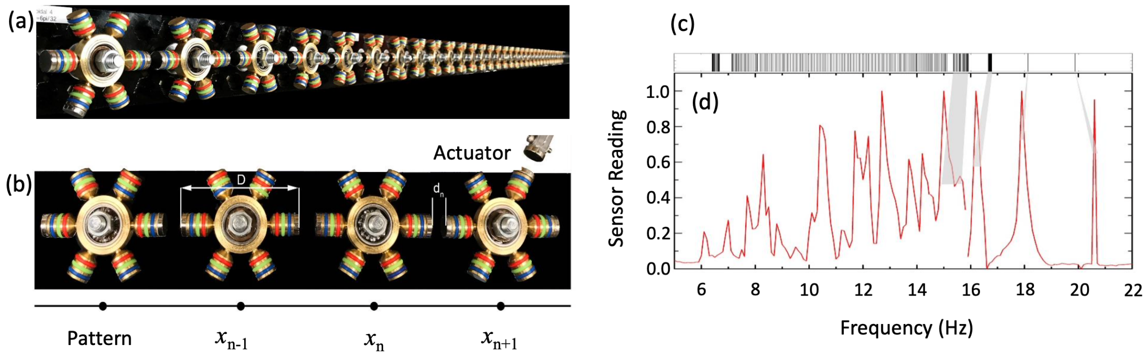

Figure 2.5 Experimental bulk spectral characteristics. (a) A system of 32 spinners arranged in the pattern described by Equation (2.10). (b) Notations and experimental values: $\theta = \frac{6\pi}{32}$, $D = 66$ mm, $l_0 = 76$ mm, $r = 2$ mm. (c) Theoretically computed bulk spectrum for $\theta = \frac{2\pi}{\sqrt{117}} = \frac{6\pi}{32} + \mathcal{O}(10^{-3})$, together with the gap labels for the upper gaps. (d) Experimental reading from an accelerometer placed in the bulk of the system. The correspondence between theory and experiment is shown by the shaded regions. Source: [Apigo et al., 2018].

2.3.2 Topological Edge Spectrum

The simulation in Figure 2.6(a) shows that the edge spectrum splits into chiral bands. Since the computation was performed on a finite rather than a halved system, the chiral bands appear always in pairs, one per edge. The experimental edge spectrum is shown in Figure 2.6(b). In these experiments, the system shown in Figure 2.5(a) is actuated from the first spinner between 14.0 and 21.0 Hz in steps of 0.1 Hz. One spinner is then moved from the front to the back of the chain, effectively implementing the translation, and the measurements are repeated. By cycling this whole process, one can shift the pattern 32 times and generate the experimental measure of the edge spectrum. Topological edge modes are detected at proper frequencies inside the bulk spectral gaps as the frequency is swept. They manifest as extremely strong and well-defined resonances, visible to the naked eye. A quantitative account of this phenomenon is reported in Figure 2.7, which displays the reading from an accelerometer placed on the uncoupled arm of the second spinner from the edge. The edge resonances appear as prominent peaks in these measurements. Figure 2.8 shows the spatial profile of an edge resonant mode detected in the last and most prominent bulk gap, which confirms that the mode is extremely well localized near the edge.

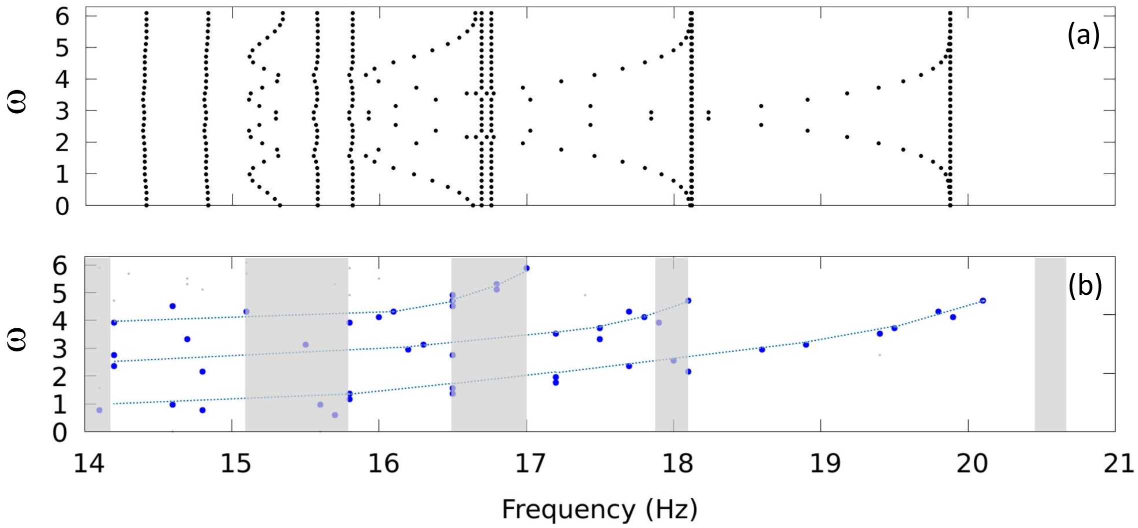

Figure 2.6 Theoretical edge spectrum versus the measured one. (a) The predicted theoretical spectrum of a chain of 32 spinners with free ends, mapped as function of ω. (b) The resonant frequencies (dots) recorded at one end of the system, with the bulk spectrum from Figure 2.5(d) indicated by vertical grey bars. Dotted lines have been added to help indicate the chiral bands. In both panels, ω runs over the experimentally available values $\omega_n = n\theta$, $n = 0, \dots, 31$. Note that the theoretical plots include both (left and right) edge modes and this is why the chiral bands come in pairs. Source: [Apigo et al., 2018].

2.4 Summary

This study shows that the collective dynamics of identical coupled mechanical resonators are fully determined by the patterns in which they are arranged. In other words, topological characteristics in mechanical systems can be induced solely through patterning in a manner entirely independent of the structure of the resonators and the details of the couplings. Such

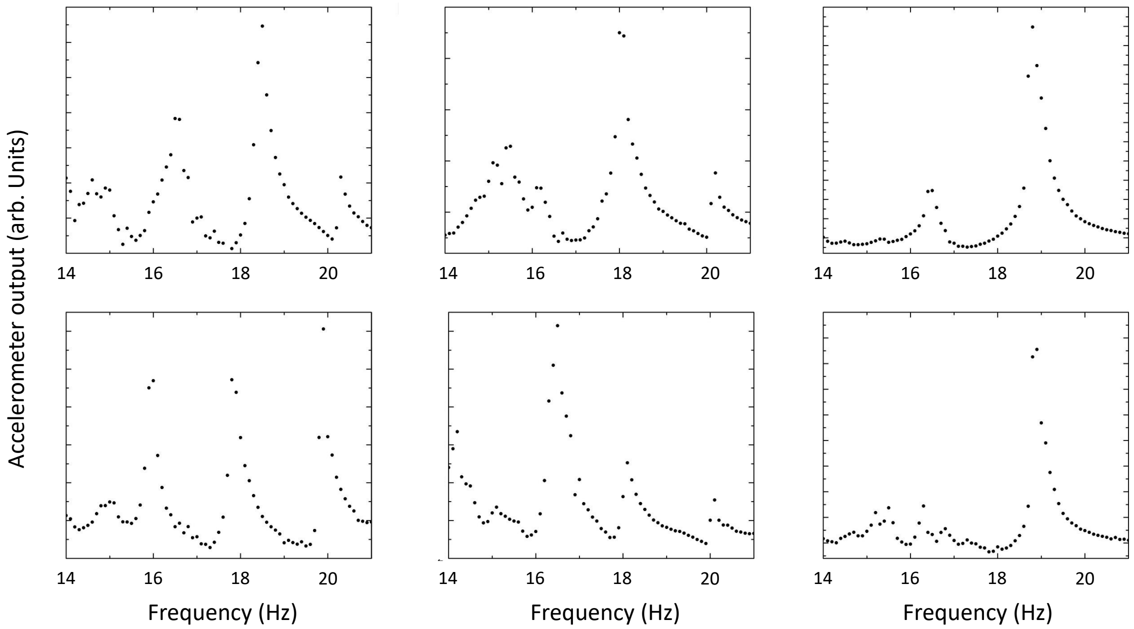

Figure 2.7 Measurements of the edge resonances. The panels report the readings from accelerometers placed on the second spinner from the edge for randomly rotated configurations of the spinner chain. Source: [Apigo et al., 2018].

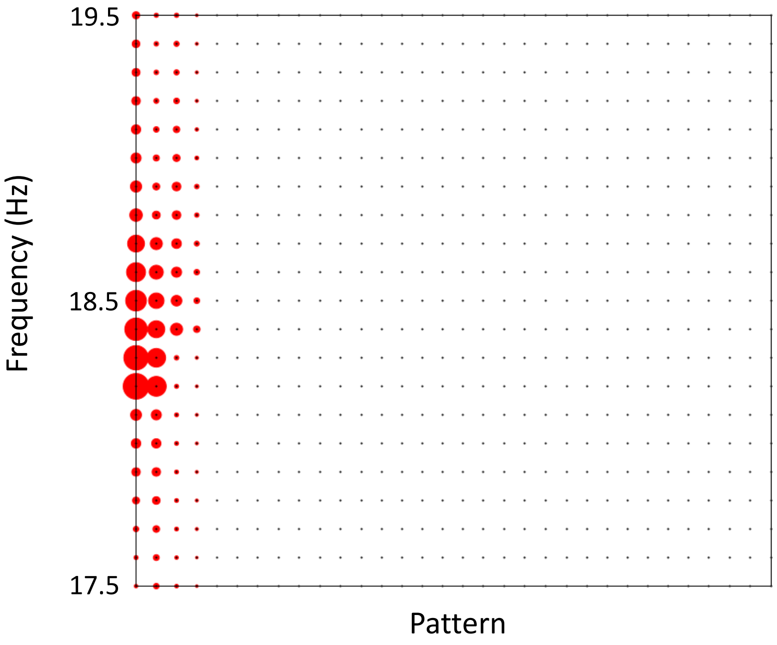

Figure 2.8 Spatial profile of a resonant mode. The data shows the readings from four accelerometers placed on the first four spinners from the edge, as the frequency was swept over the last and most prominent bulk gap. The amplitudes of these readings are proportional with the size of the disks. For convenience, the full pattern of spinners is also shown. Source: [Apigo et al., 2018].

systems require no fine tuning of parameters. For these topological systems, the boundary resonant modes fully fill all existing spectral gaps whenever the system is halved and the boundary spectrum cannot be removed or gapped by any boundary condition. Our results are not bound to mechanical systems. Topological metamaterials based on these principles can be easily engineered at any scale, which provides a practical platform for potential applications and devices.

CHAPTER 3

TOPOLOGY OF THE VALLEY-CHERN EFFECT

In this chapter, we will focus on our implementation of QVHE with a 2D honeycomb spinner system and demonstrate the limitation of this effect for metamaterial applications. The work was in collaboration with Dr. David J. Apigo and Prof. Camelia Prodan from the Department of Physics at New Jersey Institute of Technology and Dr. Yafis Barlas and Prof. Emil Prodan from the Department of Physics at Yeshiva University.

3.1 Introduction

Graphene and graphene-like honeycomb-lattice systems continue to be experimentally studied for new ideas and sources of distinctive effects. With its low energy physics determined by two small pockets of the Brillouin zone, it led scientists to realize that a new effective observable, namely the valley, emerges in many physical situations. This observable can be controlled and manipulated like the spin [Gunawan et al., 2006b, Gunawan et al., 2006a, Rycerz et al., 2007, Xiao et al., 2007, Yao et al., 2008] when the valley commutes with the dynamics of the low energy degrees of freedom. If the spectrum is gapped by breaking the inversion-symmetry of a honeycomb lattice, a unique topological effect named the QVHE emerges [Islam and Benjamin, 2016, Ren et al., 2016, Xiao et al., 2007]. It manifests in the emergence of counter-propagating quasi-chiral modes at the interface between two mirrored samples. QVHE is quite appealing for engineering interface modes because it does not require breaking of the time-reversal symmetry or the strong spin-orbit couplings. It has been observed in many solid-state devices [Mak et al., 2014, Gorbachev et al., 2014, Sui et al., 2015, Shimazaki et al., 2015, Ju et al., 2015] and the interest continues to be strong, especially in the field of graphene bilayers [Martin et al., 2008, Zhang et al., 2011a, Qiao et al., 2011, Wright and Hyart, 2011, Zhang et al., 2013, San-Jose and Prada, 2013, Vaezi et al., 2013, Huang et al., 2018]. It has been proposed in various photonic devices [Ma and Shvets, 2016, Dong et al., 2017, Chen et al., 2017, Bleu et al., 2017, Ni et al., 2018] and it was observed recently in laboratories [Gao et al., 2017, Noh et al., 2018, Kang et al., 2018]. QVHE has been enthusiastically embraced by the community of topological mechanics, where there has been an explosion of laboratory demonstrations of this effect [Lu et al., 2016, Lu et al., 2017, Pal and Ruzzene, 2017, Vila et al., 2017, Zhu et al., 2018a, Jiang et al., 2018b, Gao et al., 2018, Liu and Semperlotti, 2018, Wu et al., 2018, Chaunsali et al., 2018b, Chen et al., 2018]. We are particularly motivated by the work of [Pal and Ruzzene, 2017, Vila et al., 2017], where the mechanical interface modes have been recorded in real time, providing a dramatic visual demonstration of signal guiding along the zigzagged interfaces.

The bulk-boundary principle responsible for the observed interface modes is well understood in the regime where the valleys result from a slight splitting of graphene's Dirac cones [Qiao et al., 2011]. In such cases, the physics of low energy excitations can be captured by effective Dirac models, where the domain walls and the perturbations occur at small energy scales and over length scales much larger than that of the lattice parameters. This regime, unfortunately, is quite far from what is needed for practical applications of metamaterials, where the domain walls have to be sharp and the spectral gaps large in order to ensure good localization of the interface modes. We show these aspects using an experimental platform based on magnetically coupled spinners [Apigo et al., 2018]. Using the standard implementation of the QVHE based on nearest-neighbor couplings on a honeycomb-lattice system, we discover a fundamental conflict that the QVHE becomes weaker as the bulk energy gap increases. We experimentally demonstrate the existence of the interface modes and investigate their localization, providing undeniable evidence that practical constraints forces on the metamaterials scientists to exit the regime where Dirac physics applies. We also reproduce the forward propagation along a zigzagged interface, as observed in many studies before us, however, we, for the first time, demonstrate the backscattering of the interface modes under a lattice defect, which reveals that QVHE is a trivial (weak) topological effect.

The theory based on the Dirac physics supplies the following safe working conditions: the domain walls and the perturbations must occur at small energy scales and over length scales much larger than that of the lattice parameters. This is clearly not very useful for metamaterials applications. We discover a new regime that we name the valley-Chern effect (VCE), where a robust bulk-boundary principle can be established through topological arguments rather than effective models. This regime is characterized by large bulk spectral gaps and Berry curvature distributions that are entirely concentrated around the valley points. This requires Berry curvature engineering achievable only by turning on couplings beyond the nearest-neighbor couplings.

3.2 Experimental Platform

In this section, we describe the experimental platform to investigate different QVHE regimes obtained with the honeycomb-lattice platform.

3.2.1 Configurable Spinners

The configurable spinners in this work are shown in Figure 3.1. Three arms are fitted with magnets which provide the coupling between the spinners. Four types of spinner configurations are used in our study, displaying six, five, four and three arms, as shown in Figure 3.1(c-f). These types are referred to as A, B, C, and D, respectively.

3.2.2 Mapping the Basic Couplings

First, we will concentrate on three basic couplings: A-A, B-B and A-B. These magnetic couplings can be measured by mapping the resonant modes of the corresponding dimers. Similar to the description in Subsection 2.2.1, the dynamics of a dimer is governed by the Lagrangian:

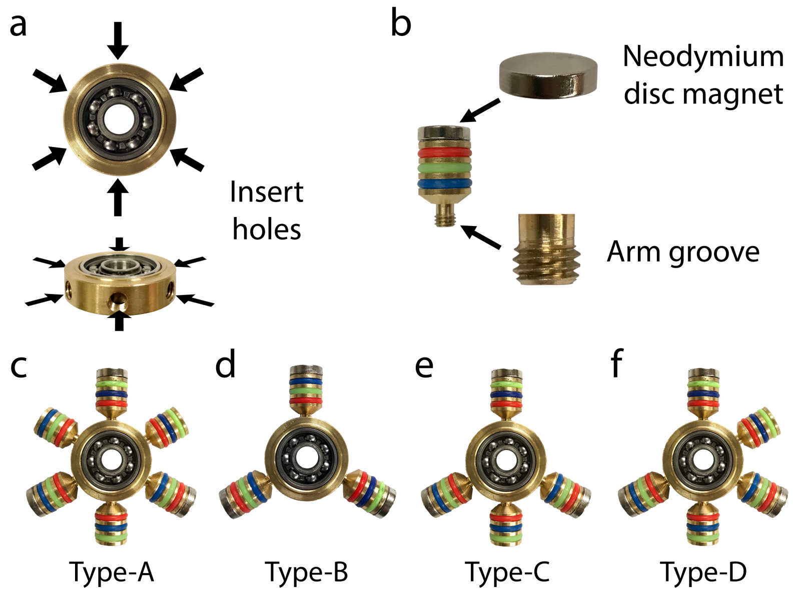

Figure 3.1 Configurable spinner with detachable arms. (a) Ball bearing with six inserts. (b) Detachable arms with magnetic ends for coupling. (c-f) The four spinner configurations used in our study, together with the labels used in the text. The quality factors of the coupled spinners are measured to be around 50. Source: [Qian et al., 2018].

$$L(\varphi_1, \varphi_2, \dot{\varphi}_1, \dot{\varphi}_2) = \tfrac{1}{2} I_1 \dot{\varphi}_1^2 + \tfrac{1}{2} I_2 \dot{\varphi}_2^2 - V(\varphi_1, \varphi_2). \tag{3.1}$$

In the regime of small oscillations around the equilibrium configuration, $\varphi_1 = \varphi_2 = 0$, the potential can be replaced by its quadratic approximation:

$$V(\varphi_1, \varphi_2) = V_0 + \tfrac{1}{2}\alpha(\varphi_1^2 + \varphi_2^2) + \beta \varphi_1 \varphi_2. \tag{3.2}$$

The symmetry of the potential with respect to the exchange $1 \leftrightarrow 2$ is made explicit in this expansion. Here, for stability, $|\beta| < \alpha$. Also, β is positive in our setup. The equations of motion are straightforward:

$$I_j \ddot{\varphi}_j + \alpha \varphi_j + \beta \varphi_{j'} = 0, \quad j = 1, 2, \quad j' = 2, 1. \tag{3.3}$$

With the ansatz $\varphi_j(t) = \frac{1}{\sqrt{I_j}} A_j e^{i\omega t}$, $\omega = 2\pi f$, the equation for the resonant modes reads:

$$\omega^2 \begin{pmatrix} A_1 \\ A_2 \end{pmatrix} = \begin{pmatrix} \frac{\alpha}{I_1} & \frac{\beta}{\sqrt{I_1 I_2}} \\ \frac{\beta}{\sqrt{I_1 I_2}} & \frac{\alpha}{I_2} \end{pmatrix} \begin{pmatrix} A_1 \\ A_2 \end{pmatrix}. \tag{3.4}$$

For $I_1 = I_2 = I_A$ or I_B, it leads to the pairs of resonant frequencies:

$$f_\pm^{A-A} = \sqrt{\frac{\alpha \pm \beta}{4\pi^2 I_A}}\,, \quad f_\pm^{B-B} = \sqrt{\frac{\alpha \pm \beta}{4\pi^2 I_B}}. \tag{3.5}$$

The upper and lower frequency modes correspond to motions where the two angles are locked as $\varphi_2 = \pm\varphi_1$, respectively.

The resonant frequencies have been independently measured as functions of distance d between the magnets and the data is reported in Figure 3.2(c-d). We have verified that the coupling coefficients are not affect by the removal of the arms, by examining the ratios $\frac{f_\pm^{B-B}}{f_\pm^{A-A}}$. As one can see in Figure 3.2(e), these two ratios are more or less identical and independent of d. From Equation (3.5), this constant value can be identified with the ratio $\sqrt{\frac{I_A}{I_B}}$, which comes to 1.235 from a fit. At this point, we obtained a quantitative measure of $r = \frac{I_A}{I_B} = 1.525$. Furthermore, it is possible to invert any of the relations in Equation (3.5), *e.g.* A-A, and map the coupling coefficients:

$$\alpha = 2\pi^2 I_A \Big(f_+^2 + f_-^2\Big), \quad \beta = 2\pi^2 I_A \Big(f_+^2 - f_-^2\Big). \tag{3.6}$$

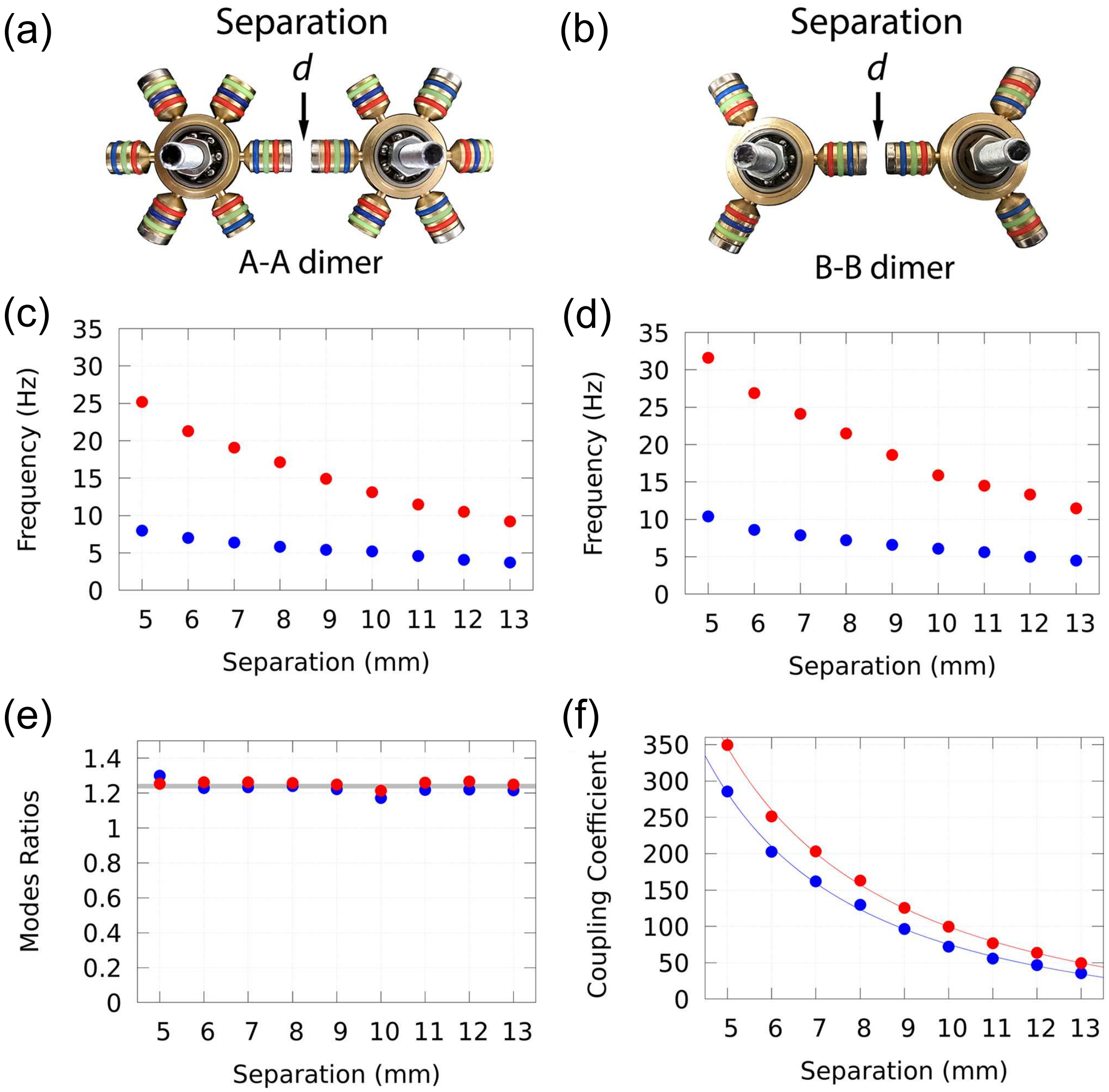

Figure 3.2 Mapping the coupling coefficients. (a-b) The A-A and B-B dimmer configurations, respectively. (c) The experimentally measured resonant frequencies $f_{\pm}^{A-A}$ (red/blue dots, respectively) of the A-A dimer as functions of separation d between the magnets. (d) Same as (c) but for B-B dimer. (e) The ratios $\frac{f_+^{B-B}}{f_+^{A-A}}$ (red dots) and $\frac{f_-^{B-B}}{f_-^{A-A}}$ (blue dots) as function of separation. (f) The coupling coefficients α (solid red dots) and β (solid blue dots), as derived from Equation (3.6) in units of $2\pi^2 I_A \times \mathrm{Hz}^2$, together with the analytic fits Equation (3.7) (continuous lines). Source: [Qian et al., 2018].

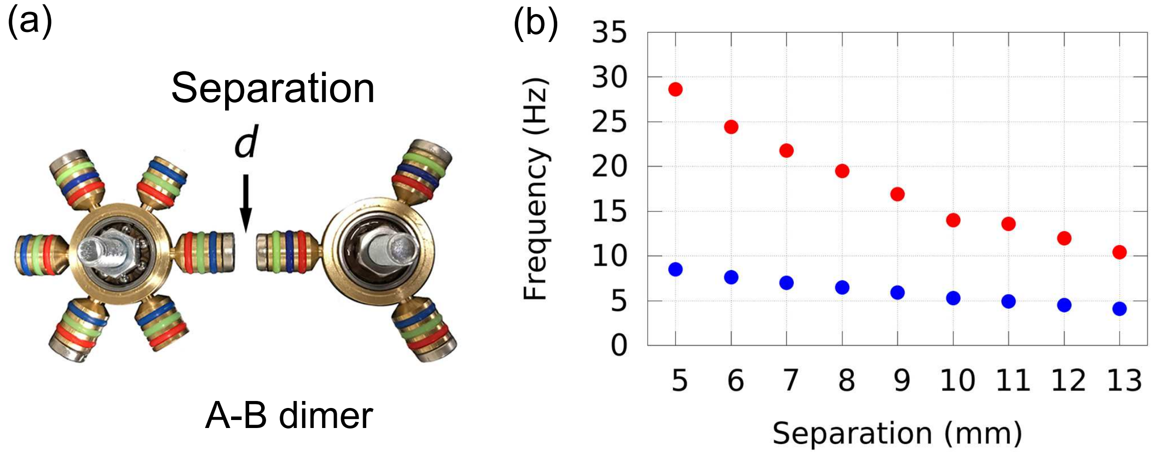

Figure 3.3 The A-B coupling. (a) The A-B dimer configuration. (b) The experimentally measured resonant frequencies $f_{\pm}^{A-B}$ as function of distance between the magnets. Source: [Qian et al., 2018].

The resulting values are shown in Figure 3.2(f), in the units of $2\pi^2 I_A \times \mathrm{Hz}^2$, together with the theoretical fits:

$$\begin{aligned} \alpha(d) &= -\tfrac{778.14}{\sqrt{d}} + \tfrac{3439.81}{d} + \tfrac{161.35}{d^2}, \\ \beta(d) &= -\tfrac{654.09}{\sqrt{d}} + \tfrac{2763.66}{d} + \tfrac{575.89}{d^2}. \end{aligned} \tag{3.7}$$

For completeness, the resonant frequencies for the A-B dimer are reported in Figure 3.3(b). They agree well with the coupling coefficients Equation (3.7). Similar measurements have been performed for the combinations A-C and A-D, for which the coupling coefficients remain the same and r was found to be approximately 1.3 and 1.2, respectively.

3.3 QVHE with Coupled Spinners

We generate the QVHE with the classical honeycomb configuration. The fully assembled spinner system in the A-B configuration is shown in Figure 3.4, together with the primitive cell and primitive vectors. The centers of the primitive cells are located at $\boldsymbol{R_n} = n_1\boldsymbol{a}_1 + n_2\boldsymbol{a}_2$, hence we can label the cells by $\boldsymbol{n} = (n_1, n_2) \in \mathbb{Z}^2$. The spinners can be easily identified using the pair of indexes $(\boldsymbol{n}, A)$ or $(\boldsymbol{n}, B)$. The shift operations acting on the indices:

$$
\begin{aligned}
S_1\boldsymbol{n} &= S_1(n_1, n_2) = (n_1 + 1, n_2), \\
S_2\boldsymbol{n} &= S_2(n_1, n_2) = (n_1, n_2 + 1),
\end{aligned}
\tag{3.8}
$$

will prove to be convenient for the calculations below.

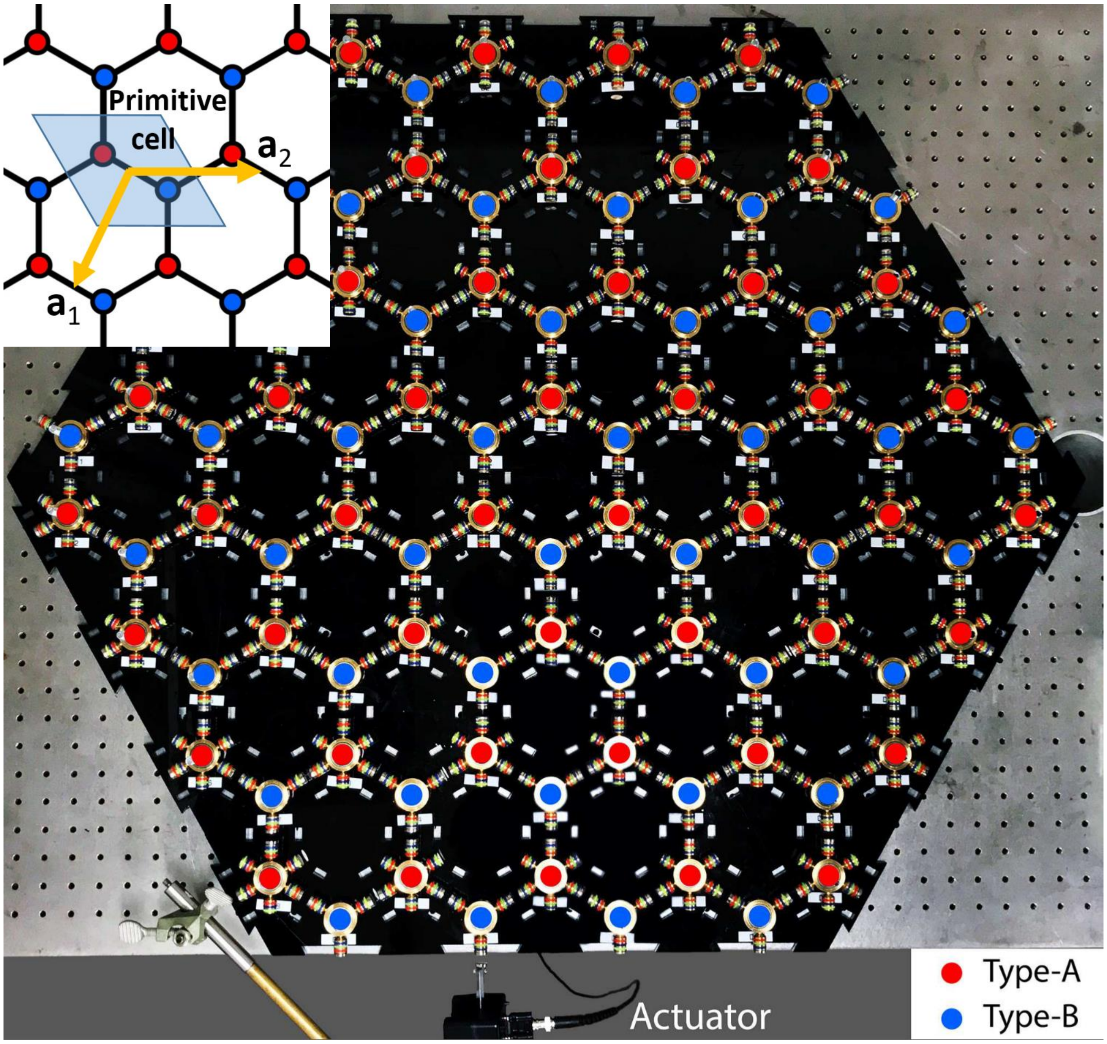

Figure 3.4 Bulk configuration. It is a finite bipartite honeycomb lattice populated with A (red) and B (blue) type spinners. The actuator appears at the bottom of the illustration. The inset shows the primitive cell (shaded region) and the primitive vectors $\boldsymbol{a}_1$ and $\boldsymbol{a}_2$ in yellow. Source: [Qian et al., 2018].

3.3.1 Mapping the Bulk Spectrum

The Lagrangian of the infinite lattice takes the form:

$$
\begin{aligned}
L = \sum_{\boldsymbol{n}\in\mathbb{Z}^2} \Big(& \tfrac{1}{2} I_A \dot{\varphi}^2_{\boldsymbol{n},A} + \tfrac{1}{2} I_B \dot{\varphi}^2_{\boldsymbol{n},B} - V(\varphi_{\boldsymbol{n},A}, \varphi_{\boldsymbol{n},B}) \\
& - V(\varphi_{\boldsymbol{n},A}, \varphi_{S_1^{-1}S_2^{-1}\boldsymbol{n},B}) - V(\varphi_{\boldsymbol{n},A}, \varphi_{S_2^{-1}\boldsymbol{n},B}) \Big),
\end{aligned}
\tag{3.9}
$$

and, using the quadratic approximation Equation (3.2), the equations of motions take the form:

$$
\begin{pmatrix} I_A \ddot{\varphi}_{\boldsymbol{n},A} \\ I_B \ddot{\varphi}_{\boldsymbol{n},B} \end{pmatrix} = \begin{pmatrix} -3\alpha\varphi_{\boldsymbol{n},A} - \beta(\varphi_{\boldsymbol{n},B} + \varphi_{S_1^{-1}S_2^{-1}\boldsymbol{n},B} + \varphi_{S_2^{-1}\boldsymbol{n},B}) \\ -3\alpha\varphi_{\boldsymbol{n},B} - \beta(\varphi_{\boldsymbol{n},A} + \varphi_{S_1S_2\boldsymbol{n},A} + \varphi_{S_2\boldsymbol{n},A}) \end{pmatrix}. \tag{3.10}
$$

It is convenient to make the change of variables:

$$
\varphi_{\boldsymbol{n},A} = \frac{1}{\sqrt{I_A}}\psi_{\boldsymbol{n},A}, \quad \varphi_{\boldsymbol{n},B} = \frac{1}{\sqrt{I_B}}\psi_{\boldsymbol{n},B}, \tag{3.11}
$$

and bring the equations to the form:

$$
\begin{pmatrix} \ddot{\psi}_{\boldsymbol{n},A} \\ \ddot{\psi}_{\boldsymbol{n},B} \end{pmatrix} = \begin{pmatrix} -3\frac{\alpha}{I_A}\psi_{\boldsymbol{n},A} - \frac{\beta}{\sqrt{I_A I_B}}(\psi_{\boldsymbol{n},B} + \psi_{S_1^{-1}S_2^{-1}\boldsymbol{n},B} + \psi_{S_2^{-1}\boldsymbol{n},B}) \\ -3\frac{\alpha}{I_B}\psi_{\boldsymbol{n},B} - \frac{\beta}{\sqrt{I_A I_B}}(\psi_{\boldsymbol{n},A} + \psi_{S_1S_2\boldsymbol{n},A} + \psi_{S_2\boldsymbol{n},A}) \end{pmatrix} \tag{3.12}
$$

We can encode the degrees of freedom in a single function:

$$\boldsymbol{\psi} : \mathbb{Z}^2 \to \mathbb{C}^2, \quad \boldsymbol{\psi}(\boldsymbol{n}) = \begin{pmatrix} \psi_{\boldsymbol{n},A} \\ \\ \psi_{\boldsymbol{n},B} \end{pmatrix}, \tag{3.13}$$

and use the ansatz $\boldsymbol{\psi}(t) \to \mathrm{Re}\Big[e^{i\omega t}\boldsymbol{\psi}\Big]$, $\omega = 2\pi f$. Then, in the units used in Figure 3.2(f), the equations of motions simplify to:

$$\begin{gathered} f^2\boldsymbol{\psi} = \Big[\tfrac{3}{2}\alpha\Big(1 + r + (1-r)\sigma_3\Big) \\ +\beta\sqrt{r}\Big(\sigma_1 + \sigma_-(S_1S_2 + S_2) + \sigma_+(S_1^\dagger S_2^\dagger + S_2^\dagger)\Big)\Big]\boldsymbol{\psi}, \end{gathered} \tag{3.14}$$

where the shift operators act as:

$$(S_j\boldsymbol{\psi})(\boldsymbol{n}) = \boldsymbol{\psi}(S_j\boldsymbol{n}), \quad j = 1,2, \tag{3.15}$$

and σ's are Pauli's matrices. The shift operators commute with each other and also with the dynamical matrix, and have common eigenvectors:

$$S_j\, e^{i\boldsymbol{k}\boldsymbol{n}} = e^{ik_j}e^{i\boldsymbol{k}\boldsymbol{n}}, \quad \boldsymbol{k} = (k_1,k_2) \in [-\pi,\pi]^2, \quad j = 1,2. \tag{3.16}$$

Hence, the normal modes will be sought in the form $\boldsymbol{\psi}(\boldsymbol{n}) = e^{i\boldsymbol{k}\boldsymbol{n}}\,\xi, \xi \in \mathbb{C}^2$, in which case the dispersion equation reduces further to:

$$f^2\xi = \left(\tfrac{3}{2}\alpha\Big(1 + r + (1-r)\sigma_3\Big) + \beta\sqrt{r}\begin{pmatrix} 0 & \gamma(\boldsymbol{k})^* \\ \gamma(\boldsymbol{k}) & 0 \end{pmatrix}\right)\xi, \tag{3.17}$$

with $\gamma(\boldsymbol{k}) = 1 + e^{i(k_1+k_2)} + e^{ik_2}$. The explicit dispersion equations of the resonant modes then follow:

$$f_\pm = \tfrac{3\alpha}{2}\left[(1+r) \pm \sqrt{(1-r)^2 + \tfrac{4r\beta^2}{9\alpha^2}|\gamma(\boldsymbol{k})|^2}\,\right]^{\frac{1}{2}}. \tag{3.18}$$

When $r = 1$, the system is inversion symmetric and two Dirac singularities are present in the bulk band structure. The imbalance between I_A and I_B breaks the inversion symmetry, hence the Dirac singularities split as soon as $r > 1$. The valleys are located at the points where $|\gamma(\boldsymbol{k})| = 0$, which are $K = -K' = (\frac{2\pi}{3}, -\frac{2\pi}{3})$.

A graphical representation of the dispersion equations (3.18) is reported in Figure 3.5 for a sequence of increasing values of r. For the value $r = 1.525$ corresponding to the A-B configuration, a comparison between the theoretical spectrum and the experimental reading from an induction coil sensor placed inside the structure is shown in Figure 3.6. Since the structure is actuated from the edge, a non-zero reading from the sensor indicates that the actuating frequency belongs to the bulk spectrum, while a zero reading indicates that it is in a spectral gap. The predicted spectral gap in Figure 3.6(a) is confirmed by the experimental result in Figure 3.6(b) within 1%.

There are several important observations about the bulk dynamics. First, in Equations (3.18), the depth of the valleys is set by the ratio of $\frac{\beta}{\alpha}$, once r is fixed. The larger this ratio the deeper the valleys, but note that $\frac{\beta}{\alpha} < 1$, so with nearest-neighbor

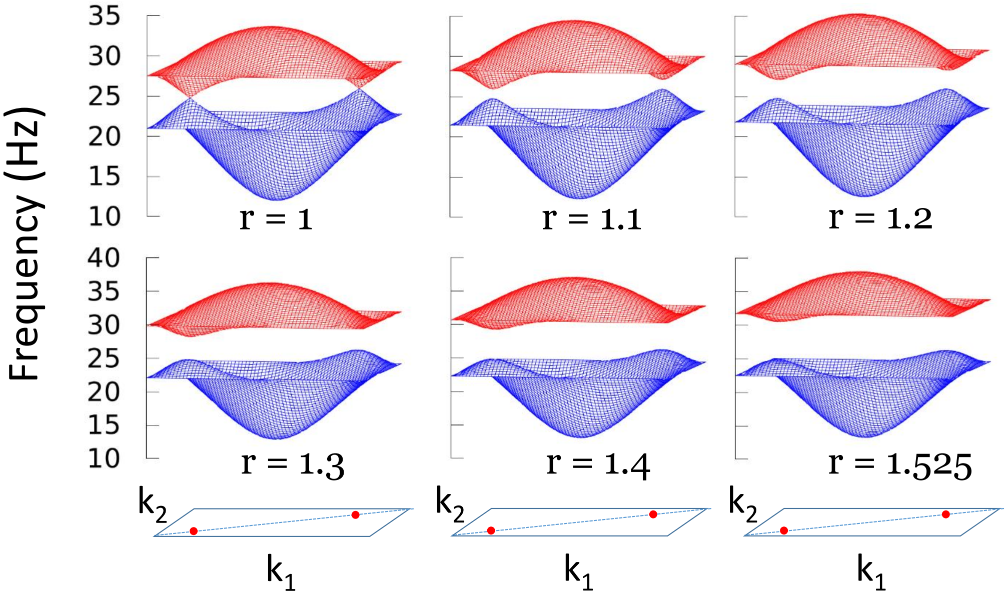

Figure 3.5 Predicted bulk band spectra. Plots of the dispersion equations (3.18) for various values of the ratio $r = \frac{I_A}{I_B}$. The graphs are rendered as functions of $(k_1, k2) \in [-\pi, \pi]^2$ and the red dots indicate the position of the valleys points K and K'. Source: [Qian et al., 2018].

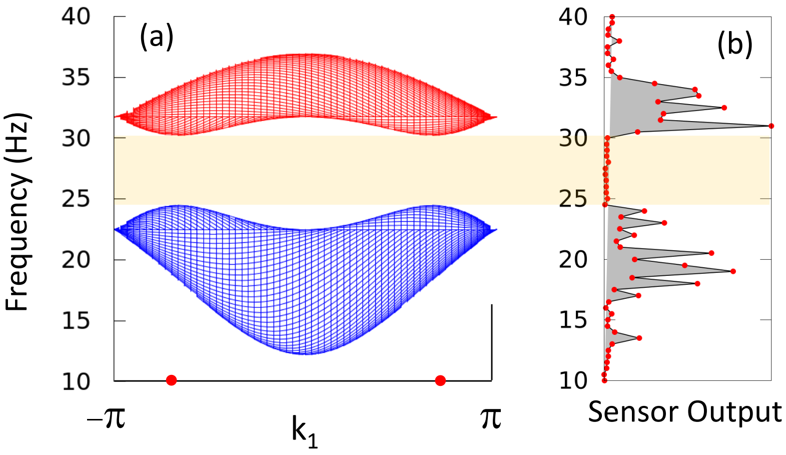

Figure 3.6 Predicted versus measured bulk spectrum. (a) The theoretical data taken from the last panel of Figure 3.5 ($r = 1.525$). The view point is chosen here such that k_2 is into the page and the red dots indicate the position of the valleys K and K'. (b) The reading from a sensor placed inside the spinner structure when the system is actuated from the edge. The shaded region in beige marks the spectral gap, which is consistent between theoretical and experimental results. Source: [Qian et al., 2018].

couplings on the honeycomb lattice, there is an upper limit on the sharpness of the valleys. For our experimental system, $\frac{\beta}{\alpha} = 0.8$, which can be placed among the most optimized systems ever produced. Hence, the conclusions we draw based on our experimental setup have quite a broad relevance. Second, while the dynamical matrix in Equation (3.17) can be indeed approximated by a Dirac Hamiltonian around the valleys K and K', by a simple linear expansion, the region on which this approximation holds reduces drastically with the increase of r. This can be already seen by examining the spectra in Figure 3.5, from where we conclude that treating QVHE with the effective Dirac approximation is questionable at and beyond $r = 1.2$.

3.3.2 Berry Curvature

A graphical representation of Berry curvature is reported in Figure 3.7 for various values of the parameter r. There are several important remarks here. First, as expected, if the inversion symmetry is only slightly broken, such as when $r = 1.05$, we see that the Berry curvature is strongly localized near the valleys. But as r is increased, this localization becomes worse. This somewhat surprising rapid decrease is due to in part to the slow decay at infinity of the Berry curvature supported by a split Dirac cone. This shows that one has to be cautious when using Dirac effective models for and beyond $r = 1.2$. Furthermore, it becomes quite apparent that robust QVHE, primed for applications, cannot be generated via simple Dirac cone splittings and instead it will require sophisticated Berry curvature engineering. The above warning signs apply to any model based on nearest-neighbor couplings on honeycomb lattice.

3.3.3 Domain Walls

The experimental setup with a straight domain wall is shown in Figure 3.8. A schematic and more geometrical data are shown in Figure 3.9. It is important to note that the previously chosen primitive cell and vectors are consistent with the domain wall, in the sense that the

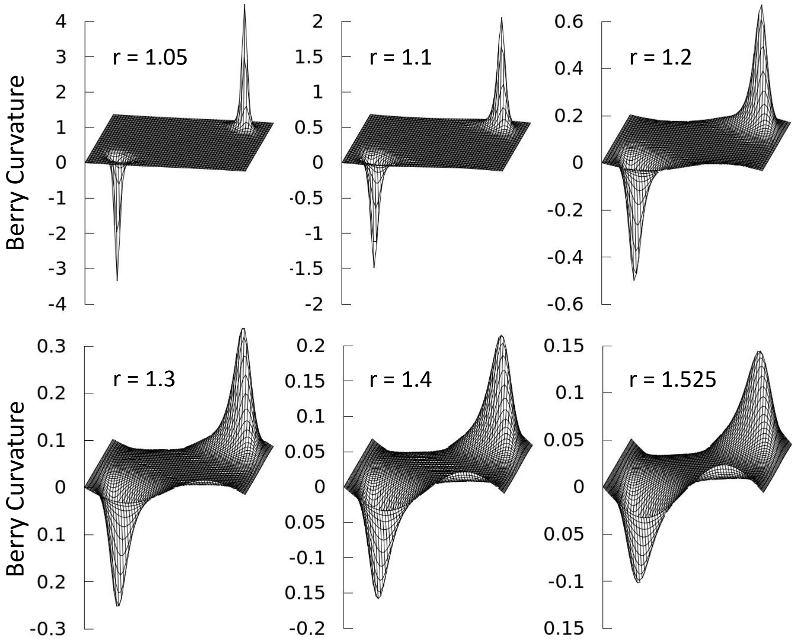

Figure 3.7 Berry curvature. The theoretical calculations were performed with the experimental values of the coupling constants α and β and for the specified values of $r = I_A/I_B$. The last value $r = 1.525$ is used in the experimental demonstrations. The data is rendered as function of (k_1, k_2) whose axes are not shown. Source: [Qian et al., 2018].

domain does not slices the unit cell and the primitive vector $\boldsymbol{a}_1$ is parallel to the domain wall.

The resulting spectrum for the domain wall configuration of Figure 3.8 is reported in Figure 3.10, which reproduces the well-known QVHE features. First thing to notice is that the domain wall modes do not dive into the bulk spectrum but rather get connected at higher and lower energies. This is one difference between this effect and a true topological effect. Also, as r is increased, the bulk gap increases, strengthening the localization of the interface modes along the domain wall. However, unfortunately, the domain wall bands move away from the bulk spectrum and the system will eventually become gapped. Another important aspect is the separation of the propagating and counter-propagating with respect to k, since a better separation implies less backscattering. Recalling that k actually live on a circle, then, ideally, one will like to pick a frequency where $k = \pm\frac{\pi}{2}$, and we can do that only with

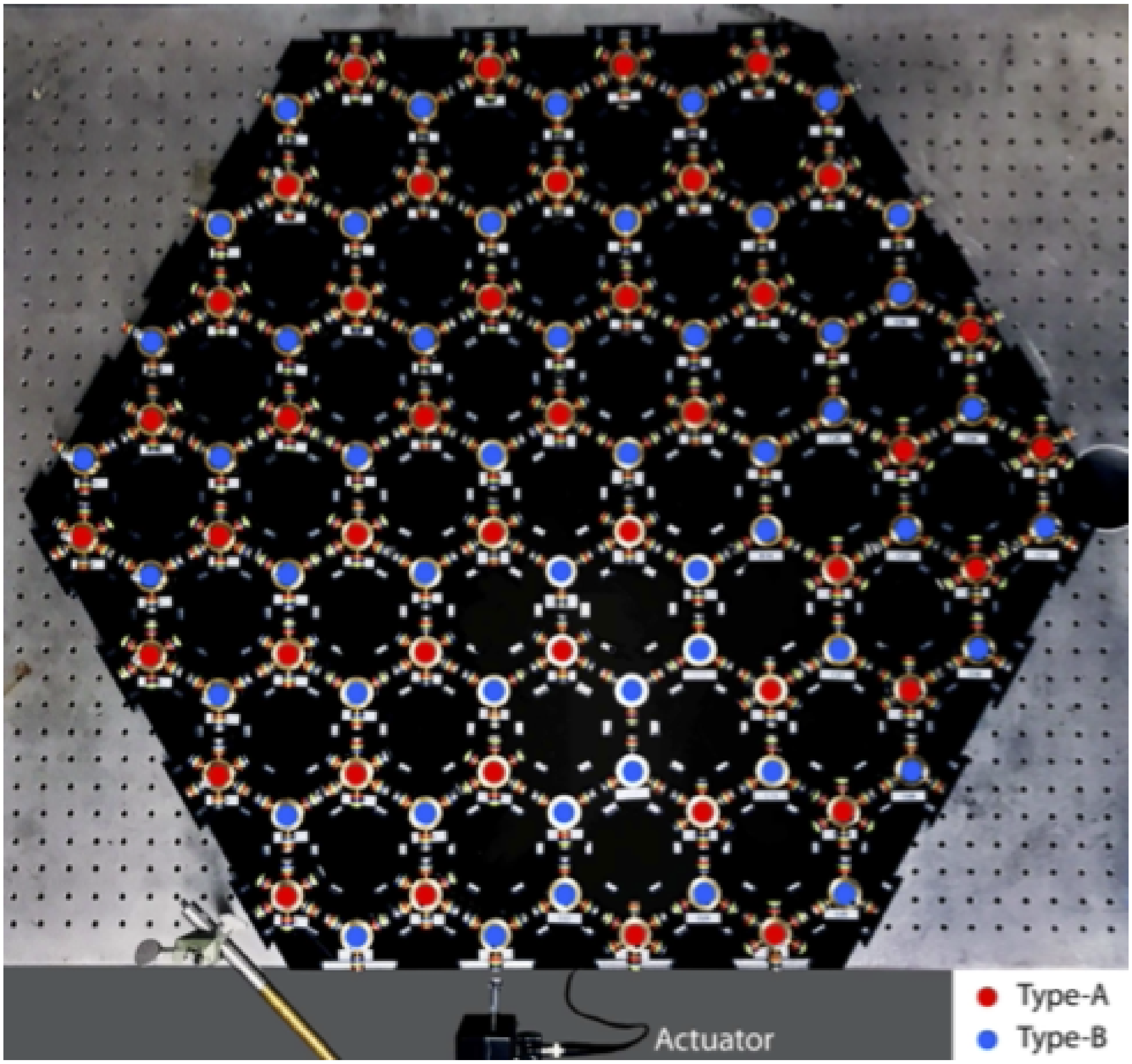

Figure 3.8 The experimental setup with a straight domain wall. The domain wall consists of the zigzag chain of B type (blue) spinners. Note the actuator positioned at one end of the domain wall. Source: [Qian et al., 2018].

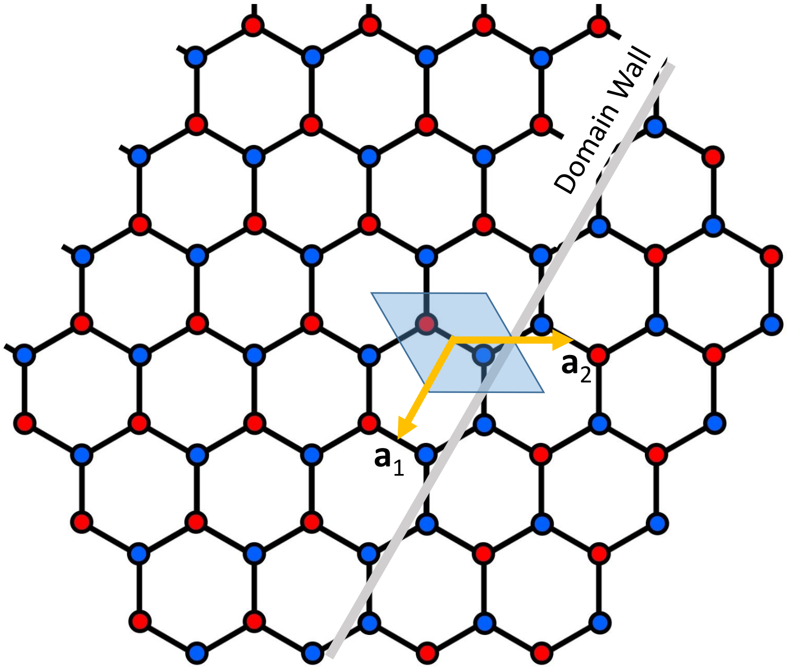

Figure 3.9 Schematic of the domain wall. Note that the domain wall does not cut any of the primitive cells. Source: [Qian et al., 2018].

$r = 1.525$. The experiment confirms that the most robust QVHE is indeed obtained at the mid-gap frequency of the A-B configured system.

3.3.4 Experimental Observation of the Domain Wall Modes

The domain wall has been actuated from one end, as shown in Figure 3.8, until a stationary regime is established. In this setup, the counter-propagating domain wall modes are scattered into each other at the ends of the interface, leading to a standing wave. Pickup coils similar to the ones found in electric guitars have been placed on top of the bonds and the standing wave pattern is mapped out. Four magnetic bonds in the $\boldsymbol{a}_2$ direction have been probed, starting from the domain wall, enough to assess the spatial localization of the modes.

The experimental results are reported in Figure 3.11. One can see that, for frequencies up to 25.0 Hz, the sensors return only small motion amplitudes. These frequencies must be within or very close to the bulk spectrum in which case the signal from the actuator disperses throughout the entire lattice, hence explaining the small amplitudes. Beyond 25.0

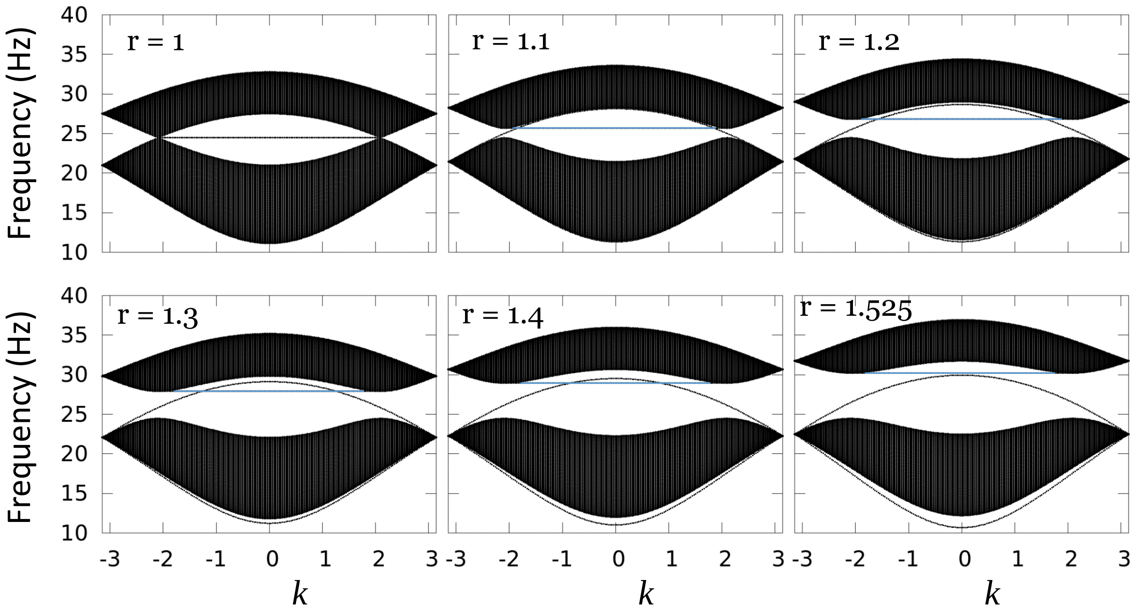

Figure 3.10 Predicted spectrum in the presence of a domain-wall. Simulations are shown for increasing values of $r = \frac{I_A}{I_B}$, ranging from 1 all the way to the experimental value of 1.525. The spectrum is computed on a strip with the domain-wall at the center. The doubly degenerated flat band seen in all panels is located at the edges of the ribbon, hence it is unrelated to the physics studied here. Source: [Qian et al., 2018].

Hz, the sensors pickup strong amplitudes near the interface and the amplitudes are seen to fade away into the bulk. We are definitely witnessing a standing wave supported by the interface channel. The strongest resonant patterns are observed within the range of frequencies from 28.0 to 29.0 Hz. Above this range, the sensor readings fade away again since the frequency approaches the upper part of the bulk spectrum.

The domain wall modes in QVHE are known to be robust against spatially slow deformations of the interface. However, it has been reported with many occasions [Lu et al., 2016, Lu et al., 2017, Pal and Ruzzene, 2017, Vila et al., 2017, Zhu et al., 2018a, Jiang et al., 2018b, Liu and Semperlotti, 2018, Wu et al., 2018, Chaunsali et al., 2018b, Chen et al., 2018] that a signal can propagate along the domain wall channels with very little backreflection even if the interface is bent sharply. To investigate this interesting and potentially important effect, we reconfigured our A-B system in the L-shaped domain wall configuration shown in Figure 3.12. The measurements have been repeated and the results

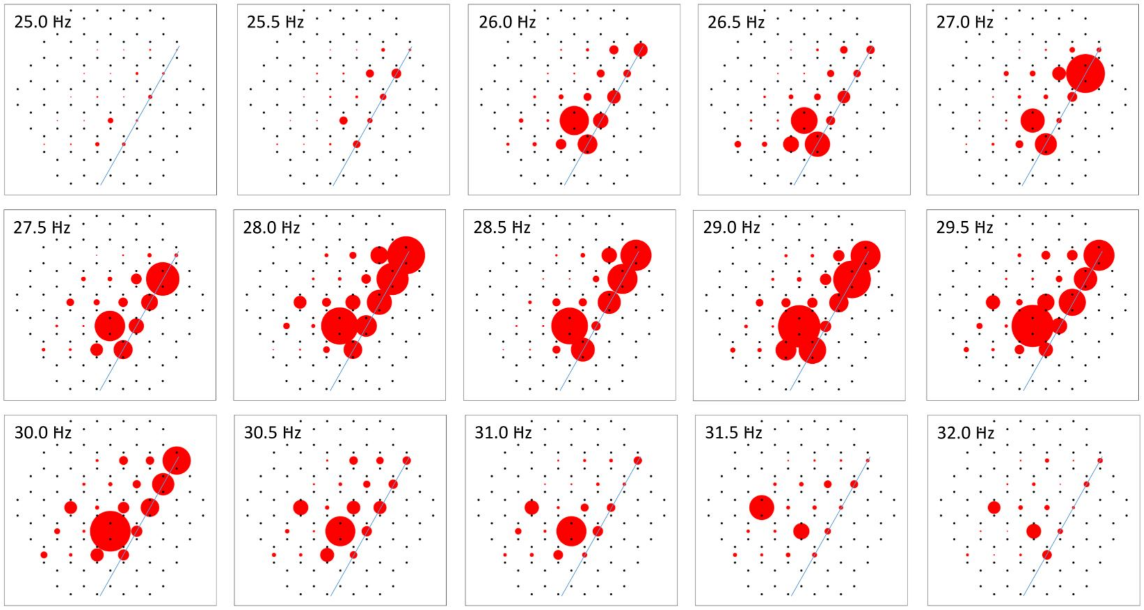

Figure 3.11 Experimental observation of the domain wall modes. The fine line marks the position of the interface relative to the honeycomb lattice, indicated by the black dots. The red disks mark the position of the motion sensors, which are placed above bonds. The size of a disk is proportional with the reading of the motion sensor at that location. The frequencies, which are marked in each panel, sample the entire bulk gap. The measurement are for the A-B system ($r = 1.525$). Source: [Qian et al., 2018].

are reported in Figure 3.13. As many before us, we find that, indeed, there is a healthy transmission of the signal beyond the corner of the L-shaped domain wall. Judging by the amplitudes seen along the two arms of the L-shaped (see especially the panels $f = 28.5$ Hz and $f = 29.0$ Hz), we concluded that the transmission is only about 90%.

We also report a comparison between the most robust domain wall modes we could generate with A-B ($r = 1.525$), A-C ($r = 1.3$), and A-D ($r = 1.2$) systems. Given that the actuation was identical, their difference is striking. Indeed, for $r = 1.525$ case, the mode is highly localized and the amplitude of the oscillations is substantial, while for the $r = 1.3$ and $r = 1.2$ cases, the mode is quite delocalized and, because of that, the amplitudes of the oscillations are much smaller. In fact, with $r = 1.2$ it was difficult to observe the domain wall mode. The inherent conclusion is that the regime $r < 1.2$, where the effective Dirac models apply, is interesting for demonstration purposes but has little relevance for the practical applications.

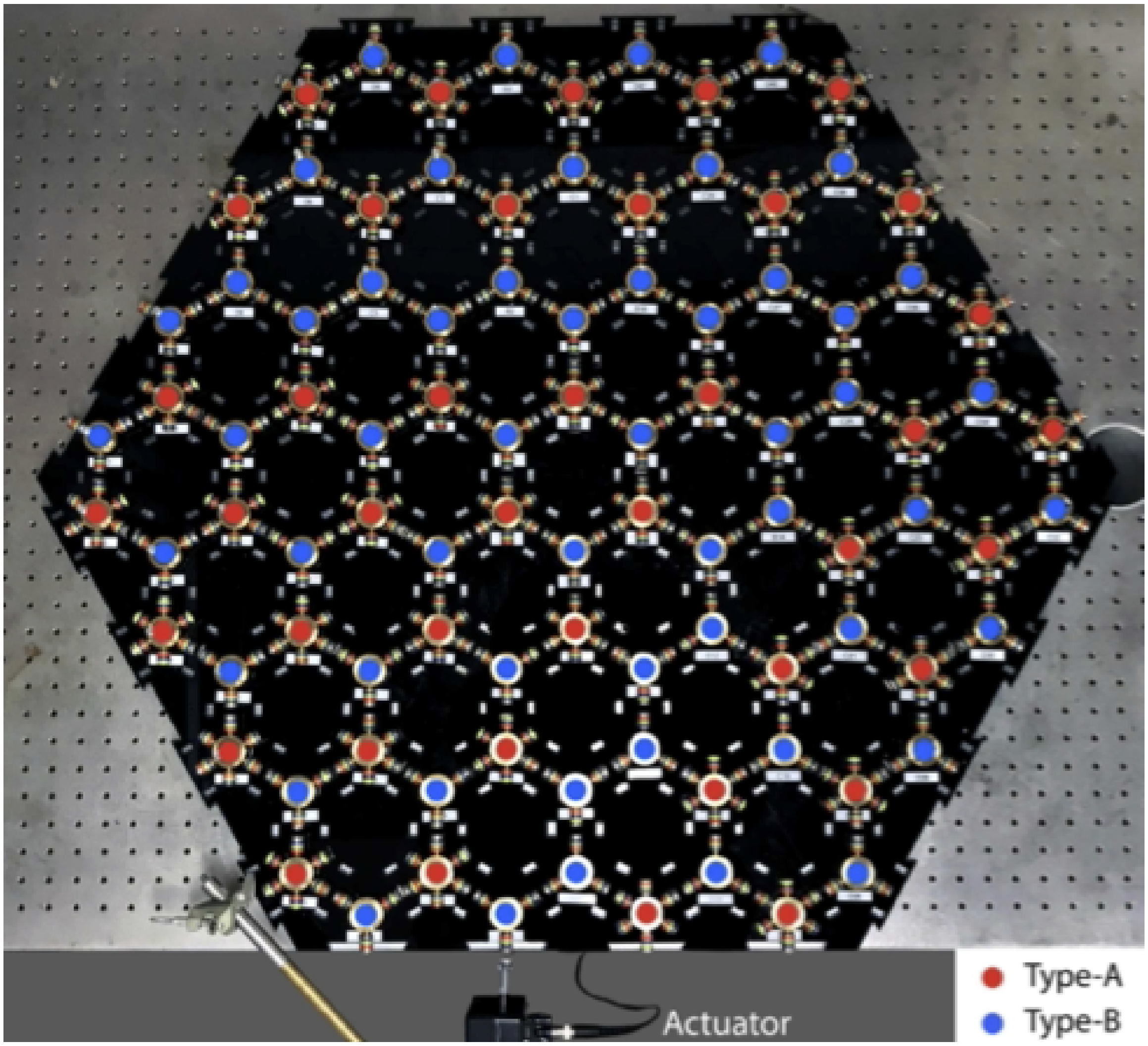

Figure 3.12 The experimental setup with a L-shaped domain wall. The domain wall consists of the zigzag chain of B type (blue) spinners. The actuator positioned at one end of the domain wall. Source: [Qian et al., 2018].

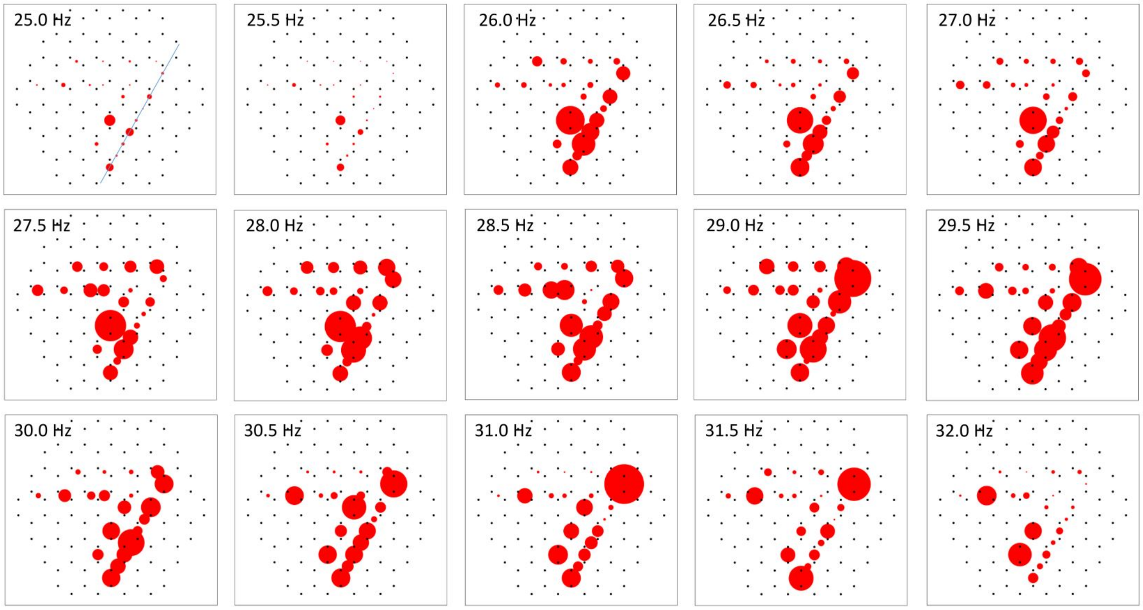

Figure 3.13 Experimental observation of the L-shaped domain wall modes. Except for the shape of the interface, the rest of the details are shown in Figure 3.12. Source: [Qian et al., 2018].

3.4 Summary

This study experimentally demonstrates how breaking inversion symmetry within the unit cell can lead to topological band gaps in a discrete mechanical system. However, a fundamental difficulty is uncovered in the current implementations of the QVHE. More precisely, the designs based on nearest-neighbor couplings on a honeycomb lattice will inherently fail one of the following tests: (1) Berry curvature localization around the valleys, (2) localization of the domain wall modes along the interface, and (3) lack of back-scattering of domain wall modes under lattice defects. To correct for these shortcomings, a certain Berry curvature engineering through couplings beyond nearest-neighbor, for large bulk spectral gaps and Berry curvature distributions localized near the valleys, is believed to be a solution, which is a new regime that we name the valley-Chern effect [Qian et al., 2018]. For this regime, genuine chiral domain modes can be achieved by adjusting the domain wall potential. As the program of Berry curvature engineering is yet to be developed, at this point, we can only provide predictions and recommendations for implementations of the true VCE.

CHAPTER 4

TOPOLOGICAL FLAT BANDS IN MECHANICAL METAMATERIALS

In this chapter, we will demonstrate the realization of topological flat frequency bands in a series of topological mechanical metamaterials based on a recently proposed 2D electronic model. The work was in collaboration with Dr. Linghua Zhu, Prof. Keun Hyuk Ahn, and Prof. Camelia Prodan from the Department of Physics at New Jersey Institute of Technology.

4.1 Introduction

Flat energy bands have been the focus of intense research in photonic crystals, such as the Lieb lattice, due to the possibility of trapping photons, which has technological significance [Lieb, 1989, Wiersma, 2015, Vicencio et al., 2015, Mukherjee et al., 2015, Klembt et al., 2017, Leykam and Flach, 2018, Leykam et al., 2018, Lazarides and Tsironis, 2019]. They have also gained a lot of attention [Kariyado and Slager, 2019] following the discovery of superconductivity in twisted bilayer graphenes [Bistritzer and MacDonald, 2011, Cao et al., 2018a, Cao et al., 2018b, Po et al., 2018, Yankowitz et al., 2019] and the pursuit of nearly flat bands in the fractional Chern insulators [Tang et al., 2011, Neupert et al., 2011, Sun et al., 2011, Wang and Ran, 2011, Liu et al., 2012, Wang et al., 2012]. Recently, there has been a theoretical proposal for flat energy bands of topological origin within antiphase and twin boundaries and at open edges in a system described by a 2D electronic tight-binding model Hamiltonian [Zhu et al., 2019]. Unlike the Lieb lattice, the flat band states occur only at edges or domain boundaries, giving a unique controllability through patterning. Unlike twisted bilayer graphenes or fractional Chern insulators, the flatness of the bands in the entire projected reciprocal space does not require tuning of parameters. We experimentally demonstrate the realization of the Hamiltonian and the flat bands in the metamaterials by using mechanical systems made of interacting spinners [Apigo et al., 2018, Qian et al., 2018].

By examining how the width of the edge band narrows in frequency as the edge-to-edge distance increases, we show the presence of the topological flat frequency bands at the edges. It is revealed that the size of the localized excitations at the edges correlates with the width of the edge band. The analog to electronic charge fractionalization [Asbóth et al., 2016] is also found. Additionally, we experimentally verify the presence of a mid-gap mode at the antiphase boundary seam of a ring-shaped spinner system, and computationally find a flat antiphase boundary seam band for a tubular system.

Systems of magnetically coupled spinners are versatile experimental platforms for various Hamiltonians [Apigo et al., 2018, Qian et al., 2018]. In mapping between electronic tight-binding Hamiltonians and magnetically coupled spinner systems, the intersite electron hopping corresponds to the interspinner magnetic interaction controlled by the distance between the magnets. The electronic model Hamiltonians for the flat bands at open edges and antiphase/twin boundaries [Zhu et al., 2019] are based on a particular 2D extension of the SSH model [Su et al., 1979]. Unlike other 2D SSH models [Xie et al., 2018, Delplace et al., 2011], SSH chains with alternating intersite hopping strengths are shifted and stacked in the direction perpendicular to the chains. With only the first neighbor hoppings, the 2D system preserves the chiral symmetry of the 1D SSH system. With the constant *interchain* coupling weaker than the average *intrachain* coupling, a gap opens between two bulk bands and the topology of the system is characterized by the winding number, which depends on the direction of edges or boundaries. The bulk-boundary correspondence predicts flat zero energy edge or boundary bands of bipartite states for the chiral 2D SSH system, similar to the 1D SSH system.

4.2 Flat Frequency Bands at Open Edges

4.2.1 Configuration of Systems

One of the 2D spinner systems and its schematic diagram are shown in Figures 4.1(a) and 4.1(b). With magnets attached to the 0°, 60°, 180°, and 240°direction arms and the spinners arranged in quasi-triangular lattices, the systems are equivalent to the electronic systems of quasi-square lattices [Zhu et al., 2019] with hoppings in the $0°$, $90°$, $180°$, and $270°$directions. The systems are assembled with the edges in the $0°$and $120°$directions, equivalent to the $0°$and $135°$directions for the quasi-square systems. The spinners are indexed as (n_1, n_2) with $n_1 = 1, ..., N_1$ and $n_2 = 1, ..., N_2$ (Figure 4.1(b)). The SSH chains run along the $0°$direction with alternating intrachain couplings, represented by the red and the blue lines in Figure 4.1(b). The chains are coupled along the $60°$direction with a constant interchain coupling, represented by the green lines. A unit cell is marked in purple. If the interchain coupling is weaker than the average intrachain coupling, and the interaction within the unit cell is weaker [stronger] than the interaction between the unit cells within the same chain, the system becomes a topological [nontopological] insulator (see Section 4.5 Supplementary Material for further information on theoretical analyses and adequacy of the chosen spinner system sizes). For chiral symmetry, fixed spinners with necessary interactions are placed around the edges, as shown in Figures 4.1(a) and 4.1(b). One of the spinners is driven by the interaction between a magnet on either $120°$or $300°$direction arm and a magnet on the actuator. The voltage from an attached accelerometer divided by the square of the frequency is used as a quantity proportional to the oscillation amplitude of the spinner.

With parameters from our previous work [Apigo et al., 2018, Qian et al., 2018], the spectra are calculated to decide which spinners to actuate and measure, so that the bulk and edge band widths are well represented. Actuating and measuring at the $(N_1, 2)$ spinner [$(N_1 - 1, 1)$ spinner] gives the spectrum that represents the edge [bulk] band width well for the topological systems. By choosing the intermagnet distances of 5.0, 8.0, and 9.0 mm for red, blue, and green lines, respectively, as shown in Figure 4.1(b), we realize topological systems with the winding numbers $\nu(120°) = 1$ and $\nu(0°) = 0$, where topological edges in 120°direction, and by choosing 8.0, 5.0, and 9.0 mm, nontopological with $\nu(120°) = \nu(0°) = 0$ [Zhu et al., 2019]. The theoretical analysis for the $N_1 \times N_2$ topological systems with open boundary conditions (see Section 4.5 Supplementary Material) shows that the

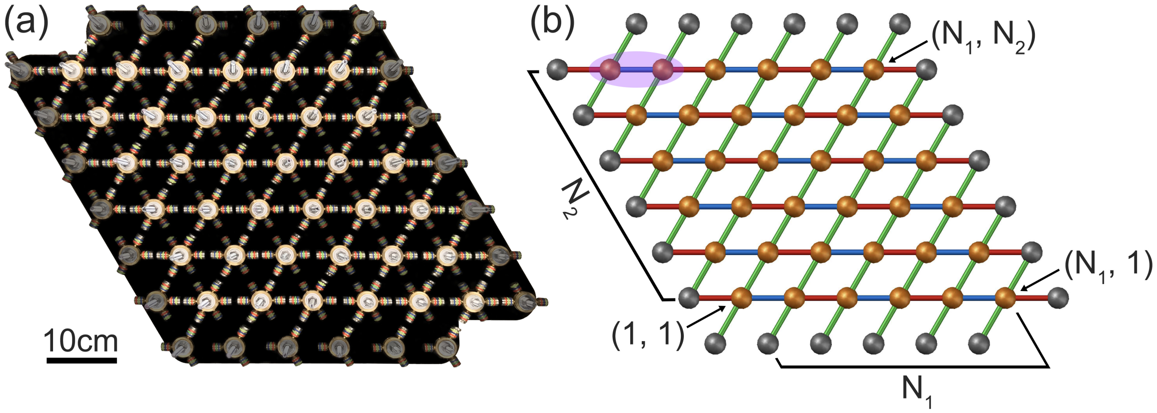

Figure 4.1 (a) 6×6 spinner system, where rotatable spinners and magnetically coupled arms are highlighted and fixed spinners and arms without magnets are shaded. (b) Illustration of the spinner system pictured in (a), where the orange [grey] balls represent rotatable [fixed] spinners. The purple ellipse represents a unit cell. The blue [red] lines indicate the couplings within [between] the unit cells within the 1D SSH chains along the $0°$direction. The green lines indicate the constant interchain coupling, which is smaller than the average intrachain coupling. Coordinates (n_1, n_2) describe the position of the spinners. Source: [Qian et al., 2020].

edge states decay rapidly within a few spinner-to-spinner distances in the n_1 direction and the edge band widths for the systems with $N_2 = 6$ are within $5 - 15\%$ $(0.12 - 0.03$ Hz) from those for the large N_2 limit. Thus, small size systems from 4×6 to 12×6 are sufficient to reveal the trend in the edge band width versus N_1, the distance between the topological edges.

4.2.2 Results for Topological Insulator Systems

Figure 4.2 shows the results for the topological systems. Spectra obtained with the $(N_1-1, 1)$ spinner for the $N_1 \times 6$ systems with N_1 = 4, 6, 8, 10, and 12 are shown in solid lines in Figures 4.2(a)-4.2(e), respectively, each of which reveals upper and lower bulk bands, marked by blue areas, and a gap in between. To reveal the modes at the top [bottom] of the upper [lower] bulk bands better, we also actuate and measure at $(N_1/2 + 1, 5)$ spinners, as shown in dotted lines in Figures 4.2(a)-4.2(e). Figures 4.2(f)-4.2(j) show spectra obtained with the $(N_1, 2)$ spinner for the same systems as in Figures 4.2(a)-4.2(e), respectively. Edge bands, marked by red areas, appear within the gaps of the bulk spectra. Figures 4.2(a)-4.2(j) show systematic changes in the bulk and edge band widths, which are plotted as solid symbols in Figure 4.2(k), along with the theoretical results shown as open symbols. The experimental results are in agreement with the theory and show both upper and lower bulk band widths increase as the edge-to-edge distance N_1 increases due to the finite size effect, and start to saturate around $N_1 \sim 8$. In contrast, the edge band width from the experiments narrows rapidly as the edge-to-edge distance increases, consistent with the numerical results. Theoretical analysis for systems with a periodic boundary condition in the n_2 direction reveals that the edge states with the wave vector k_2 have bipartite patterns of zero amplitudes and exponentially decaying nonzero amplitudes with localization length $\xi(k_2)$.[1] This leads to the edge band width $\Delta f_0 = CN_1 e^{-N_1/\xi_0}$ in the large N_1/ξ_0 limit, where C is a constant and $\xi_0 = \xi\ (k_2 = 0)$ (see Section 4.5 Supplementary Material for details.). Since N_1/ξ_0 is not large for $N_1 = 4$ and the theoretical $\xi_0^{\text{theory}} = 3.1$, the experimental data for $N_1 =$ 6, 8, 10, and 12 are used to decide ξ_0 experimentally as shown in Figure 4.2(l). The line represents $\ln(\Delta f_0) = \ln C + \ln N_1 - N_1/\xi_0$ and shows agreement with experimental data with $\xi_0 \approx 3.2$, close to ξ_0^{theory}. The results in Figures 4.2(k) and 4.2(l) indicate that the edge band would be completely flat, as the edge-to-edge distance N_1 increases further, confirming the predictions [Zhu et al., 2019].

4.2.3 Topological and Nontopological Systems

By exchanging the strong and the weak intrachain couplings, the topological systems become nontopological. The experimental results for 6×6 topological and nontopological systems are shown in Figures 4.3(a) and 4.3(b). For the topological system, the edge band is prominent in the spectra obtained from the $(6, 2)$ and $(6, 1)$ spinners, located within the gap in the spectrum from the $(5, 1)$ spinner. For the nontopological system, the edge band

---

[1] The theoretical analysis leads to the localization length of the edge states with a wave vector k_2, $\xi(k_2) = 4/\ln[(\beta_r^2 + \beta_g^2 + 2\beta_r\beta_g \cos k_2)/(\beta_b^2 + \beta_g^2 + 2\beta_b\beta_g \cos k_2)]$. Here, β_r, β_b, and β_g are the parameter β defined in the paper [Apigo et al., 2018] for the pairs connected by red, blue and green lines in Figure 4.1(b) with values of 280.0 Hz^2, 106.7 Hz^2, and 83.4 Hz^2, respectively, resulting in $\xi(k_2)$ from 0.9 at $k_2 = \pm\pi$ to 3.1 at $k_2 = 0$.

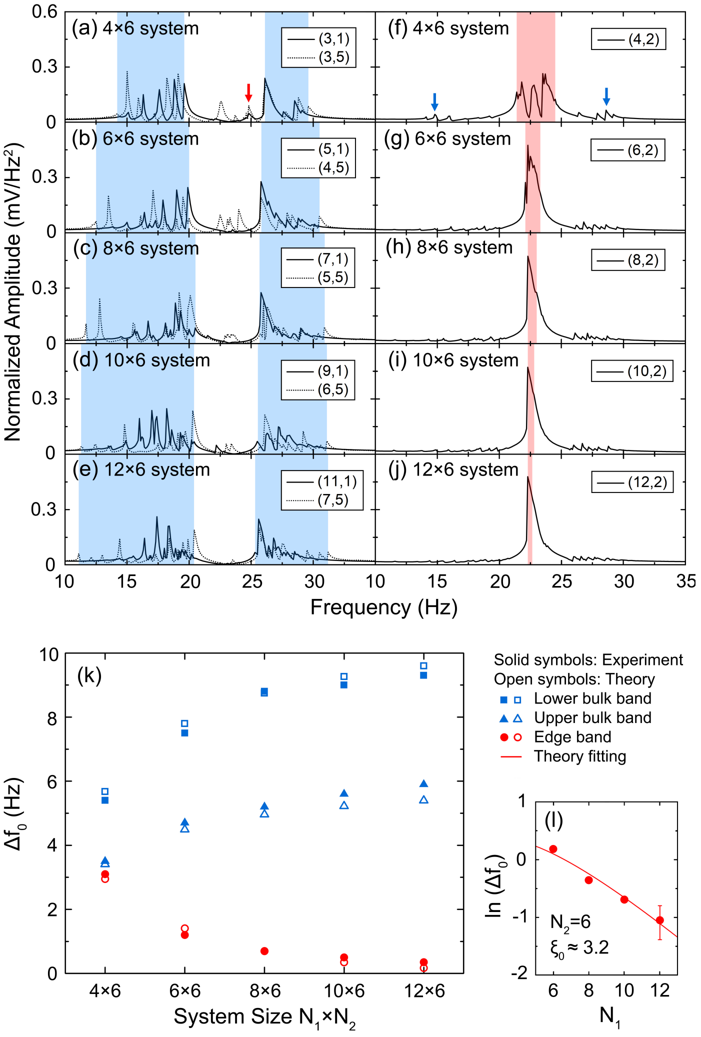

Figure 4.2 Results for topological systems. (a-e) Solid lines: Bulk mode spectra experimentally obtained by actuating and measuring at the $(N_1 - 1, 1)$ spinner for the $N_1 \times 6$ systems with $N_1 = 4$, 6, 8, 10, and 12, respectively. Dotted lines: Spectra obtained with the $(N_1/2 + 1, 5)$ spinner to reveal the top [bottom] of the upper [lower] bulk bands better. The blue areas indicate the lower and upper bulk bands. (f-j) Edge mode spectra experimentally obtained with the $(N_1, 2)$ spinner for the same systems as in (a-e), respectively. Red areas indicate the edge bands. A red arrow in (a) [blue arrows in (f)] indicates edge [bulk] modes appearing in the bulk [edge] spectra due to the short edge-to-edge distance. (k) Experimental and theoretical bulk and edge band widths versus the system size $N_1 \times N_2$. (l) Logarithm of experimental edge band width, $\ln(\Delta f_0)$, versus N_1 and fitting to the theory, resulting in the localization length at $k_2 = 0$, $\xi_0 \approx 3.2$, close to the theory value of 3.1 (see Section 4.5 Supplementary Material for details). Source: [Qian et al., 2020].

disappears from the gap, leaving only the bulk bands. The results show the difference between the topological and nontopological systems and the topological origin of the edge states [Zhu et al., 2019].

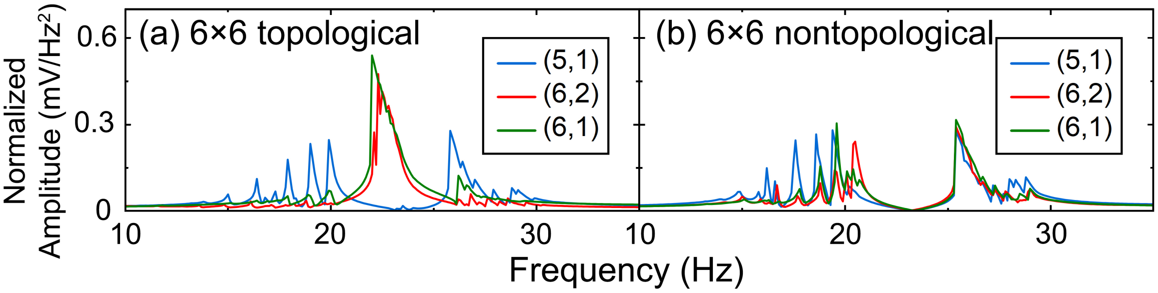

Figure 4.3 Spectra experimentally obtained by actuating and measuring at the $(5, 1)$, $(6, 2)$, and $(6, 1)$ spinners for the 6×6 (a) topological and (b) nontopological systems. The edge band is present in the bulk band gap in (a), but absent in (b). Source: [Qian et al., 2020].

4.2.4 Localization of Edge Modes

For topological systems, the presence of the edge modes depends on the direction of the open edges, determined by the winding numbers $\nu(120°) = 1$ and $\nu(0°) = 0$. With $\nu = 0$ outside the open edges, the edge modes should occur only along the $120°$direction edges, not along the $0°$direction. To test these predictions, we build a topological system with the same number of spinners along the $0°$and $120°$directions, and actuate the $(N_1, 1)$ spinner, which belongs to both $0°$and $120°$direction edges, at a frequency within the edge band to see along which direction the edge mode appears. We choose a small 4×4 system, so that all the spinners at the topological edges show large oscillations and bulk modes could be excited by actuating the same spinner at a bulk mode frequency. The oscillation pattern at an edge mode frequency is displayed in Figure 4.4(a), in which the colors approximately represent the oscillation amplitudes of spinners, estimated from the slow motion movie by eyes. The actuated spinners are marked by stars in Figure 4.4. The edge mode appears along the edges in the $120°$direction, not in the $0°$direction, consistent with the topological analysis. It confirms that the bands in the bulk band gap in Figures 4.2(f)-4.2(j), and 4.3(a) are edge bands. We excite bulk modes by actuating the $(4, 1)$ spinner at a bulk band frequency, as shown in Figure 4.4(b), where the oscillations are concentrated on the central two columns along the 120°direction, confirming the bands above and below the gap in Figures 4.2(a)-4.2(e) and 4.3(a) are the bulk bands. As the edge-to-edge distance N_1 increases and the edge band becomes flatter, the excitation at the edges is more localized along the edges. To verify this, the $N_1 \times 4$ systems with $N_1 = 6$ and 8 are studied by actuating $(N_1, 1)$ spinner at edge mode frequencies. The results shown in Figures 4.4(c) and 4.4(d) reveal that edge modes decay much faster along the edges compared to the 4×4 system in Figure 4.4(a), consistent with the enhanced localization as the edge band becomes narrower. For the 8×4 system shown in Figure 4.4(d), only $(1, 4)$ spinner, other than the actuated $(8, 1)$ spinner, shows a large oscillation, while the oscillations of all other spinners are much smaller, which is the analog of the fractional charge state [Asbóth et al., 2016].

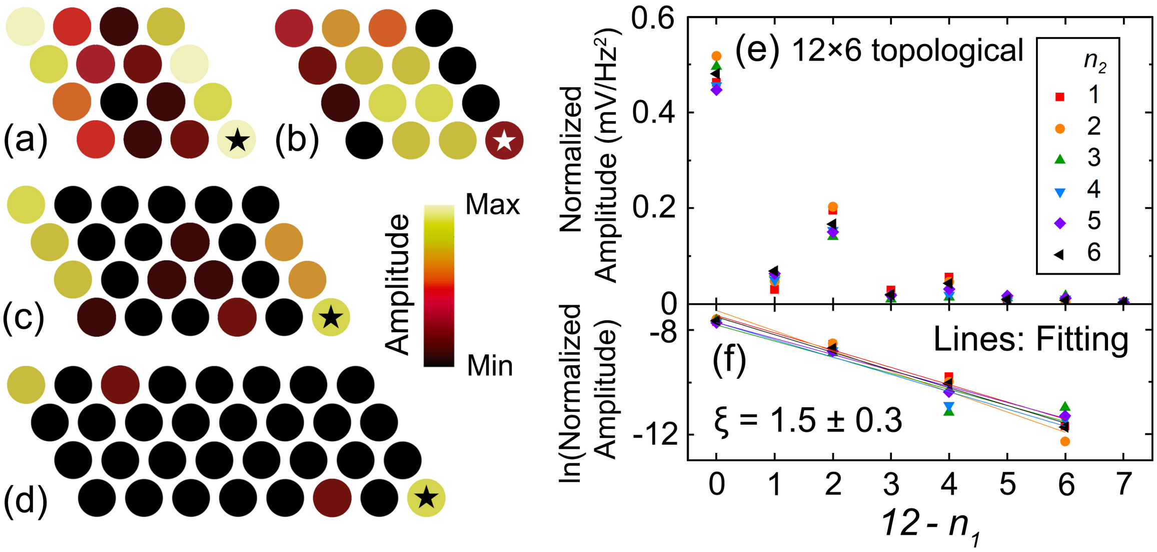

Figure 4.4 (a-d): Patterns of modes. Colors represent the oscillation amplitudes of the spinners, estimated from slow motion movies by eyes. Stars mark actuated spinners. In (a) [(b)], an edge [bulk] mode is revealed at 23.6 Hz [19.5 Hz] in the edge [bulk] band for the 4×4 topological system. In (c) [(d)], an edge mode is revealed at 23.7 Hz [24.5 Hz] for the 6×4 [8×4] topological system. (e) Normalized oscillation amplitude of the (n_1, n_2) spinner versus its distance from the right edge, $12 - n_1$, when a single $(12, n_2)$ spinner ($n_2 = 1, ..., 6$) at the right edge is actuated for the 12×6 topological system. (f) Symbols: semilogarithmic plot of (e) for even $12 - n_1$. Lines: linear fittings, leading to an average localization length $\xi = 1.5 \pm 0.3$, consistent with the theoretical range of $\xi(k)$, $0.9 \sim 3.1$. Source: [Qian et al., 2020].

As mentioned briefly, theoretical analysis leads to the amplitude of the right edge mode with the wave vector k_2 vanishes for odd n_1, and decays as $B_{k_2}(n_1, n_2) = Be^{-(N_1-n_1)/\xi(k_2)}$ for even n_1, where $\xi(k_2)$ is the localization length (see Section 4.5 Supplementary Material for details.) To verify this for the 12×6 system, we actuate a single $(12, n_2)$ spinner ($n_2 = 1, ..., 6$) at the central frequency of the edge band and measure the amplitudes for the (n_1, n_2) spinners with 12-n_1 = 0, ..., 7 by accelerometers. The results for each case of n_2 are shown in Figure 4.4(e), which reveals that the right edge modes have much smaller amplitude for odd n_1 than for even n_1, consistent with the theory. Semilogarithmic plot for the data with even n_1 in Figure 4.4(f) shows exponentially decaying amplitudes, with the average localization length $\xi = 1.5 \pm 0.3$, which is within the range of the theoretical $\xi(k_2)$ from 0.9 at $k_2 = \pm\pi$ to 3.1 at $k_2 = 0$, reflecting that the excited edge states are combinations of edge states with different k_2.

4.3 Flat Frequency Bands at Antiphase Boundaries

4.3.1 Ring-shaped System

Inhomogeneous systems could host flat bands at the antiphase or twin boundaries inside the bulk [Zhu et al., 2019, Ahn et al., 2005]. The antiphase boundary of the 1D SSH chain hosts the zero energy state in the gap, because it separates domains with different winding numbers [Li et al., 2018, Asbóth et al., 2016]. To force the system to have an antiphase boundary but no edges, a ring-shaped 1D SSH system with an odd number (15) of spinners is built, as shown in Figure 4.5(a), where the red and the blue lines represent the interactions between magnets separated by 5.0 and 8.0 mm, respectively. A fixed spinner, shown as a grey ball, is placed just outside the seam for the chiral symmetry. By actuating and measuring at the spinner $\#1$ [$\#2$], the antiphase boundary seam mode [bulk mode] is revealed in the spectrum, as shown in the red [blue] line in Figure 4.5(b). The seam mode peak is present in the gap, consistent with the theory [Zhu et al., 2019, Asbóth et al., 2016]. The slow motion movie of the seam mode reveals an oscillation of every other spinners in both directions from the spinner $\#1$ with decaying amplitudes, consistent with the theory [Schomerus, 2013, Asbóth et al., 2016] and experiments for other 1D SSH metamaterials [Li et al., 2018, Ota et al., 2018].

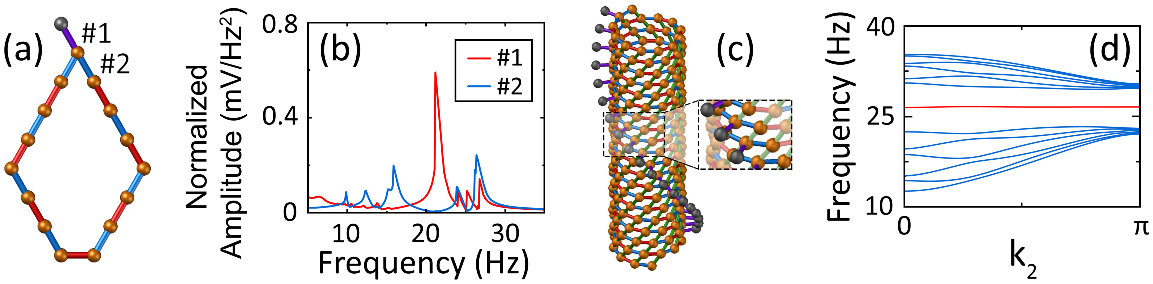

Figure 4.5 (a) Illustration of the SSH ring with fifteen spinners and a seam experimentally studied. See the caption for Figure 4.1(b). The purple line represents the extra coupling at a magnet distance of 6.5 mm for the chiral symmetry. (b) Red [Blue] line: Edge [Bulk] mode spectrum experimentally obtained by actuating and measuring at the spinner $\#1$ [$\#2$] for the SSH ring shown in (a). (c) Tubular model system with thirteen spinners in the azimuthal direction and an antiphase boundary seam, obtained by joining the $(1, n_2)$ and $(13, n_2 + 1)$ spinners of a planar system like Figure 4.1(b) with $N_1 = 13$. The grey balls represent fixed spinners interacting with the spinners at the seam. The magnification shows the antiphase boundary seam with the weak azimuthal couplings on both sides (the blue lines), and the couplings with the fixed spinners (the purple lines). (d) Band structure for the tubular system in (c). The blue lines represent the bulk bands and the red line the flat antiphase boundary seam band. Source: [Qian et al., 2020].

4.3.2 Theoretical Tubular Model

We theoretically consider tubular SSH systems with odd numbers of the spinners in the azimuthal direction, so that the antiphase boundary seams are forced to be present as shown in Figure 4.5(c). While this seam is *locally* equivalent to the $120°$antiphase boundary [Zhu et al., 2019], the odd number of spinners in the azimuthal direction prevents us from defining a two-spinner unit cell or the topological winding number *globally*, unlike the systems proposed in [Zhu et al., 2019]. With a periodic boundary condition along the tube axis, the frequency versus k_2 is calculated and shown in Figure 4.5(d), revealing an almost flat seam band (red line) inside the gap between the bulk bands (blue lines). The flat band found in this system, where the winding number is undefinable, demonstrates the robustness of the flat bands.

4.4 Summary

This study experimentally demonstrates the presence of the flat frequency bands of the topological origin localized at open edges and antiphase boundary seams in discrete mechanical metamaterials made of magnetically coupled spinners. The results presented herein could apply to metamaterials in different fields of interest, potentially leading to novel phenomena and device applications.

4.5 Supplementary Material

4.5.1 Theoretical Analysis

In this subsection, further details of the theoretical analysis are provided. As described in previous chapters [Apigo et al., 2018, Qian et al., 2018], the normalized Lagrangian for two magnetically coupled spinners is approximately given by

$$\frac{L(\varphi_1,\varphi_2,\dot{\varphi}_1,\dot{\varphi}_2)}{2\pi^2 I} = \frac{1}{4\pi^2}\dot{\varphi}_1^2 + \frac{1}{4\pi^2}\dot{\varphi}_2^2 - \frac{1}{2}\alpha(\varphi_1^2 + \varphi_2^2) - \beta\varphi_1\varphi_2, \tag{4.1}$$

where I represents the moment of inertia of each spinner, φ_1 and φ_2 the rotation angles of the two spinners from the equilibrium states. The parameters α and β represent the coefficients in potential energy terms and depend on the strengths of the magnets attached at the end of spinner arms and the distance between the magnets. If we represent the parameter β for the spinner pairs connected by the blue, red, and green lines in Figure 4.1(b) in the main text as β_b, β_r, and β_g, the condition for the gap opening is $\beta_g < (\beta_b + \beta_r)/2$, under which the system becomes topological if $\beta_b < \beta_r$ and nontopological if $\beta_b > \beta_r$. For the topological insulator spinner systems, the parameter values are $\beta_b = 106.7$ Hz^2, $\beta_r = 280.0$ Hz^2, and $\beta_g = 83.4$ Hz^2.

Applying periodic boundary conditions in the n_2 direction, the localization length $\xi(k_2)$ for the edge states with the wave vector k_2 is found to be

$$\xi(k_2) = \frac{4}{\ln \frac{\beta_r^2+\beta_g^2+2\beta_r\beta_g\cos k_2}{\beta_b^2+\beta_g^2+2\beta_b\beta_g\cos k_2}}, \tag{4.2}$$

similar to the localization length for the 1D SSH system [Asbóth et al., 2016]. The amplitude of the oscillation for the left-edge state with the wave vector k_2 decays as

$$A_{k_2}(n_1, n_2) = \begin{cases} Ae^{-(n_1-1)/\xi(k_2)} & \text{for odd } n_1 \\ 0 & \text{for even } n_1 \end{cases} \tag{4.3}$$

and for the right-edge state as

$$B_{k_2}(n_1, n_2) = \begin{cases} 0 & \text{for odd } n_1 \\ Be^{-(N_1-n_1)/\xi(k_2)} & \text{for even } n_1 \end{cases} \tag{4.4}$$

in the limit of the large edge-to-edge distance, N_1. With the parameter values given above for the topological spinner systems, we obtain the localization length $\xi(k_2)$ versus k_2 as shown in Figure 4.6, with $\xi(k_2)$ ranging between 0.9 at $k_2 = \pm\pi$ and 3.1 at $k_2 = 0$ in the unit of the spinner-to-spinner distance. The above theoretical results are used to analyze the experimental results shown in Figures 4.4(e) and 4.4(f) in the main text.

The frequency splitting $\Delta f(k_2)$ between the two edge modes with the wave vector k_2 is $\Delta f(k_2) = CN_1e^{-N_1/\xi(k_2)}$ in the limit of large $N_1/\xi(k_2)$. Since the localization length $\xi(k_2)$ is largest at $k_2 = 0$, the edge band width Δf_0 is given by

$$\Delta f_0 = CN_1e^{-N_1/\xi_0} \tag{4.5}$$

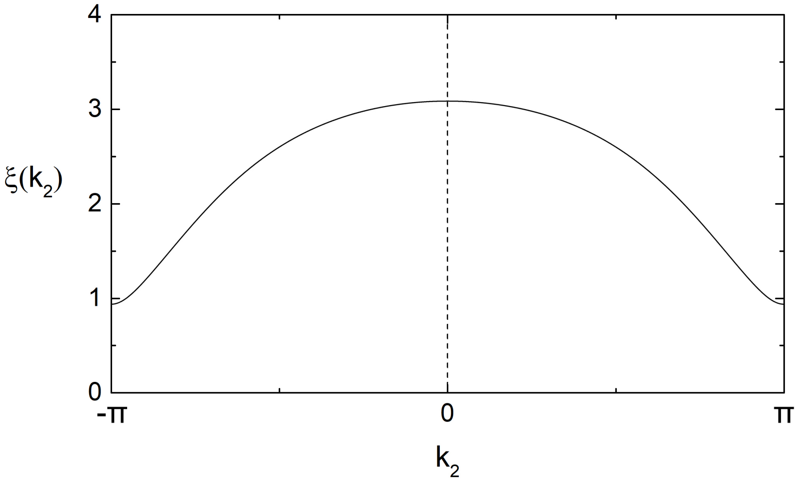

Figure 4.6 Localization length $\xi(k_2)$ versus the edge state wave vector k_2 in the limit of the large edge-to-edge distance N_1 for the topological spinner systems. $\xi(k_2)$ varies between 0.9 at $k_2 = \pm\pi$ and 3.1 at $k_2 = 0$. Source: [Qian et al., 2020].

in the limit of large N_1/ξ_0, where $\xi_0 = \xi(k_2 = 0)$, the localization length at $k_2 = 0$. The plot of $\ln(\Delta f_0)$ versus N_1 for experimental data is fitted into $\ln(\Delta f_0) = \ln C + \ln N_1 - N_1/\xi_0$ to estimate ξ_0, as shown in Figure 4.2(l).

4.5.2 Adequacy of the Chosen Spinner System Sizes

In this subsection, the sizes experimentally chosen for the spinner systems are shown to be adequate to demonstrate the flatness of the edge bands. Since Figure 4.2(k) demonstrates that experimental results agree well with numerical simulations for the edge band width, numerical simulations with open boundary conditions are used for the analysis.

First, for the $N_1 \times N_2$ spinner system, we fix N_1 to 4, 6, 8, 10, and 12, the values chosen for the experiments, and varies N_2 up to $1,000$ to see how the edge band width Δf_0 depends on N_2. The results in Figure 4.7(a) show that the edge band width Δf_0 increases as N_2 increases. The values of Δf_0 at $N_2 = 1,000$, which could be considered as the large N_2 limit, are shown as horizontal lines. The results show that the edge band widths Δf_0 at $N_2 = 6$ (vertical dashed line), the size chosen for experimental setups for the results in Figure 4.2, are only about $0.12 \sim 0.03$ Hz, or $5 \sim 15\%$ smaller than the corresponding large N_2 limits for the systems with $N_1 = 4, 6, 8, 10$, and 12, which indicates that the choice

$N_2 = 6$ is adequate. Relatively quick saturation of Δf_0 for N_2 as small as 6 in Figure 4.7(a) is consistent with the edge band width being determined at $k_2 = 0$ [See Equation (4.5)], which is insensitive to the number of k_2-points.

Next, with N_2 fixed at 6, we examine how adequate the experimental choice of $N_1 = 4$, 6, 8, 10, 12 is to represent the trend in the edge band width Δf_0 versus N_1. The results in Figure 4.7(b) show that the edge band width Δf_0 continues to decrease as the edge-to-edge distance N_1 increases further up to 30, and becomes below the experimental resolution, shown in gray area, beyond around $N_1 = 12$. Rapid decrease of the edge band width with the increase in N_1 from $N_1 = 4$ to 12 reflects the relatively short localization length, $\xi(k_2) = 0.9 \sim 3.1$ in the unit of spinner-to-spinner distance for the chosen experimental parameters. The experimental results for $N_1 = 6$, 8, 10, and 12 also allow us to reveal exponential decrease of the edge band width Δf_0 with respect to N_1, consistent with the theoretical predictions, as shown in Figure 4.2(l). Therefore, our choice of $N_1 = 4$, 6, 8, 10, 12 and $N_2 = 6$ for experimental setups is adequate to show that the edge band would have a vanishing width and become flat in the whole projected reciprocal space in the limit of large edge-to-edge distance.

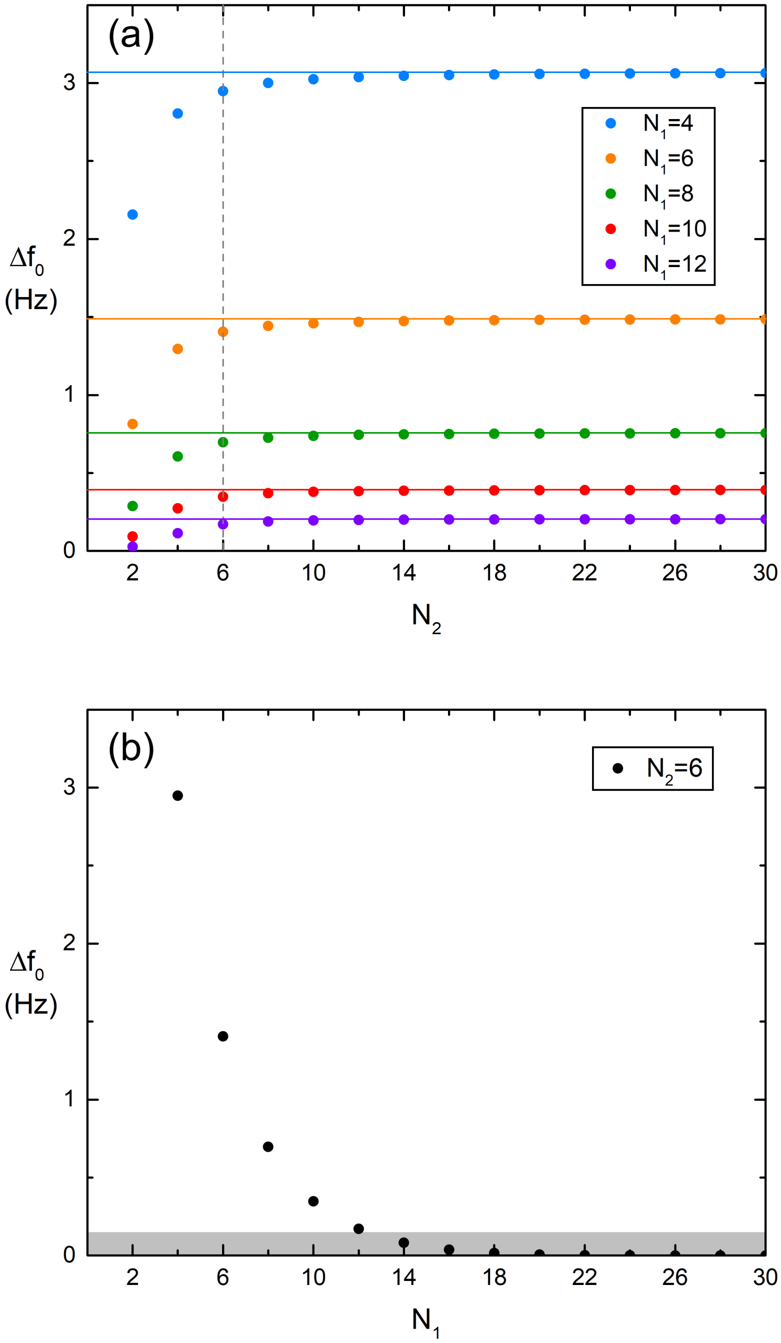

Figure 4.7 (a) Symbols: Edge band width Δf_0 versus N_2, calculated for $N_1 \times N_2$ systems with $N_1 = 4$, 6, 8, 10, and 12 and open boundary conditions. Horizontal solid lines: Δf_0 calculated for $N_2 = 1,000$ as a large N_2 limit for each case of N_1. Vertical dashed line: $N_2 = 6$ chosen for experimental setups. (b) Edge band width Δf_0 versus N_1, calculated for the $N_1 \times 6$ systems with open boundary conditions. The gray area approximately represents the experimental resolution, below which the edge band width cannot be measured reliably. Source: [Qian et al., 2020].

CHAPTER 5

MAJORANA EDGE MODES IN A SU-SCHRIEFFER-HEEGER LADDER

In this chapter, we will experimentally demonstrate Majorana edge modes and topological phase transitions in a mechanical Kitaev chain system based on a previously proposed SSH ladder model. The manuscript of this study is still in preparation. The work is in collaboration with Dr. David J. Apigo and Prof. Camelia Prodan from the Department of Physics at New Jersey Institute of Technology, Drs. Karmela Padavić, Suraj S. Hedge, and Prof. Smitha Vishveshwara from University of Illinois, Urbana-Champaign, and Prof. Emil Prodan from the Department of Physics from Yeshiva University.

5.1 Introduction

Localized Majorana fermions or Majorana bound states, supported by the Kitaev chain (Majorana wire) [Kitaev, 2001], have attracted much interest in the rapidly growing research field of topological superconductors [Hughes, 2011, Hosur et al., 2011, Leijnse and Flensberg, 2012, Teo and Hughes, 2013, DeGottardi et al., 2013, Nadj-Perge et al., 2014, Benalcazar et al., 2014, Sato and Fujimoto, 2016, Kozii et al., 2016, Hu and Kane, 2018, Yan et al., 2019, Li et al., 2020, Wang et al., 2020]. Remarkably, due to the intrinsic immunity to decoherence, they can be used as qubits for quantum computations [Kitaev, 2001, Nayak et al., 2008, Hyart et al., 2013, Kauffman and Lomonaco, 2018, Lian et al., 2018, Tutschku et al., 2020]. Recently, there has been a theoretical study for investigating physical properties for the Kitaev chain and its localized bound edge states in an electronic system described by a quasi-one-dimensional (quasi-1D) ladder model Hamiltonian [Padavić et al., 2018] based on the SSH model [Su et al., 1979]. In the topological phase, this SSH ladder model acts as an analog of the Kitaev chain [Padavić et al., 2018]. The close relationship between the two model systems gives rise to a clear correspondence between their respective topological phases. Here, we emphasize that the bound edge states of the SSH ladder model are not Majorana fermions but number-conserving fermionic states. Previous studies have shown that topological phases of the SSH ladder model host edge modes with wave functions having spatial profiles that match those of the localized Majorana modes of the Kitaev chain [Padavić et al., 2018]. Presently, we discuss its realization, and therefore, a realization of the Majorana wire, in a system of magnetically coupled spinners [Apigo et al., 2018, Qian et al., 2018, Qian et al., 2020]. We focus on zero energy states as they are meant to reflect the spatial wave function structure of the dispersionless edge modes present in the Kitaev chain and the SSH ladder model. Experimentally confirming the presence of these modes amounts to establishing the mechanical resonator system to be in a topologically non-trivial phase that is a counterpart to the topological phases of the Kitaev chain.

5.2 SSH Ladder System

Systems of magnetically coupled spinners have been shown to be a versatile experimental platform for various model Hamiltonians [Apigo et al., 2018, Qian et al., 2018, Qian et al., 2020]. In the mapping between electronic tight-binding Hamiltonians and magnetically coupled spinner systems, the intersite electron hopping corresponds to the interspinner magnetic interaction, which is controlled by the distance between the magnets. The electronic model Hamiltonians studied in [Padavić et al., 2018] are based on a quasi-1D model consisting of two coupled SSH chains - an SSH ladder - which possesses the same edge mode localization properties as the Majorana wire. By calculation, the SSH ladder can be realized with magnetically coupled spinners. By simply varying the interchain coupling distance, the spinner ladder system can be transformed between a topological insulator and a topologically trivial insulator. Slow motion movies are analyzed for the pattern of modes.

5.2.1 Configuration

The setup of the SSH spinner ladder system and its schematic diagram are shown in Figures 5.1(a) and 5.1(b). The system is composed of two horizontal SSH chains with alternating intrachain couplings, shifted and stacked along the $60°$direction with a constant interchain coupling distance. As shown in Figure 5.1(a), with magnets attached to the $0°$, $60°$(for lower chain), $180°$, and $240°$(for upper chain) direction arms and the spinners arranged in the quasi-triangular lattice, the system is equivalent to the quasi-1D electronic model of square lattice with electron hopping in the $0°$, $90°$(for lower chain), $180°$, and $270°$(for upper chain) directions shown in the paper [Padavić et al., 2018]. The spinners are indexed as (n_1, n_2) with $n_1 = 1$ (upper chain), 2 (lower chain) and $n_2 = 1, 2, ..., 13$. As shown in Figure 5.1(b), d_i for $i = 1, 2$ and $i = 12$ denote the couplings between individual spinners along the 0°and 60°directions, respectively. A purple plaquette represents a unit cell. The chiral symmetry is preserved by providing fixed spinners with the necessary interactions placed at the edges. For experimentation, one of the spinners is driven to oscillate by an actuator through the interaction between a magnet on the $60°$direction arm of the spinner and a magnet on the actuator arm. The voltage from an attached accelerometer divided by the square of the frequency is used as a quantity proportional to the oscillation amplitude of the spinner.

5.3 Experimental Results

5.3.1 Bulk and Edge Spectra

Figure 5.2 shows the results for the spinner ladder system with various interchain coupling distances d_{12}. Spectra obtained by actuating and measuring at the $(1, 6)$ and $(1, 7)$ spinners are shown as black solid dots in Figure 5.2(a), which reveals bulk bands, marked by grey areas. When d_{12} is small and close to zero, a gap emerges in the bulk spectra. As d_{12} increases, the gap narrows rapidly from its initial wide open state and disappears. As d_{12} increases further, the gap reopens but with a distinct edge mode emerging within it, shown

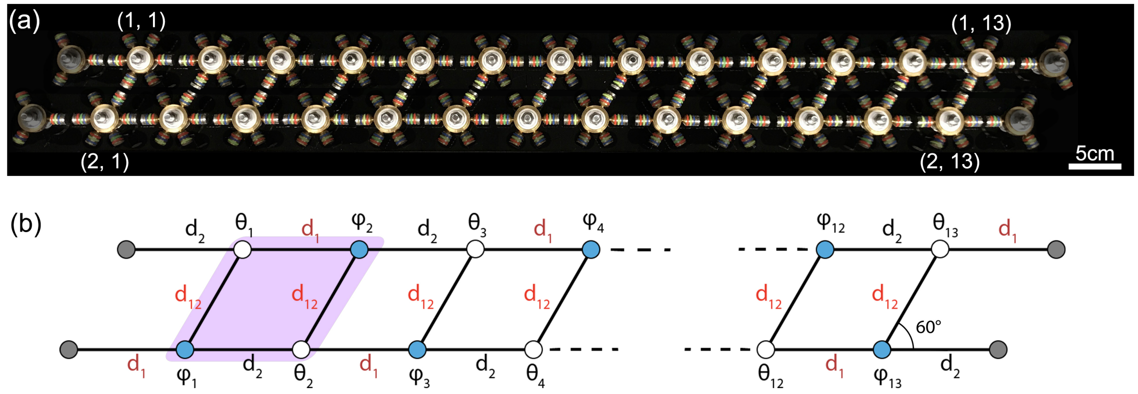

Figure 5.1 (a) Spinner ladder system with the length of 13 rotatable spinners, where rotatable spinners and magnetically coupled arms are highlighted and fixed spinners and arms without magnets are shaded. (b) Illustration of the spinner ladder system pictured in (a), where rotatable spinners are colored white and blue and fixed spinners at both ends are colored grey. A purple plaquette represents a unit cell. d_i for $i = 1, 2$ and $i = 12$ denote the intrachain and interchain coupling distances between spinners in the $0^\circ$and 60°directions, respectively.

as red solid dots in Figure 5.2. We can conclude that the spinner ladder system changes phases from without edge modes to containing edge modes, i.e. the finite-size equivalent of a topologically trivial phase to a topological phase. The width of the spectra range also decreases exponentially as d_{12} increases shown in Figure 5.2. Both are in consistent with the theoretical computations shown in Figure 5.2(b). The results indicate that the topological phase of the spinner ladder system can be controlled by varying the interchain coupling distance, confirming the predictions in [Padavić et al., 2018].

5.3.2 Edge Modes

While the ladder system can hold topological edge states, the localization of the edge mode only emerges at the strong coupled site within the open edges. To verify it, we choose the ladder system with the interchain coupling distance $d_{12} = 8.0$ mm and actuate at the $(1, 1)$ spinner at a frequency of 26.6 Hz to bring out the edge mode and to observe along which chain the edge mode appears. Figure 5.3(a) shows the spectra obtained by measuring at all the rotatable spinners in the system and confirms the resonance mode within the topological gap in Figure 5.2 is indeed the edge mode. Oscillation patterns of different states are

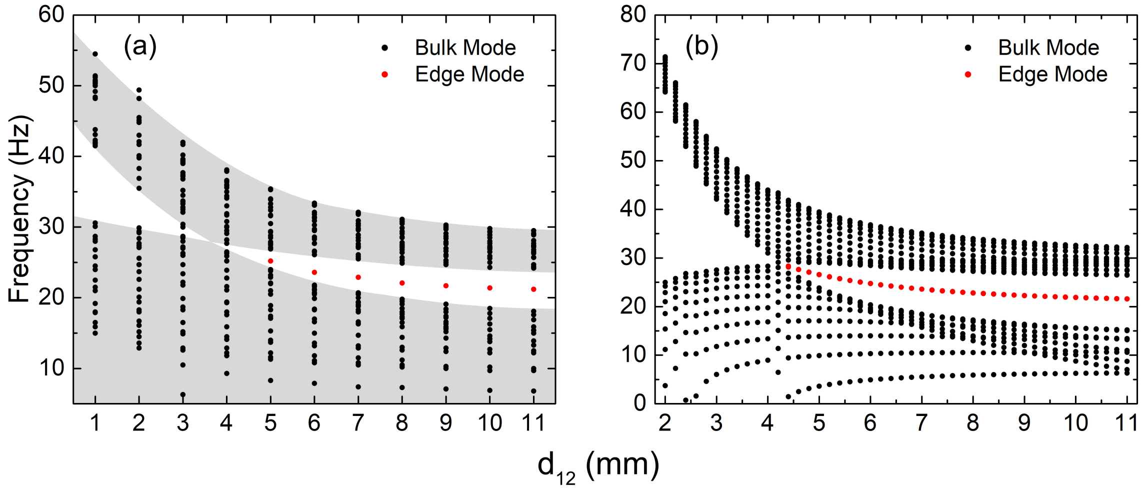

Figure 5.2 (a) Experimental and (b) theoretical resonance modes versus the interchain coupling distance d_{12}. In (a), the bulk modes are obtained by actuating and measuring at the $(1, 6)$ and $(1, 7)$ spinners and the edge modes at the $(1, 1)$ spinner in the ladder system. The grey areas indicate the bulk bands.

shown in Figure 5.3(b-e), where colors represent the normalized oscillation amplitudes. Figure 5.3(c) reveals an oscillation confined at the strong coupled site within left open edge, i.e. the $(1, 1)$ spinner. The oscillation decays in amplitude every other spinners within the upper SSH chain along the $0°$direction, consistent with the theory [Padavić et al., 2018].

5.3.3 Phase Transition

As mentioned previously, the ladder system can be switched between a topologically trivial insulator and a topological insulator by varying the interchain coupling distance d_{12}. Experimental results for topologically trivial ($d = 1.0$ mm) and topological ($d = 7.0$ mm) spinner ladder systems are shown in Figures 5.4(a) and 5.4(c), respectively. In Figure 5.4(c), when the spinner ladder system becomes a topological insulator, the edge mode is prominent located within the gap in the bulk spectra. In contrast, Figure 5.4(a), when the spinner ladder system becomes topologically trivial, the edge mode is absent from the gap, leaving only the lower and upper bulk bands. Figure 5.4(b) shows the results measured from the ladder system with $d_{12} = 4.0$ mm and demonstrate the transition between topologically trivial and topological phases, where no gap and edge mode emerges. In Figures 5.4(a)-(c), in spite of

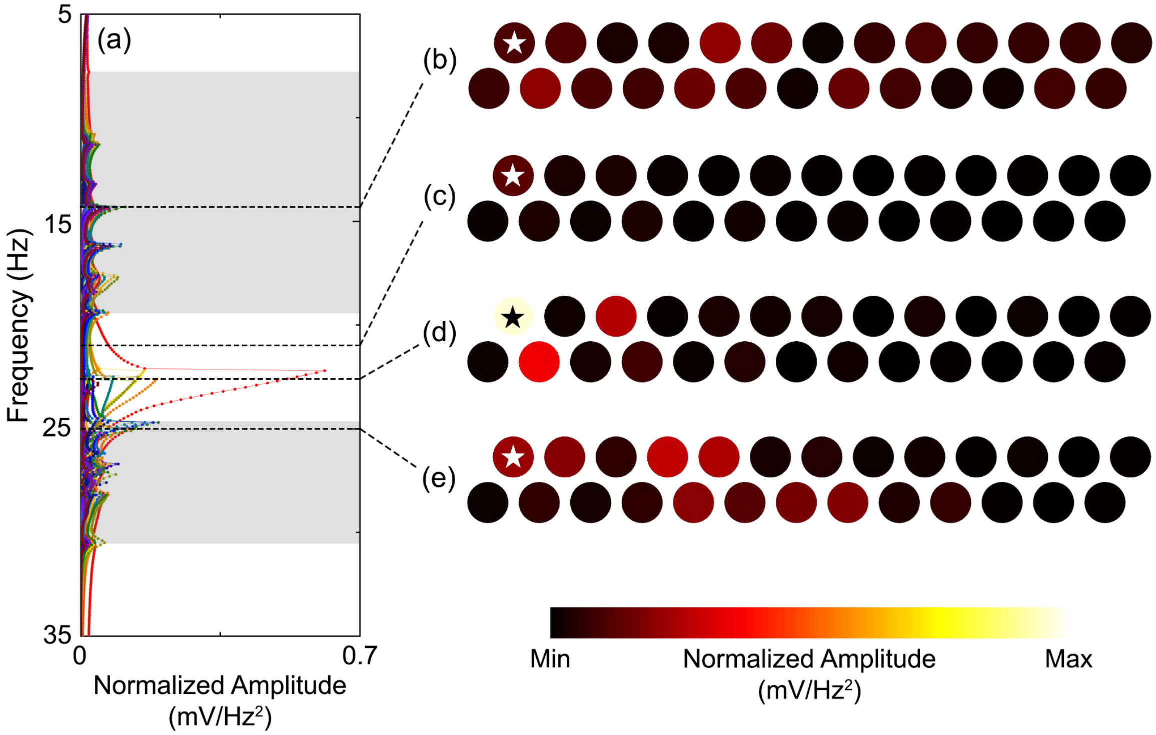

Figure 5.3 (a) Experimental spectra obtained by actuating at the $(1, 1)$ spinner and measuring at all the rotatable spinners in the ladder system with the interchain coupling distance $d_{12} = 8.0$ mm. Grey areas represent the lower and upper bulk bands. One spectral gap, which contains a strong edge mode at the frequency of 22.6 Hz, can be clearly identified. (b)-(e) Patterns of oscillations measured at the frequencies of (b) 14.3 Hz, (c) 21.0 Hz, (d) 22.6 Hz, and (e) 25.0 Hz, respectively. Colors represent the oscillation amplitudes of the rotatable spinners. Stars mark actuated spinners.

different amplitude scales, the data are obtained at the same experimental setup condition. The results show the difference between topologically trivial and topological systems and the topological origin of the spinner ladder system.

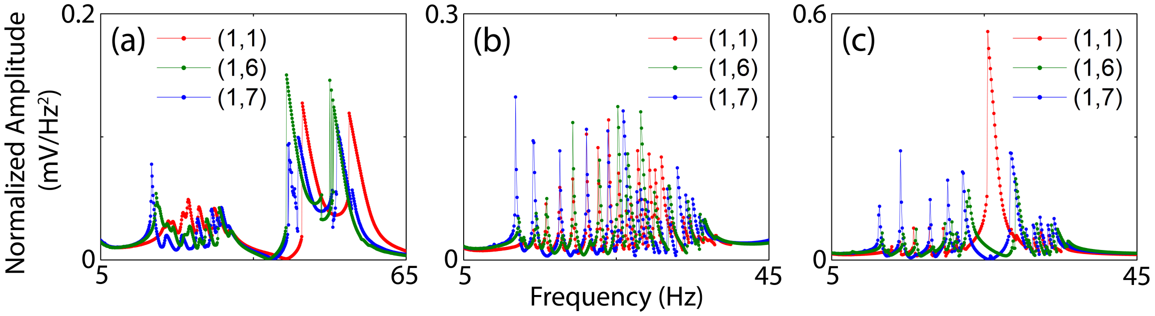

Figure 5.4 Spectra experimentally obtained by actuating and measuring at the $(1,1)$, $(1,6)$, and $(1,7)$ spinners of the ladder systems with interchain coupling distances (a) $d_{12} = 1.0$ mm, (b) $d_{12} = 4.0$ mm and (c) $d_{12} = 7.0$ mm, respectively. The edge band is prominent in the bulk band gap in (c), but absent in (a) and (b). The bulk band gap is absent in (b).

5.4 Summary

This study experimentally demonstrated classical Majorana edge modes at the boundary of a ladder-shaped mechanical metamaterial. The topological phase of the system can be controlled by adjusting the interchain interaction, consistent with previous theoretical analysis [Padavić et al., 2018].

CHAPTER 6

CONCLUSIONS

To recap briefly, we clearly demonstrate that mechanical metamaterials made of magnetically coupled spinners can be novel and versatile experimental platforms for investigation of topological phonons and their phase transitions. Localized excitation modes along the boundaries or interfaces within the bulk spectral gaps are their characteristics. These topological properties originate from the structures solely. Our results can apply to any coupled resonator systems regardless of their nature. In addition, our approach can also offer one a chance to observe topological excitation modes by naked eyes, helping with the exemplification of theoretical concepts that may appear quite abstract.

Recently, the principle of our 1D quasi-periodic pattern has been theoretically expanded to quasi-periodic continuous elastic beams [Pal et al., 2019] and 2D quasi-crystalline structures [Zhou et al., 2019]. Experimental studies also demonstrate the feasibility of generating topological edge or interface modes out of patterning in different systems, such as in quasi-periodic acoustic crystals [Apigo et al., 2019, Ni et al., 2019] and radio-frequency resonator arrays [Voss and Ballon, 2020]. For QVHE regime, Chaunsali *et al.* report that the preference of the topological wave propagation around sharp bends depends on the excitation frequency [Chaunsali et al., 2018a], which deserves a close look. Our proposal for second couplings inspires the numerical simulation of geometrically designed interfacial wave networks that contain splitters, which partition energy along more than two directions, ideal for applications such as beam-splitters, switches, and filters [Makwana and Craster, 2018]. Furthermore, QVHE has been theoretically emulated in a new kagome-like photonic topological insulator where highly efficient photonic edge mode propagates unidirectionally depending on its termination [Wong et al., 2020, Saba et al., 2020]. Similar structure has also been proposed using plasmonic lattices [Proctor et al., 2020, Proctor et al., 2021]. These creative studies offer us an opportunity to review QVHE from a new perspective. The experimental results presented in Chapter 4 and 5 have implications for other metamaterials experimentally shown to realize the 1D SSH model. It includes photonic [Han et al., 2019, Chen et al., 2019, Xie et al., 2019, Xie et al., 2018, Ota et al., 2018, Bello et al., 2019], electronic [Belopolski et al., 2017], acoustic [Li et al., 2018], plasmonic [Bleckmann et al., 2017], circuitry [Lee et al., 2018, Liu et al., 2019, Imhof et al., 2018, Serra-Garcia et al., 2019, Jiang et al., 2018a], optical lattice [Meier et al., 2016], and microwave [Zhu et al., 2018b] metamaterials. Especially for flat bands, realization of the chiral 2D SSH Hamiltonian in photonic crystals [Henriques et al., 2020] could lead to photons guided slowly along designed paths for pulse buffering [Leykam and Flach, 2018, Leykam et al., 2018]. In electronic metamaterials, the effects of correlations would be enhanced for flat bands, resulting in strongly correlated phenomena [Mesaros et al., 2010]. Dynamic tunability in optical lattices may be used to switch the system between topological and nontopological phases [Leykam et al., 2018]. Extension to three-dimensional (3D) systems would reveal the effects of polarization [Leykam and Flach, 2018, Leykam et al., 2018].

A few thoughts for improvements of current experimental setups are discussed here. First, the spinners can be customized using metal additive manufacturing techniques for achieving more complex coupled arms, such as the proposed setting in Figure 2.1(b). Second, the concept of programmable mechanical metamaterials inspire us to adjust the coupling by electrically controlled electromagnetic interaction for reversible and real-time control of topological phases and topological transitions rather than rearrange the inter-magnet distances, which often causes the offset coupling problems, such as the systems in Figures 4.1 and 5.1. The strength of inter-spinner couplings, which are sensitive to the inter-magnet distances, can hence be set more accurate and precise for experimental needs as well. A recent and interesting study has shown electromagnets as a promising and effective way of achieving enhanced static and dynamic efficiency [Haghpanah et al., 2016].

A significant hurdle will be reducing the size of these electromagnets while avoiding serious reduction of coupling strength. Nevertheless, our results can lead to studies of programable mechanical metamaterials with controllable topological properties, which might apply in expandable biomedical devices and soft robotics. Except for electromagnets, manipulating the locations of the spinners can be another choice for changing topological phase. However, due to the offset coupling problems mentioned previously, this method may only be suitable for 1D or quasi-1D systems.

To date, we mainly investigate 1D and 2D topological mechanical systems. The realization of 3D topological metamaterials, which are more complex but appealing, still remains challenging. Essentially, ball bearings we use possess only one rotational degree of freedom and spinners are coupled horizontally only through nearest-neighbor interaction. Although we have realized couplings between adjacent planes in layered lattices, as shown in Figure 6.1, it is still difficult for us to fully realize the whole system in a short time. Fortunately, there have been a few recent studies that we can learn and use for reference, such as 3D topological node lines [Xiong et al., 2018] and 3D elastic phononic topological insulators [Huo et al., 2020]. Future challenges would also include the nonlinearities. Our current studies are bound to fixed lattices and small oscillations. The emerging of nonlinear topological phases, such as nonlinear quantum hall effect [Ma et al., 2019b] and topological laser [Zeng et al., 2020], has already become a new focus of research. However, in mechanical systems, the bulk-boundary correspondence involved in the nonlinear process and the inherent connections between the nonlinear output of the system and the global topological invariant are still ambiguous. Vila *et al.* have reported the lack of topological protections due to the presence of nonlinearities using a 1D spinner system inspired by our work [Vila et al., 2019]. The control of localization and the transition to bulk propagation with topological protection along with nonlinear interactions are still difficult to realize for now.

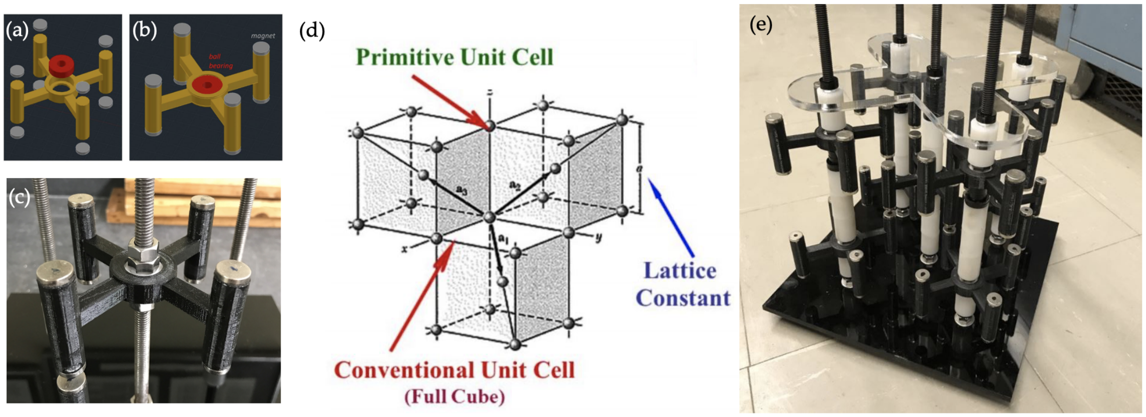

Figure 6.1 Example of the unit cell as our approach for going beyond 2D metamaterials, which is inspired by (d) the body centered cubic lattices. (a-c) The configurations of a single spinner for eight couplings. (e) Prototype of the unit cell for 3D mechanical lattice.

Our results are also applicable in a number of engineering fields, including waveguiding, vibration isolation, sensing, energy harvesting, smart materials, and quantum information. For practical uses, mechanical metamaterials tend to be smaller and lighter. The rapid development of additive manufacturing and nanoelectromechanical systems has provided scientist unprecedented chances to manufacture topological mechanical metamaterials. Indeed, in the real world, the systems, especially continuous systems, are much more complex and certainly have additional degrees of freedom. However, the significance of our work lies in the implementation and observation of topological excitation modes originating solely from the structure of the materials. We hope our efforts would inspire others to design more fascinating topological metamaterials based on the same principles. Although our recent works have been reported, there are still a number of unknown phenomena and mechanisms still waited for being explored.

REFERENCES

[Ahn et al., 2005] Ahn, K., Lookman, T., Saxena, A., and Bishop, A. (2005). Electronic properties of structural twin and antiphase boundaries in materials with strong electron-lattice couplings. *Physical Review B*, 71(21):212102.

[Alù and Engheta, 2007] Alù, A. and Engheta, N. (2007). Plasmonic materials in transparency and cloaking problems: Mechanism, robustness, and physical insights. *Optics Express*, 15(6):3318–3332.

[Alù and Engheta, 2008] Alù, A. and Engheta, N. (2008). Plasmonic and metamaterial cloaking: Physical mechanisms and potentials. *Journal of Optics A: Pure and Applied Optics*, 10(9):093002.

[Apigo et al., 2019] Apigo, D. J., Cheng, W., Dobiszewski, K. F., Prodan, E., and Prodan, C. (2019). Observation of topological edge modes in a quasiperiodic acoustic waveguide. *Physical Review Letters*, 122(9):095501.

[Apigo et al., 2018] Apigo, D. J., Qian, K., Prodan, C., and Prodan, E. (2018). Topological edge modes by smart patterning. *Physical Review Materials*, 2(12):124203.

[Asbóth et al., 2016] Asbóth, J. K., Oroszlány, L., and Pályi, A. (2016). A short course on topological insulators. *Lecture Notes in Physics*, 919:997–1000.

[Bello et al., 2019] Bello, M., Platero, G., Cirac, J. I., and González-Tudela, A. (2019). Unconventional quantum optics in topological waveguide QED. *Science Advances*, 5(7).

[Belopolski et al., 2017] Belopolski, I., Xu, S.-Y., Koirala, N., Liu, C., Bian, G., Strocov, V. N., Chang, G., Neupane, M., Alidoust, N., Sanchez, D., et al. (2017). A novel artificial condensed matter lattice and a new platform for one-dimensional topological phases. *Science Advances*, 3(3):e1501692.

[Benalcazar et al., 2014] Benalcazar, W. A., Teo, J. C., and Hughes, T. L. (2014). Classification of two-dimensional topological crystalline superconductors and Majorana bound states at disclinations. *Physical Review B*, 89(22):224503.

[Berg et al., 2011] Berg, N., Joel, K., Koolyk, M., and Prodan, E. (2011). Topological phonon modes in filamentary structures. *Physical Review E*, 83(2):021913.

[Bernevig et al., 2006] Bernevig, B. A., Hughes, T. L., and Zhang, S.-C. (2006). Quantum spin Hall effect and topological phase transition in $HgTe$ quantum wells. *Science*, 314(5806):1757–1761.

[Bernevig and Zhang, 2006] Bernevig, B. A. and Zhang, S.-C. (2006). Quantum spin Hall effect. *Physical Review Letters*, 96(10):106802.

[Bistritzer and MacDonald, 2011] Bistritzer, R. and MacDonald, A. H. (2011). Moiré bands in twisted double-layer graphene. *Proceedings of the National Academy of Sciences*, 108(30):12233–12237.

[Bleckmann et al., 2017] Bleckmann, F., Cherpakova, Z., Linden, S., and Alberti, A. (2017). Spectral imaging of topological edge states in plasmonic waveguide arrays. *Physical Review B*, 96(4):045417.

[Bleu et al., 2017] Bleu, O., Solnyshkov, D., and Malpuech, G. (2017). Quantum valley Hall effect and perfect valley filter based on photonic analogs of transitional metal dichalcogenides. *Physical Review B*, 95(23):235431.

[Cao et al., 2018a] Cao, Y., Fatemi, V., Demir, A., Fang, S., Tomarken, S. L., Luo, J. Y., Sanchez-Yamagishi, J. D., Watanabe, K., Taniguchi, T., Kaxiras, E., Ashoori, R. C., and Jarillo-Herrero, P. (2018a). Correlated insulator behaviour at half-filling in magic-angle graphene superlattices. *Nature*, 556(7699):80–84.

[Cao et al., 2018b] Cao, Y., Fatemi, V., Fang, S., Watanabe, K., Taniguchi, T., Kaxiras, E., and Jarillo-Herrero, P. (2018b). Unconventional superconductivity in magic-angle graphene superlattices. *Nature*, 556(7699):43–50.

[Chang et al., 2013] Chang, C.-Z., Zhang, J., Feng, X., Shen, J., Zhang, Z., Guo, M., Li, K., Ou, Y., Wei, P., Wang, L.-L., Ji, Z.-Q., Feng, Y., Ji, S., Chen, X., Jia, J., Dai, X., Fang, Z., Zhang, S.-C., He, K., Wang, Y., Lu, L., Ma, X.-C., and Xue, Q.-K. (2013). Experimental observation of the quantum anomalous Hall effect in a magnetic topological insulator. *Science*, 340(6129):167–170.

[Chaunsali et al., 2018a] Chaunsali, R., Chen, C.-W., and Yang, J. (2018a). Experimental demonstration of topological waveguiding in elastic plates with local resonators. *New Journal of Physics*, 20(11):113036.

[Chaunsali et al., 2018b] Chaunsali, R., Chen, C.-W., and Yang, J. (2018b). Subwavelength and directional control of flexural waves in zone-folding induced topological plates. *Physical Review B*, 97(5):054307.

[Chen et al., 2014] Chen, B. G.-g., Upadhyaya, N., and Vitelli, V. (2014). Nonlinear conduction via solitons in a topological mechanical insulator. *Proceedings of the National Academy of Sciences*, 111(36):13004–13009.

[Chen et al., 2018] Chen, H., Nassar, H., and Huang, G. (2018). Topological mechanics of edge waves in kagome lattices. *arXiv 1802.04404*.

[Chen et al., 2019] Chen, X.-D., Deng, W.-M., Shi, F.-L., Zhao, F.-L., Chen, M., and Dong, J.-W. (2019). Direct observation of corner states in second-order topological photonic crystal slabs. *Physical Review Letters*, 122(23):233902.

[Chen et al., 2017] Chen, X.-D., Zhao, F.-L., Chen, M., and Dong, J.-W. (2017). Valley-contrasting physics in all-dielectric photonic crystals: Orbital angular momentum and topological propagation. *Physical Review B*, 96(2):020202.

[DeGottardi et al., 2013] DeGottardi, W., Sen, D., and Vishveshwara, S. (2013). Majorana fermions in superconducting 1D systems having periodic, quasiperiodic, and disordered potentials. *Physical Review Letters*, 110(14):146404.

[Delplace et al., 2011] Delplace, P., Ullmo, D., and Montambaux, G. (2011). Zak phase and the existence of edge states in graphene. *Physical Review B*, 84(19):195452.

[Deymier and Runge, 2016] Deymier, P. and Runge, K. (2016). One-dimensional mass-spring chains supporting elastic waves with non-conventional topology. *Crystals*, 6(4):44.

[Deymier et al., 2015] Deymier, P. A., Runge, K., Swinteck, N., and Muralidharan, K. (2015). Torsional topology and fermion-like behavior of elastic waves in phononic structures. *Comptes Rendus Mécanique*, 343(12):700–711.

[Dong et al., 2017] Dong, J.-W., Chen, X.-D., Zhu, H., Wang, Y., and Zhang, X. (2017). Valley photonic crystals for control of spin and topology. *Nature Materials*, 16(3):298–302.

[Fleury et al., 2014] Fleury, R., Sounas, D. L., Sieck, C. F., Haberman, M. R., and Alù, A. (2014). Sound isolation and giant linear nonreciprocity in a compact acoustic circulator. *Science*, 343(6170):516–519.

[Gao et al., 2018] Gao, F., Xue, H., Yang, Z., Lai, K., Yu, Y., Lin, X., Chong, Y., Shvets, G., and Zhang, B. (2018). Topologically protected refraction of robust kink states in valley photonic crystals. *Nature Physics*, 14(2):140–144.

[Gao et al., 2017] Gao, Z., Yang, Z., Gao, F., Xue, H., Yang, Y., Dong, J., and Zhang, B. (2017). Valley surface-wave photonic crystal and its bulk/edge transport. *Physical Review B*, 96(20):201402.

[Gorbachev et al., 2014] Gorbachev, R. V., Song, J. C. W., Yu, G. L., Kretinin, A. V., Withers, F., Cao, Y., Mishchenko, A., Grigorieva, I. V., Novoselov, K. S., Levitov, L. S., and Geim, A. K. (2014). Detecting topological currents in graphene superlattices. *Science*, 346(6208):448–451.

[Gunawan et al., 2006a] Gunawan, O., Habib, B., De Poortere, E., and Shayegan, M. (2006a). Quantized conductance in an AlAs two-dimensional electron system quantum point contact. *Physical Review B*, 74(15):155436.

[Gunawan et al., 2006b] Gunawan, O., Shkolnikov, Y., Vakili, K., Gokmen, T., De Poortere, E., and Shayegan, M. (2006b). Valley susceptibility of an interacting two-dimensional electron system. *Physical Review Letters*, 97(18):186404.

[Haghpanah et al., 2016] Haghpanah, B., Ebrahimi, H., Mousanezhad, D., Hopkins, J., and Vaziri, A. (2016). Programmable elastic metamaterials. *Advanced Engineering Materials*, 18(4):643–649.

[Haldane, 1988] Haldane, F. D. M. (1988). Model for a quantum Hall effect without Landau levels: Condensed-matter realization of the "parity anomaly". *Physical Review Letters*, 61(18):2015.

[Han et al., 2019] Han, C., Lee, M., Callard, S., Seassal, C., and Jeon, H. (2019). Lasing at topological edge states in a photonic crystal $L3$ nanocavity dimer array. *Light: Science & Applications*, 8(1):1–10.

[Hasan and Kane, 2010] Hasan, M. Z. and Kane, C. L. (2010). Colloquium: Topological insulators. *Reviews of Modern Physics*, 82(4):3045.

[Henriques et al., 2020] Henriques, J., Rappoport, T., Bludov, Y. V., Vasilevskiy, M., and Peres, N. (2020). Topological photonic Tamm states and the Su-Schrieffer-Heeger model. *Physical Review A*, 101(4):043811.

[Hofstadter, 1976] Hofstadter, D. R. (1976). Energy levels and wave functions of Bloch electrons in rational and irrational magnetic fields. *Physical Review B*, 14(6):2239.

[Hosur et al., 2011] Hosur, P., Ghaemi, P., Mong, R. S., and Vishwanath, A. (2011). Majorana modes at the ends of superconductor vortices in doped topological insulators. *Physical Review Letters*, 107(9):097001.

[Hu and Kane, 2018] Hu, Y. and Kane, C. (2018). Fibonacci topological superconductor. *Physical Review Letters*, 120(6):066801.

[Huang et al., 2018] Huang, S., Kim, K., Efimkin, D. K., Lovorn, T., Taniguchi, T., Watanabe, K., MacDonald, A. H., Tutuc, E., and LeRoy, B. J. (2018). Topologically protected helical states in minimally twisted bilayer graphene. *Physical Review Letters*, 121(3):037702.

[Huber, 2016] Huber, S. D. (2016). Topological mechanics. *Nature Physics*, 12(7):621–623.

[Hughes, 2011] Hughes, T. L. (2011). Majorana fermions inch closer to reality. *Physics*, 4:67.

[Huo et al., 2020] Huo, S.-Y., Huang, J.-J., Chen, H.-B., Wei, Y.-J., Feng, Z.-H., Tan, L.-Y., and Xie, X.-P. (2020). Experimental realization of three-dimensional elastic phononic topological insulator. *arXiv:2004.05743*.

[Hyart et al., 2013] Hyart, T., Van Heck, B., Fulga, I., Burrello, M., Akhmerov, A., and Beenakker, C. (2013). Flux-controlled quantum computation with Majorana fermions. *Physical Review B*, 88(3):035121.

[Imhof et al., 2018] Imhof, S., Berger, C., Bayer, F., Brehm, J., Molenkamp, L. W., Kiessling, T., Schindler, F., Lee, C. H., Greiter, M., Neupert, T., and Thomale, R. (2018). Topolectrical-circuit realization of topological corner modes. *Nature Physics*, 14(9):925–929.

[Islam and Benjamin, 2016] Islam, S. F. and Benjamin, C. (2016). A scheme to realize the quantum spin-valley Hall effect in monolayer graphene. *Carbon*, 110:304–312.

[Jiang et al., 2018a] Jiang, J., Guo, Z., Ding, Y., Sun, Y., Li, Y., Jiang, H., and Chen, H. (2018a). Experimental demonstration of the robust edge states in a split-ring-resonator chain. *Optics Express*, 26(10):12891–12902.

[Jiang et al., 2018b] Jiang, J.-W., Wang, B.-S., and Park, H. S. (2018b). Topologically protected interface phonons in two-dimensional nanomaterials: Hexagonal boron nitride and silicon carbide. *Nanoscale*, 10(29):13913–13923.

[Ju et al., 2015] Ju, L., Shi, Z., Nair, N., Lv, Y., Jin, C., Velasco, J., Ojeda-Aristizabal, C., Bechtel, H. A., Martin, M. C., Zettl, A., Analytis, J., and Wang, F. (2015). Topological valley transport at bilayer graphene domain walls. *Nature*, 520(7549):650–655.

[Kane and Lubensky, 2014] Kane, C. and Lubensky, T. (2014). Topological boundary modes in isostatic lattices. *Nature Physics*, 10(1):39–45.

[Kane and Mele, 2005a] Kane, C. L. and Mele, E. J. (2005a). Quantum spin Hall effect in graphene. *Physical Review Letters*, 95(22):226801.

[Kane and Mele, 2005b] Kane, C. L. and Mele, E. J. (2005b). Z_2 topological order and the quantum spin Hall effect. *Physical Review Letters*, 95(14):146802.

[Kang et al., 2018] Kang, Y., Ni, X., Cheng, X., Khanikaev, A. B., and Genack, A. Z. (2018). Pseudo-spin–valley coupled edge states in a photonic topological insulator. *Nature Communications*, 9(1):1–7.

[Kariyado and Hatsugai, 2015] Kariyado, T. and Hatsugai, Y. (2015). Manipulation of Dirac cones in mechanical graphene. *Scientific Reports*, 5(1):1–8.

[Kariyado and Slager, 2019] Kariyado, T. and Slager, R.-J. (2019). π-fluxes, semimetals, and flat bands in artificial materials. *Physical Review Research*, 1(3):032027.

[Kauffman and Lomonaco, 2018] Kauffman, L. H. and Lomonaco, S. J. (2018). Braiding, Majorana fermions, Fibonacci particles and topological quantum computing. *Quantum Information Processing*, 17(8):1–81.

[Khanikaev et al., 2015] Khanikaev, A. B., Fleury, R., Mousavi, S. H., and Alu, A. (2015). Topologically robust sound propagation in an angular-momentum-biased graphene-like resonator lattice. *Nature Communications*, 6(1):1–7.

[Kitaev, 2001] Kitaev, A. Y. (2001). Unpaired Majorana fermions in quantum wires. *Physics-Uspekhi*, 44(10S):131.

[Klembt et al., 2017] Klembt, S., Harder, T. H., Egorov, O. A., Winkler, K., Suchomel, H., Beierlein, J., Emmerling, M., Schneider, C., and Höfling, S. (2017). Polariton condensation in S-and P-flatbands in a two-dimensional Lieb lattice. *Applied Physics Letters*, 111(23):231102.

[Klitzing et al., 1980] Klitzing, K. v., Dorda, G., and Pepper, M. (1980). New method for high-accuracy determination of the fine-structure constant based on quantized Hall resistance. *Physical Review Letters*, 45(6):494.

[König et al., 2007] König, M., Wiedmann, S., Brüne, C., Roth, A., Buhmann, H., Molenkamp, L. W., Qi, X.-L., and Zhang, S.-C. (2007). Quantum spin Hall insulator state in $HgTe$ quantum wells. *Science*, 318(5851):766–770.

[Kozii et al., 2016] Kozii, V., Venderbos, J. W., and Fu, L. (2016). Three-dimensional Majorana fermions in chiral superconductors. *Science Advances*, 2(12):e1601835.

[Lakes, 2017] Lakes, R. S. (2017). Negative-Poisson's-ratio materials: Auxetic solids. *Annual Review of Materials Research*, 47.

[Laughlin, 1983] Laughlin, R. B. (1983). Anomalous quantum Hall effect: An incompressible quantum fluid with fractionally charged excitations. *Physical Review Letters*, 50(18):1395.

[Lazarides and Tsironis, 2019] Lazarides, N. and Tsironis, G. (2019). Compact localized states in engineered flat-band $\mathscr{PT}$ metamaterials. *Scientific Reports*, 9(1):1–9.

[Lee et al., 2018] Lee, C. H., Imhof, S., Berger, C., Bayer, F., Brehm, J., Molenkamp, L. W., Kiessling, T., and Thomale, R. (2018). Topolectrical circuits. *Communications Physics*, 1(1):1–9.

[Leijnse and Flensberg, 2012] Leijnse, M. and Flensberg, K. (2012). Introduction to topological superconductivity and Majorana fermions. *Semiconductor Science and Technology*, 27(12):124003.

[Leykam et al., 2018] Leykam, D., Andreanov, A., and Flach, S. (2018). Artificial flat band systems: From lattice models to experiments. *Advances in Physics: X*, 3(1):1473052.

[Leykam and Flach, 2018] Leykam, D. and Flach, S. (2018). Perspective: Photonic flatbands. *APL Photonics*, 3(7):070901.

[Li et al., 2020] Li, Q., Han, Y., Zhang, K., Zhang, Y.-T., Liu, J.-J., and Qiao, Z. (2020). Multiple Majorana edge modes in magnetic topological insulator–superconductor heterostructures. *Physical Review B*, 102(20):205402.

[Li et al., 2018] Li, X., Meng, Y., Wu, X., Yan, S., Huang, Y., Wang, S., and Wen, W. (2018). Su-Schrieffer-Heeger model inspired acoustic interface states and edge states. *Applied Physics Letters*, 113(20):203501.

[Lian et al., 2018] Lian, B., Sun, X.-Q., Vaezi, A., Qi, X.-L., and Zhang, S.-C. (2018). Topological quantum computation based on chiral Majorana fermions. *Proceedings of the National Academy of Sciences*, 115(43):10938–10942.

[Lieb, 1989] Lieb, E. H. (1989). Two theorems on the Hubbard model. *Physical Review Letters*, 62(10):1201.

[Liu et al., 2009] Liu, R., Ji, C., Mock, J., Chin, J., Cui, T., and Smith, D. (2009). Broadband ground-plane cloak. *Science*, 323(5912):366–369.

[Liu et al., 2019] Liu, S., Gao, W., Zhang, Q., Ma, S., Zhang, L., Liu, C., Xiang, Y. J., Cui, T. J., and Zhang, S. (2019). Topologically protected edge state in two-dimensional Su–Schrieffer–Heeger circuit. *Research*, 2019.

[Liu and Semperlotti, 2018] Liu, T.-W. and Semperlotti, F. (2018). Tunable acoustic valley–Hall edge states in reconfigurable phononic elastic waveguides. *Physical Review Applied*, 9(1):014001.

[Liu et al., 2012] Liu, Z., Bergholtz, E. J., Fan, H., and Läuchli, A. M. (2012). Fractional Chern insulators in topological flat bands with higher Chern number. *Physical Review Letters*, 109(18):186805.

[Lu et al., 2016] Lu, J., Qiu, C., Ke, M., and Liu, Z. (2016). Valley vortex states in sonic crystals. *Physical Review Letters*, 116(9):093901.

[Lu et al., 2017] Lu, J., Qiu, C., Ye, L., Fan, X., Ke, M., Zhang, F., and Liu, Z. (2017). Observation of topological valley transport of sound in sonic crystals. *Nature Physics*, 13(4):369–374.

[Lu et al., 2014] Lu, L., Joannopoulos, J. D., and Soljačić, M. (2014). Topological photonics. *Nature Photonics*, 8(11):821–829.

[Lu et al., 2009] Lu, M.-H., Feng, L., and Chen, Y.-F. (2009). Phononic crystals and acoustic metamaterials. *Materials Today*, 12(12):34–42.

[Ma et al., 2019a] Ma, G., Xiao, M., and Chan, C. T. (2019a). Topological phases in acoustic and mechanical systems. *Nature Reviews Physics*, 1(4):281–294.

[Ma et al., 2019b] Ma, Q., Xu, S.-Y., Shen, H., MacNeill, D., Fatemi, V., Chang, T.-R., Valdivia, A. M. M., Wu, S., Du, Z., Hsu, C.-H., Fang, S., Gibson, Q. D., Watanabe, K., Taniguchi, T., Cava, R. J., Kaxiras, E., Lu, H.-Z., Lin, H., Fu, L., Gedik, N., and Jarillo-Herrero, P. (2019b). Observation of the nonlinear Hall effect under time-reversal-symmetric conditions. *Nature*, 565(7739):337–342.

[Ma and Shvets, 2016] Ma, T. and Shvets, G. (2016). All-Si valley-Hall photonic topological insulator. *New Journal of Physics*, 18(2):025012.

[Mak et al., 2014] Mak, K. F., McGill, K. L., Park, J., and McEuen, P. L. (2014). The valley Hall effect in MoS_2 transistors. *Science*, 344(6191):1489–1492.

[Makwana and Craster, 2018] Makwana, M. P. and Craster, R. V. (2018). Designing multidirectional energy splitters and topological valley supernetworks. *Physical Review B*, 98(23):235125.

[Mao et al., 2015] Mao, X., Souslov, A., Mendoza, C. I., and Lubensky, T. C. (2015). Mechanical instability at finite temperature. *Nature Communications*, 6(1):1–8.

[Martin et al., 2008] Martin, I., Blanter, Y. M., and Morpurgo, A. (2008). Topological confinement in bilayer graphene. *Physical Review Letters*, 100(3):036804.

[Meier et al., 2016] Meier, E. J., An, F. A., and Gadway, B. (2016). Observation of the topological soliton state in the Su-Schrieffer-Heeger model. *Nature Communications*, 7(1):1–6.

[Mesaros et al., 2010] Mesaros, A., Papanikolaou, S., Flipse, C., Sadri, D., and Zaanen, J. (2010). Electronic states of graphene grain boundaries. *Physical Review B*, 82(20):205119.

[Mousavi et al., 2015] Mousavi, S. H., Khanikaev, A. B., and Wang, Z. (2015). Topologically protected elastic waves in phononic metamaterials. *Nature Communications*, 6(1):1–7.

[Mukherjee et al., 2015] Mukherjee, S., Spracklen, A., Choudhury, D., Goldman, N., Öhberg, P., Andersson, E., and Thomson, R. R. (2015). Observation of a localized flat-band state in a photonic Lieb lattice. *Physical Review Letters*, 114(24):245504.

[Nadj-Perge et al., 2014] Nadj-Perge, S., Drozdov, I. K., Li, J., Chen, H., Jeon, S., Seo, J., MacDonald, A. H., Bernevig, B. A., and Yazdani, A. (2014). Observation of Majorana fermions in ferromagnetic atomic chains on a superconductor. *Science*, 346(6209):602–607.

[Nash et al., 2015] Nash, L. M., Kleckner, D., Read, A., Vitelli, V., Turner, A. M., and Irvine, W. T. (2015). Topological mechanics of gyroscopic metamaterials. *Proceedings of the National Academy of Sciences*, 112(47):14495–14500.

[Nayak et al., 2008] Nayak, C., Simon, S. H., Stern, A., Freedman, M., and Sarma, S. D. (2008). Non-Abelian anyons and topological quantum computation. *Reviews of Modern Physics*, 80(3):1083.

[Neupert et al., 2011] Neupert, T., Santos, L., Chamon, C., and Mudry, C. (2011). Fractional quantum Hall states at zero magnetic field. *Physical Review Letters*, 106(23):236804.

[Ni et al., 2019] Ni, X., Chen, K., Weiner, M., Apigo, D. J., Prodan, C., Alù, A., Prodan, E., and Khanikaev, A. B. (2019). Observation of Hofstadter butterfly and topological edge states in reconfigurable quasi-periodic acoustic crystals. *Communications Physics*, 2(1):1–7.

[Ni et al., 2018] Ni, X., Purtseladze, D., Smirnova, D. A., Slobozhanyuk, A., Alù, A., and Khanikaev, A. B. (2018). Spin-and valley-polarized one-way Klein tunneling in photonic topological insulators. *Science Advances*, 4(5):eaap8802.

[Nicolaou and Motter, 2012] Nicolaou, Z. G. and Motter, A. E. (2012). Mechanical metamaterials with negative compressibility transitions. *Nature Materials*, 11(7):608–613.

[Noh et al., 2018] Noh, J., Huang, S., Chen, K. P., and Rechtsman, M. C. (2018). Observation of photonic topological valley Hall edge states. *Physical Review Letters*, 120(6):063902.

[Oh, 2013] Oh, S. (2013). The complete quantum Hall trio. *Science*, 340(6129):153–154.

[Ota et al., 2018] Ota, Y., Katsumi, R., Watanabe, K., Iwamoto, S., and Arakawa, Y. (2018). Topological photonic crystal nanocavity laser. *Communications Physics*, 1(1):1–8.

[Ozawa et al., 2019] Ozawa, T., Price, H. M., Amo, A., Goldman, N., Hafezi, M., Lu, L., Rechtsman, M. C., Schuster, D., Simon, J., Zilberberg, O., and Carusotto, I. (2019). Topological photonics. *Reviews of Modern Physics*, 91:015006.

[Padavić et al., 2018] Padavić, K., Hegde, S. S., DeGottardi, W., and Vishveshwara, S. (2018). Topological phases, edge modes, and the Hofstadter butterfly in coupled Su-Schrieffer-Heeger systems. *Physical Review B*, 98(2):024205.

[Pal et al., 2019] Pal, R. K., Rosa, M. I., and Ruzzene, M. (2019). Topological bands and localized vibration modes in quasiperiodic beams. *New Journal of Physics*, 21(9):093017.

[Pal and Ruzzene, 2017] Pal, R. K. and Ruzzene, M. (2017). Edge waves in plates with resonators: An elastic analogue of the quantum valley Hall effect. *New Journal of Physics*, 19(2):025001.

[Pal et al., 2016] Pal, R. K., Schaeffer, M., and Ruzzene, M. (2016). Helical edge states and topological phase transitions in phononic systems using bi-layered lattices. *Journal of Applied Physics*, 119(8):084305.

[Paulose et al., 2015a] Paulose, J., Chen, B. G.-g., and Vitelli, V. (2015a). Topological modes bound to dislocations in mechanical metamaterials. *Nature Physics*, 11(2):153–156.

[Paulose et al., 2015b] Paulose, J., Meeussen, A. S., and Vitelli, V. (2015b). Selective buckling via states of self-stress in topological metamaterials. *Proceedings of the National Academy of Sciences*, 112(25):7639–7644.

[Peano et al., 2015] Peano, V., Brendel, C., Schmidt, M., and Marquardt, F. (2015). Topological phases of sound and light. *Physical Review X*, 5(3):031011.

[Pendry, 2000] Pendry, J. B. (2000). Negative refraction makes a perfect lens. *Physical Review Letters*, 85(18):3966.

[Po et al., 2018] Po, H. C., Zou, L., Vishwanath, A., and Senthil, T. (2018). Origin of Mott insulating behavior and superconductivity in twisted bilayer graphene. *Physical Review X*, 8(3):031089.

[Proctor et al., 2021] Proctor, M., Blanco de Paz, M., Bercioux, D., García-Etxarri, A., and Arroyo Huidobro, P. (2021). Higher-order topology in plasmonic kagome lattices. *Applied Physics Letters*, 118(9):091105.

[Proctor et al., 2020] Proctor, M., Huidobro, P. A., Maier, S. A., Craster, R. V., and Makwana, M. P. (2020). Manipulating topological valley modes in plasmonic metasurfaces. *Nanophotonics*, 9(3):657–665.

[Prodan et al., 2017] Prodan, E., Dobiszewski, K., Kanwal, A., Palmieri, J., and Prodan, C. (2017). Dynamical Majorana edge modes in a broad class of topological mechanical systems. *Nature Communications*, 8(1):1–7.

[Prodan and Prodan, 2009] Prodan, E. and Prodan, C. (2009). Topological phonon modes and their role in dynamic instability of microtubules. *Physical Review Letters*, 103(24):248101.

[Prodan and Schulz-Baldes, 2016] Prodan, E. and Schulz-Baldes, H. (2016). Bulk and boundary invariants for complex topological insulators. *K*.

[Prodan and Shmalo, 2019] Prodan, E. and Shmalo, Y. (2019). The K-theoretic bulk-boundary principle for dynamically patterned resonators. *Journal of Geometry and Physics*, 135:135–171.

[Qian et al., 2018] Qian, K., Apigo, D. J., Prodan, C., Barlas, Y., and Prodan, E. (2018). Topology of the valley-Chern effect. *Physical Review B*, 98(15):155138.

[Qian et al., 2020] Qian, K., Zhu, L., Ahn, K. H., and Prodan, C. (2020). Observation of flat frequency bands at open edges and antiphase boundary seams in topological mechanical metamaterials. *Physical Review Letters*, 125(22):225501.

[Qiao et al., 2011] Qiao, Z., Jung, J., Niu, Q., and MacDonald, A. H. (2011). Electronic highways in bilayer graphene. *Nano Letters*, 11(8):3453–3459.

[Raghu and Haldane, 2008] Raghu, S. and Haldane, F. D. M. (2008). Analogs of quantum-Hall-effect edge states in photonic crystals. *Physical Review A*, 78(3):033834.

[Ren et al., 2016] Ren, Y., Qiao, Z., and Niu, Q. (2016). Topological phases in two-dimensional materials: A review. *Reports on Progress in Physics*, 79(6):066501.

[Rocklin et al., 2016] Rocklin, D. Z., Chen, B. G.-g., Falk, M., Vitelli, V., and Lubensky, T. (2016). Mechanical Weyl modes in topological Maxwell lattices. *Physical Review Letters*, 116(13):135503.

[Rocklin et al., 2017] Rocklin, D. Z., Zhou, S., Sun, K., and Mao, X. (2017). Transformable topological mechanical metamaterials. *Nature Communications*, 8(1):1–9.

[Rycerz et al., 2007] Rycerz, A., Tworzydło, J., and Beenakker, C. (2007). Valley filter and valley valve in graphene. *Nature Physics*, 3(3):172–175.

[Saba et al., 2020] Saba, M., Wong, S., Elman, M., Oh, S. S., and Hess, O. (2020). Nature of topological protection in photonic spin and valley Hall insulators. *Physical Review B*, 101(5):054307.

[Salerno et al., 2016] Salerno, G., Ozawa, T., Price, H. M., and Carusotto, I. (2016). Floquet topological system based on frequency-modulated classical coupled harmonic oscillators. *Physical Review B*, 93(8):085105.

[San-Jose and Prada, 2013] San-Jose, P. and Prada, E. (2013). Helical networks in twisted bilayer graphene under interlayer bias. *Physical Review B*, 88(12):121408.

[Sato and Fujimoto, 2016] Sato, M. and Fujimoto, S. (2016). Majorana fermions and topology in superconductors. *Journal of the Physical Society of Japan*, 85(7):072001.

[Schomerus, 2013] Schomerus, H. (2013). Topologically protected midgap states in complex photonic lattices. *Optics Letters*, 38(11):1912–1914.

[Schurig et al., 2006] Schurig, D., Mock, J. J., Justice, B., Cummer, S. A., Pendry, J. B., Starr, A. F., and Smith, D. R. (2006). Metamaterial electromagnetic cloak at microwave frequencies. *Science*, 314(5801):977–980.

[Serra-Garcia et al., 2019] Serra-Garcia, M., Süsstrunk, R., and Huber, S. D. (2019). Observation of quadrupole transitions and edge mode topology in an LC circuit network. *Physical Review B*, 99(2):020304.

[Shimazaki et al., 2015] Shimazaki, Y., Yamamoto, M., Borzenets, I. V., Watanabe, K., Taniguchi, T., and Tarucha, S. (2015). Generation and detection of pure valley current by electrically induced Berry curvature in bilayer graphene. *Nature Physics*, 11(12):1032–1036.

[Smith et al., 2004] Smith, D. R., Pendry, J. B., and Wiltshire, M. C. (2004). Metamaterials and negative refractive index. *Science*, 305(5685):788–792.

[Su et al., 1979] Su, W., Schrieffer, J., and Heeger, A. J. (1979). Solitons in polyacetylene. *Physical Review Letters*, 42(25):1698.

[Sui et al., 2015] Sui, M., Chen, G., Ma, L., Shan, W.-Y., Tian, D., Watanabe, K., Taniguchi, T., Jin, X., Yao, W., Xiao, D., et al. (2015). Gate-tunable topological valley transport in bilayer graphene. *Nature Physics*, 11(12):1027–1031.

[Sun et al., 2011] Sun, K., Gu, Z., Katsura, H., and Sarma, S. D. (2011). Nearly flatbands with nontrivial topology. *Physical Review Letters*, 106(23):236803.

[Süsstrunk and Huber, 2015] Süsstrunk, R. and Huber, S. D. (2015). Observation of phononic helical edge states in a mechanical topological insulator. *Science*, 349(6243):47–50.

[Süsstrunk and Huber, 2016] Süsstrunk, R. and Huber, S. D. (2016). Classification of topological phonons in linear mechanical metamaterials. *Proceedings of the National Academy of Sciences*, 113(33):E4767–E4775.

[Tang et al., 2011] Tang, E., Mei, J.-W., and Wen, X.-G. (2011). High-temperature fractional quantum Hall states. *Physical Review Letters*, 106(23):236802.

[Teo and Hughes, 2013] Teo, J. C. and Hughes, T. L. (2013). Existence of Majorana-fermion bound states on disclinations and the classification of topological crystalline superconductors in two dimensions. *Physical Review Letters*, 111(4):047006.

[Thouless et al., 1982] Thouless, D. J., Kohmoto, M., Nightingale, M. P., and den Nijs, M. (1982). Quantized Hall conductance in a two-dimensional periodic potential. *Physical Review Letters*, 49(6):405.

[Tutschku et al., 2020] Tutschku, C., Reinthaler, R., Lei, C., MacDonald, A., and Hankiewicz, E. (2020). Majorana-based quantum computing in nanowire devices. *Physical Review B*, 102(12):125407.

[Vaezi et al., 2013] Vaezi, A., Liang, Y., Ngai, D. H., Yang, L., and Kim, E.-A. (2013). Topological edge states at a tilt boundary in gated multilayer graphene. *Physical Review X*, 3(2):021018.

[Veselago, 1967] Veselago, V. G. (1967). Electrodynamics of substances with simultaneously negative ϵ and μ. *Usp. Fiz. Nauk*, 92:517.

[Vicencio et al., 2015] Vicencio, R. A., Cantillano, C., Morales-Inostroza, L., Real, B., Mejía-Cortés, C., Weimann, S., Szameit, A., and Molina, M. I. (2015). Observation of localized states in Lieb photonic lattices. *Physical Review Letters*, 114(24):245503.

[Vila et al., 2017] Vila, J., Pal, R. K., and Ruzzene, M. (2017). Observation of topological valley modes in an elastic hexagonal lattice. *Physical Review B*, 96(13):134307.

[Vila et al., 2019] Vila, J., Paulino, G. H., and Ruzzene, M. (2019). Role of nonlinearities in topological protection: Testing magnetically coupled fidget spinners. *Physical Review B*, 99(12):125116.

[Voss and Ballon, 2020] Voss, H. U. and Ballon, D. J. (2020). Topological modes in radiofrequency resonator arrays. *Physics Letters A*, 384(8):126177.

[Wang and Ran, 2011] Wang, F. and Ran, Y. (2011). Nearly flat band with Chern number $C = 2$ on the dice lattice. *Physical Review B*, 84(24):241103.

[Wang et al., 2012] Wang, Y.-F., Yao, H., Gong, C.-D., and Sheng, D. (2012). Fractional quantum Hall effect in topological flat bands with Chern number two. *Physical Review B*, 86(20):201101.

[Wang et al., 2015] Wang, Y.-T., Luan, P.-G., and Zhang, S. (2015). Coriolis force induced topological order for classical mechanical vibrations. *New Journal of Physics*, 17(7):073031.

[Wang et al., 2016] Wang, Z., Cheng, F., Winsor, T., and Liu, Y. (2016). Optical chiral metamaterials: A review of the fundamentals, fabrication methods and applications. *Nanotechnology*, 27(41):412001.

[Wang et al., 2009] Wang, Z., Chong, Y., Joannopoulos, J. D., and Soljačić, M. (2009). Observation of unidirectional backscattering-immune topological electromagnetic states. *Nature*, 461(7265):772–775.

[Wang et al., 2020] Wang, Z., Rodriguez, J. O., Jiao, L., Howard, S., Graham, M., Gu, G., Hughes, T. L., Morr, D. K., and Madhavan, V. (2020). Evidence for dispersing 1D Majorana channels in an iron-based superconductor. *Science*, 367(6473):104–108.

[Wiersma, 2015] Wiersma, D. (2015). Trapped in a photonic maze. *Physics*, 8:55.

[Wong et al., 2020] Wong, S., Saba, M., Hess, O., and Oh, S. S. (2020). Gapless unidirectional photonic transport using all-dielectric kagome lattices. *Physical Review Research*, 2(1):012011.

[Wright and Hyart, 2011] Wright, A. R. and Hyart, T. (2011). Robust one-dimensional wires in lattice mismatched bilayer graphene. *Applied Physics Letters*, 98(25):251902.

[Wu et al., 2018] Wu, Y., Chaunsali, R., Yasuda, H., Yu, K., and Yang, J. (2018). Dial-in topological metamaterials based on bistable Stewart Platform. *Scientific Reports*, 8(1):1–9.

[Xiao et al., 2007] Xiao, D., Yao, W., and Niu, Q. (2007). Valley-contrasting physics in graphene: Magnetic moment and topological transport. *Physical Review Letters*, 99(23):236809.

[Xiao et al., 2015a] Xiao, M., Chen, W.-J., He, W.-Y., and Chan, C. T. (2015a). Synthetic gauge flux and Weyl points in acoustic systems. *Nature Physics*, 11(11):920–924.

[Xiao et al., 2015b] Xiao, M., Ma, G., Yang, Z., Sheng, P., Zhang, Z., and Chan, C. T. (2015b). Geometric phase and band inversion in periodic acoustic systems. *Nature Physics*, 11(3):240–244.

[Xie et al., 2019] Xie, B.-Y., Su, G.-X., Wang, H.-F., Su, H., Shen, X.-P., Zhan, P., Lu, M.-H., Wang, Z.-L., and Chen, Y.-F. (2019). Visualization of higher-order topological insulating phases in two-dimensional dielectric photonic crystals. *Physical Review Letters*, 122(23):233903.

[Xie et al., 2018] Xie, B.-Y., Wang, H.-F., Wang, H.-X., Zhu, X.-Y., Jiang, J.-H., Lu, M.-H., and Chen, Y.-F. (2018). Second-order photonic topological insulator with corner states. *Physical Review B*, 98(20):205147.

[Xin et al., 2020] Xin, L., Siyuan, Y., Harry, L., Minghui, L., and Yanfeng, C. (2020). Topological mechanical metamaterials: A brief review. *Current Opinion in Solid State and Materials Science*, 24(5):100853.

[Xiong et al., 2018] Xiong, Z., Wang, H.-X., Ge, H., Shi, J., Luo, J., Lai, Y., Lu, M.-H., and Jiang, J.-H. (2018). Topological node lines in mechanical metacrystals. *Physical Review B*, 97(18):180101.

[Yan et al., 2019] Yan, Q., Zhou, Y.-F., and Sun, Q.-F. (2019). Electrically tunable chiral Majorana edge modes in quantum anomalous Hall insulator–topological superconductor systems. *Physical Review B*, 100(23):235407.

[Yankowitz et al., 2019] Yankowitz, M., Chen, S., Polshyn, H., Zhang, Y., Watanabe, K., Taniguchi, T., Graf, D., Young, A. F., and Dean, C. R. (2019). Tuning superconductivity in twisted bilayer graphene. *Science*, 363(6431):1059–1064.

[Yao et al., 2008] Yao, W., Xiao, D., and Niu, Q. (2008). Valley-dependent optoelectronics from inversion symmetry breaking. *Physical Review B*, 77(23):235406.

[Zeng et al., 2020] Zeng, Y., Chattopadhyay, U., Zhu, B., Qiang, B., Li, J., Jin, Y., Li, L., Davies, A. G., Linfield, E. H., Zhang, B., et al. (2020). Electrically pumped topological laser with valley edge modes. *Nature*, 578(7794):246–250.

[Zhang et al., 2011a] Zhang, F., Jung, J., Fiete, G. A., Niu, Q., and MacDonald, A. H. (2011a). Spontaneous quantum Hall states in chirally stacked few-layer graphene systems. *Physical Review Letters*, 106(15):156801.

[Zhang et al., 2013] Zhang, F., MacDonald, A. H., and Mele, E. J. (2013). Valley Chern numbers and boundary modes in gapped bilayer graphene. *Proceedings of the National Academy of Sciences*, 110(26):10546–10551.

[Zhang et al., 2011b] Zhang, L., Ren, J., Wang, J.-S., and Li, B. (2011b). The phonon Hall effect: Theory and application. *Journal of Physics: Condensed Matter*, 23(30):305402.

[Zhang et al., 2018] Zhang, X., Xiao, M., Cheng, Y., Lu, M.-H., and Christensen, J. (2018). Topological sound. *Communications Physics*, 1(1):1–13.

[Zhou et al., 2019] Zhou, D., Zhang, L., and Mao, X. (2019). Topological boundary floppy modes in quasicrystals. *Physical Review X*, 9(2):021054.

[Zhu et al., 2018a] Zhu, H., Liu, T.-W., and Semperlotti, F. (2018a). Design and experimental observation of valley-Hall edge states in diatomic-graphene-like elastic waveguides. *Physical Review B*, 97(17):174301.

[Zhu et al., 2019] Zhu, L., Prodan, E., and Ahn, K. H. (2019). Flat energy bands within antiphase and twin boundaries and at open edges in topological materials. *Physical Review B*, 99(4):041117.

[Zhu et al., 2018b] Zhu, W., Ding, Y.-q., Ren, J., Sun, Y., Li, Y., Jiang, H., and Chen, H. (2018b). Zak phase and band inversion in dimerized one-dimensional locally resonant metamaterials. *Physical Review B*, 97(19):195307.